

Functional Convergence at the Mouse Retinogeniculate Synapse

A dissertation presented

by

Elizabeth Yakovlevna Litvina

to

The Division of Medical Sciences

in partial fulfillment of the requirements

for the degree of

Doctor of Philosophy

in the subject of

Neurobiology

Harvard University

Cambridge, Massachusetts

June 2017

© 2017 Elizabeth Yakovlevna Litvina

All rights reserved.

Functional Convergence at the Mouse Retinogeniculate SynapseABSTRACT

The basic wiring diagram of a mammalian sensory circuit can illuminate the synaptic underpinnings of its function. The mammalian retina possesses a diversity retinal ganglion cell (RGC) types that encode different features of the visual scene. We do not yet fully understand how the visual system uses these features to support vision. According to the leading view, these diverse RGCs form separate channels of information that remain segregated as parallel lines that are relayed through the dorsoLateral Geniculate Nucleus (dLGN) to the visual cortex, where they finally converge in different combinations to form the basis of complex visual feature extraction.

In this dissertation, I interrogate the degree to which the functional organization of the mouse retinogeniculate synapse—the site of synaptic contact between a RGC axon and a thalamocortical (TC) neuron—conforms to this view. In the first study, I demonstrate that developmental refinement continues past p30, following the closure of the thalamic and cortical critical periods. This refinement coincides with the pruning of the broad RGC axonal arbor. Earlier in development, an arbor retains the potential to contact new geniculate partners through the reorganization of synaptic boutons along its scaffold, which exhibits plasticity in response to visual manipulation. Retinogeniculate connectivity thus remains morphologically and functionally plastic into adulthood in mice. In the second study, I optogenetically label RGCs in order to quantify the number of RGCs that innervate TC neurons in mice. In contrast to prior functional estimates, I show that an average of 10 RGCs converge onto a geniculate neuron, though only 30% of these contacts may strongly drive postsynaptic spiking. My final study asks whether

retinogeniculate connectivity maintains functional segregation of visual information despite this surprisingly high degree of convergence; I use optogenetics to test if multiple types of RGCs can provide substantial inputs to the same TC neuron. Evidence from three groups of direction-selective RGCs shows that mature TC neurons often receive functional synaptic input from more than one RGC type. Together, these studies show the retinogeniculate functional organization in mice may support the computation of complex visual features at the level of the dLGN.

Table of Contents

Acknowledgements	vi
Chapter 1: Introduction. An Evolving View of Retinogeniculate Transmission	1
Chapter 2: Materials and Methods	33
Chapter 3: Refinement of the Retinogeniculate Synapse by Bouton Clustering.....	53
Abstract	55
Introduction	56
Results	57
Discussion	65
Chapter 4: Functional Convergence at the Retinogeniculate Synapse	72
Abstract	74
Introduction	75
Results	76
Discussion	108
Chapter 5: Examining the Functional Integration of Multiple Types of RGCs in Mouse dLGN Thalamocortical Neurons.....	114
Abstract	115
Introduction	115
Results	117
Discussion	142
Chapter 6: Conclusions	147
Appendix: Supplemental Figures	153
References	164

Acknowledgements

I would like to thank my many mentors for guidance, resources, motivation, and patience. First and foremost, I want to express my gratitude and appreciation to Chinfei Chen, my PhD advisor, whose intelligence, generosity, resourcefulness, creativity, dedication, and ceaseless drive make her a great model scientist and mentor. Working with her has been a great privilege. I would also like to thank: my Dissertation Advisory Committee, the members of the Kirby Neuroscience Department, including the Imaging and Viral Cores staff, Karen Harmin, and past and present Program in Neuroscience directions for their compassion and devotion to student success and the neuroscience community at Harvard. I also gratefully acknowledge generous financial support from the Lefler Center.

My senior lab mates, Andrew Thompson, Jess Hauser, Kate Hong, David Lin, Liang Liang, and Celeste-Elise Stephanie have over the years inspired and motivated me, and have been generous with their scientific excellence, time, patience, honesty, and optimism. I also thank several excellent technicians for their friendship and invaluable technical assistance: Kevin Park, Joseph Leffler, Matthew Taylor, Mallory Stanley, Genelle Rankin, and Sally Curtiss.

Finally I must express my gratitude to Foster Nichols V, and my three families: my Wesleyan family for their honest companionship, my musical family Boston Choral Ensemble for providing a cheap alternative to therapy, and of course, my biological family for the many sacrifices they have made to support me. They've all been with me for this journey and I'll be glad to see a lot more of them now that it's done. I dedicate my work to the next generation of awesome women in these families: Зюка, Фефа, Ася, and Eloise.

CHAPTER 1:

Introduction: An Evolving View of Retinogeniculate Transmission

Attributions: This chapter is a review accepted for publication in a special issue of Visual Neuroscience. It is reprinted here with permission from Cambridge University Press. EYL drafted the manuscript with the intention of including it as the introduction to this dissertation; EYL and CC edited and revised the manuscript for publication. The work benefited from critical advice and close reading by C-E Stephanie, G Rankin, AD Thompson, and two anonymous reviewers.

An Evolving View of Retinogeniculate Transmission

Elizabeth Y Litvina and Chinfai Chen*

Department of Neurology, F.M. Kirby Neurobiology Center, Children's Hospital, Boston, 300

Longwood Avenue, Boston, MA 02115

Program in Neuroscience

Harvard Medical School

220 Longwood Avenue, Boston, MA 02115

*To whom correspondence should be addressed:

F.M. Kirby Neurobiology Center Boston Children's Hospital

300 Longwood Avenue, CLS 12250 Boston, MA 02115

Phone: 617-919-2685, Fax: 617-919-2772

chinfai.chen@childrens.harvard.edu

ABSTRACT

The thalamocortical relay neuron of the dorsoLateral Geniculate Nucleus (dLGN) has borne its imprecise label for many decades in spite of strong evidence that its role in visual processing transcends the implied simplicity of the term “relay” (Bishop et al., 1959; Kastner et al., 2006; Sherman, 2007; Kaplan, 2014; Usrey & Alitto, 2015; Weyand, 2016). The retinogeniculate synapse is the site of communication between a retinal ganglion cell and a thalamocortical neuron of the dLGN. Activation of retinal fibers in the optic tract causes reliable, rapid, and robust post-synaptic potentials that drive postsynaptic spikes in a thalamocortical neuron. Cortical and subcortical modulatory systems have been known for decades to regulate retinogeniculate transmission (Sherman, 2016). The dynamic properties that the retinogeniculate synapse itself exhibits during and after developmental refinement further enrich the role of the dLGN in the transmission of the retinal signal. Here we consider the structural and functional substrates for retinogeniculate synaptic transmission and plasticity, and reflect on how the complexity of the retinogeniculate synapse imparts a novel dynamic and influential capacity to subcortical processing of visual information.

Keywords: retinogeniculate synapse, short-term plasticity, developmental refinement, visual circuit, synaptic transmission

More Than A Relay

The retinogeniculate synapse has been an invaluable workhorse for neuroscience research. In recent years, it has served as a powerful model for understanding the molecular and circuit-level mechanisms that influence normal development and disease (Sengpiel & Kind, 2002; Guido, 2008; Kano & Hashimoto, 2009; Hong & Chen, 2011; Stephan et al., 2012). The ability to independently label Retinal Ganglion Cells (RGCs) from opposite eyes has enabled the identification of cellular and molecular mechanisms of axon mapping, arbor pruning and synapse elimination that drive the refinement of retinotopic maps and eye-specific lamination (Wong, 1999; Luo & O’Leary, 2005; Huberman et al., 2008a; Feller, 2009; Kano & Hashimoto, 2009; Hong & Chen, 2011). *In vitro*, the easily accessible bundle of RGC axons in the optic nerve provides a convenient means of selectively activating presynaptic inputs in studies of synaptic physiology and plasticity, and is also an excellent system for uncovering mechanisms of axon regeneration (Guido, 2008; Hong & Chen, 2011; Benowitz et al., 2017). *In vivo*, the retinogeniculate synapse has been a prominent model system for the study of subcortical visual processing. Numerous studies have capitalized on the ease of manipulating visual stimulation, combined with the ability to simultaneously monitor the activity patterns of inputs and outputs of the thalamus to reliably demonstrate that the transfer of information from the retina to the visual cortex is the major function of the retinogeniculate synapse (Sherman, 2005; Usrey & Alitto, 2015; Weyand, 2016).

Despite the tenacity of the term “relay” to describe the function of the dLGN, the retinogeniculate synapse does not simply transfer a copy of RGC activity patterns to the cortex. Over the past few decades, a number of retinogeniculate attributes have been shown to play a role in modifying visual information before conveying it to the cortex (Blitz et al., 2004; Sherman, 2007; Usrey & Alitto, 2015; Weyand, 2016). Simultaneous recording of the firing patterns of RGC inputs and thalamocortical (TC) target neurons *in vivo* has shown that the reliability of action potential generation in TC neurons depends on the local activity context, such as

neuromodulatory signaling or the membrane potential. These factors can dictate or modulate the firing pattern (“tonic” or “burst”) of a TC neuron (Usrey et al., 1998; Sherman & Guillery, 2002; Wang et al., 2007). In some cases, a TC neuron is much more likely to generate a response to the second of a pair of visually-driven potentials arriving in quick succession (separated by less than 30 msec, Mastronarde, 1987; von Krosigk et al., 1993; Usrey *et al.*, 1998; Levine & Cleland, 2001; Rowe & Fischer, 2001; Carandini *et al.*, 2007; Weyand, 2007; Sincich *et al.*, 2007, 2009; Alitto *et al.*, 2011). This integrative function increases the amount of information encoded in thalamic spiking (Wang et al., 2010). In other cases, a single RGC impulse can result in a postsynaptic burst of multiple action potentials (Usrey et al., 1998; Blitz & Regehr, 2003).

Recent work is revealing new receptive field complexity and plasticity in the dLGN that further demonstrates significant thalamic processing of visual information en route to the cortex, at least in some species. Stimulus orientation selectivity is one salient example of a complex feature encoded in subpopulations of dLGN neurons in a variety of species: mouse (Marshall et al. 2012; Piscopo et al. 2013; Zhao et al. 2013; Scholl et al. 2013) and rabbit (Levick et al., 1969; Hei et al., 2014), with weaker orientation or direction bias occurring in the cat (Hubel & Wiesel, 1961; Daniels et al., 1977; Levick & Thibos, 1980; Vidyasagar & Urbas, 1982; Soodak et al., 1987; Shou & Leventhal, 1989; Thompson et al., 1994), squirrel (Zaltsman et al., 2015), and primate (Lee et al., 1979; Smith et al., 1990; Cheong et al., 2013). Complex feature selectivity persists in TC neurons after inactivation of the primary visual cortex, suggesting that the dLGN may compute orientation or direction selectivity rather than inherit it from cortical feedback (cat Vidyasagar & Urbas 1982; mouse Zhao et al. 2013; Scholl et al. 2013). Furthermore, cat TC neurons have a higher stimulus contrast sensitivity than their individual inputs, suggesting TC neurons can functionally integrate information from multiple RGC inputs (Rathbun et al., 2016). The presence of binocularly innervated dLGN neurons in mice, cats, and primates further supports the possibility of convergence of multiple RGCs onto single geniculate

neurons in mice, cat, and primate dLGN (Sanderson et al., 1971; Howarth et al., 2014; Zeater et al., 2015; Rompani et al., 2017). Here, we explore synaptic mechanisms and structural attributes that could support the diversity of features and functions now emerging in studies of the dLGN. In this review, we describe the structural properties of RGC axons and TC neurons, together with their biophysical features and plasticity mechanisms. These properties may combine to impart novel and adaptive functionality to the dLGN, and to dynamically regulate information flow between retina and cortex.

Retinogeniculate Synaptic Structure

To appreciate the functional complexity in retinogeniculate processing, we first describe the underlying synaptic structure. The architecture of the retinogeniculate synapse is conserved across species. Glutamate is the excitatory neurotransmitter packed into numerous round vesicles contained in large synaptic terminals along the axon (Montero & Wenthold, 1989). A single retinal axon terminal can span ~1-4 microns in diameter and contain multiple spatially distinct neurotransmitter release sites (cat and mouse studies: Famiglietti & Peters, 1972; Rafols & Valverde, 1973; Sur & Sherman, 1982; Hamos et al., 1987; Robson, 1993; Bickford et al., 2010; Budisantoso et al., 2012; Morgan et al., 2016). RGC boutons contact a TC neuron near its cell body, synapsing directly onto the dendritic shaft or dendritic appendages that protrude from the proximal shaft or primary dendritic branch points (Rafols & Valverde, 1973; Robson & Mason, 1979; Wilson et al., 1984; Hamos et al., 1987; Bickford et al., 2010; Morgan et al., 2016). Retinal inputs account for only 5-10% of a TC neuron's synaptic input, whereas cortical feedback projections from Layer 6 occupy the distal dendrites, providing as much as 50% of synaptic input (Wilson et al., 1984; Montero, 1991; Van Horn et al., 2000). Nonetheless, the proximal position of retinogeniculate synapses along the dendrite, their synaptic structure with multiple release sites, and their large number of synaptic contacts drives powerful and reliable

transmission that has earned the retinal input the moniker of “driver” to all other inputs’ “modulator” (Guillery & Sherman, 2002).

The fine details of retinogeniculate connectivity reveal potential heterogeneity of circuit organization and, thereby, of function. A RGC axon contacts a TC neuron with as many as 59 terminals in cat or mouse (Hamos et al., 1987; Robson, 1993; Morgan et al., 2016). The morphology of these numerous synaptic contacts between a single RGC axon and its target TC neuron can range from the simple to the complex (Figure 1.1A-C; Jones & Powell 1969; Famiglietti & Peters 1972; Hammer et al. 2015; for finer categorization, see Lund & Cunningham, 1972; Robson & Mason 1979; Morgan et al. 2016). Simple retinogeniculate contacts consist of one small or large crenulated bouton contacting a dendrite or dendritic appendage. Complex contacts comprise a glomerular structure containing multiple boutons from retinal, inhibitory, and neuromodulatory inputs (Robson & Mason, 1979; Koch, 1985; Sherman & Guillery, 1996; Sherman, 2004). Although it is not known whether differences in bouton morphology correlate with specializations for retinogeniculate information transfer, work on cerebellar parallel fibers shows that bouton size can predict sensitivity to neuromodulation, and induction of LTP or LTD can induce plasticity in the size of hippocampal presynaptic boutons (Toni et al., 1999; Becker et al., 2008; Zhang & Linden, 2009). Furthermore, the morphology of synaptic contacts is optimized to the requirements of sensory transmission in the retina, inner ear, and central auditory synapses (Taschenberger et al., 2002; Matthews & Fuchs, 2010; Freche et al., 2011; Graydon et al, 2014). it is therefore likely that the diversity of retinogeniculate contact morphologies reflects differences in their contribution to transmission. Indeed, different TC neuron types in cats exhibit biases in presynaptic morphology. Cat RGCs and TC neurons are distinguished into three categories (X, Y, W) based on the properties of their responses to visual stimuli, including the size of the receptive field and the degree of linearity of spatial summation, as well as morphological markers. The X and Y classifications

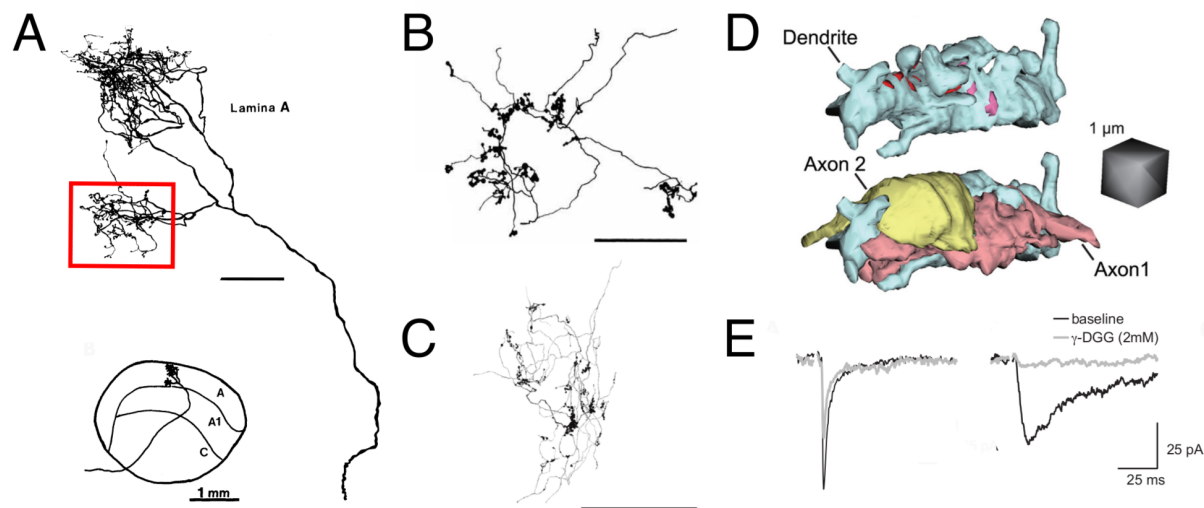


Figure 1.1: Synaptic structure shapes retinogeniculate transmission.

(A). Tracing of an HRP-filled X-RGC arbor in the cat dLGN shows the location and morphology of a single branch (red box) of the X-RGC arbor used for EM reconstruction. This branch of the axon contacts 4 TC neurons out of 40 available neurons in the territory of the arbor. The remainder of the axon was not reconstructed, and likely contacts several other TC neurons. Bottom inset shows the location of the axonal arbor in the context of the cat LGN. Figure modified from Hamos et al. 1987. Unmarked scale bar = 100 μm . (B, C). Reconstructed arbors of single RGC axons showing distribution of presynaptic boutons into dense clusters in the LGN of (B) an adult cat and (C) a p20 mouse. Note the clustering of boutons along the arbor. Image in B is modified from Robson et al, 1993, showing a segment of a RGC axon; Image in C is from Hong et al, 2014, showing a BD-RGC axon. Scales bars are 100 μm . (D). A 3D reconstruction of a TC neuron dendrite and sites of contact between two neighboring RGC boutons from Budisantoso et al, 2012. In the top image, the dendrite and its appendages are depicted in blue, whereas pink and red sites label the postsynaptic densities of the two axons. In the bottom image, the structure of the terminals of two axons has been added. Spillover can occur between these two nearby terminals. (E). Evidence of spillover-mediated responses to the stimulation of a single RGC axon before eye opening. Two different synaptic responses were observed in response to single retinal fiber stimulation. Shown are recordings from TC neurons in whole cell voltage clamp at -70 mV in a dLGN slice in the presence of the NMDAR blocker, 20 μM CPP. On the left is an example of a retinogeniculate AMPAR EPSC with characteristic rapid rise time and decay kinetics (black trace). On the right is an atypical AMPAR EPSC response notable for significantly slower rise time and decay kinetics (black trace). The two types of EPSCs differ in their sensitivity to the low-affinity AMPAR antagonist, γ -DGG. Low affinity antagonists can be used to assess the relative concentration of glutamate in the synaptic cleft (Clements et al., 1992; Diamond & Jahr, 1997). As γ -DGG competes with glutamate for binding to AMPAR, its efficacy of inhibition decreases with increasing glutamate concentration. γ -DGG has only a small effect on the amplitude of the fast EPSC, but dramatically reduces the amplitude of the slow EPSC (overlaid grey traces), consistent with lower peak glutamate concentration in the

Figure 1.1 (Continued)

synaptic cleft of the slow EPSC. Because the EPSCs are evoked by minimal stimulation, the rapid EPSC represents a direct input from a single RGC axon that forms a direct synapse onto the voltage-clamped relay neuron, whereas the slow EPSC corresponds to the activation of a GC axon that does not directly synapse onto the voltage-clamped neuron. Modified from Hauser et al, 2014. All figures reprinted with permission.

refer to relatively homogeneous populations (and are often compared to primate M and P pathways), whereas the W (compared to K in primates) encompasses a more diverse set of cells with rarely-encountered physiological responses (Wilson et al., 1976; Fukuda et al., 1984; Felch & Van Hooser, 2012). Simple contacts dominate retinal input onto cat Y cells, whereas X cell dendritic appendages preferentially participate in complex synaptic structures (Robson & Mason, 1979; Koch, 1985; Sherman & Guillery, 1996; Sherman, 2004). Similar distinctions among TC neurons have been observed in the mice by morphological analysis, but have not been associated with distinct patterns of synaptic structures nor delineated by physiology (Krahe et al. 2011; El-Danaf et al. 2015; Sriram et al. 2016).

In addition to potential functional differences reflected in the morphology of presynaptic geniculate boutons, the close proximity of clustered multisynaptic boutons in the mature synapse makes possible novel interactions between glutamate transients originating in separate RGC inputs. Large simple boutons in the rat contain an average of 27 independent release sites, whereas each of the boutons in a glomerulus has approximately 6 (Hamos et al., 1987; Budisantoso et al., 2012; Hammer et al., 2015). Notably, multiple RGCs may contribute to the same cluster or glomerulus of boutons (Hammer et al., 2015; Morgan et al., 2016). At other CNS synapses, glia ensheath individual boutons and interdigitate into the synaptic cleft, preventing glutamate from diffusing, or “spilling over,” to neighboring boutons, in part through the action of glutamate transporters, which clear glutamate from the extracellular space (Diamond & Jahr, 1997; Danbolt, 2001; Tzingounis & Wadiche, 2007; Hauser et al., 2013; Rimmele & Rosenberg, 2016). In contrast, glia do not interdigitate into the cleft of single RGC boutons nor within geniculate glomeruli, making the retinogeniculate connection conducive to glutamate spillover within and between individual boutons (Famiglietti & Peters 1972; Robson & Mason 1979; Winfield et al. 1980; Mason 1982; Bickford et al. 2010). Although interbouton spillover has not been experimentally assessed in the mature dLGN, a simulation that demonstrated the likelihood of spillover between distant synapses within the same bouton also implies the

possibility of spillover of glutamate between closely spaced boutons. Figure 1.1D shows an example of two such close retinogeniculate boutons along one TC neuron dendrite, highlighting that glutamate released from one bouton can diffuse to postsynaptic release sites of the neighboring bouton (Budisantoso et al., 2012). At a developmental phase when boutons are less clustered (Sur et al., 1984; Hong et al., 2014) and glomeruli have not yet formed, retinogeniculate transmission exhibits extensive glutamate spillover between neighboring boutons. In fact, glutamate from the bouton of one RGC axon can spill over to the synaptic cleft of a neighboring RGC axon before eye opening (Hauser et al., 2014). Glutamate spillover can be distinguished from direct retinogeniculate synaptic activation by the slower kinetics of the α -amino-3-hydroxy-5-methyl-4-isoxazolepropionic acid receptor (AMPA)-mediated Excitatory Postsynaptic Current (EPSC) and increased sensitivity to g-DGG (grey traces), a low affinity AMPAR antagonist. (Figure 1.1E). These characteristics indicate that the receptors mediating the spillover current are exposed to a lower glutamate concentration than those mediating the direct EPSC. Glutamate spillover can therefore diminish synaptic specificity, but also result in complex and graded integration of information transmitted from different RGC inputs. This mechanism of transmission may be particularly relevant for high-frequency presynaptic activity (RGCs can reach up to 500 Hz, Nirenberg & Meister 1997), which would promote the pooling and spillover of glutamate. Therefore, the intricate morphology of retinogeniculate contacts presents the possibility for a diversity of modes of retinogeniculate information transfer, which could vary as a function of preceding sensory or modulatory activity.

Short-Term Plasticity

The mature retinogeniculate synapse boasts multiple bouton contacts, each with many release sites, leading to a high probability of release (Yeow & Peterson, 1991; Chen & Regehr, 2000; Budisantoso et al., 2012). Combined with the proximity of retinal contacts to the cell body that minimizes potential dendritic filtering of the synaptic signal, these structural features give

rise to an EPSC characterized by rapid kinetics (time constant of decay ~2 ms) and large amplitudes *in vitro* (Chen & Regehr, 2000; example recording in Figure 1.2A, p26-32). Studies in slices have identified several pre- and post-synaptic mechanisms of short-term plasticity that modulate these EPSCs to further shape transmission based on the activity of the RGC input itself as well as other retinal and nonretinal inputs to that neuron. In shaping retinogeniculate transmission, these short-term plasticity mechanisms provide the means to dynamically modify the information transmitted from RGC to TC neuron output.

A prominent feature of retinogeniculate transmission studied *in vitro* is short-term depression: the second of two impulses separated by a short interval generates a weaker response than the first. Both presynaptic mechanisms involving vesicle depletion and postsynaptic mechanisms including AMPAR desensitization and N-methyl-D-aspartate receptor (NMDAR) saturation contribute to this plasticity (Chen et al., 2002; Blitz et al., 2004; Budisantoso et al., 2012). In contrast to the short-term depression observed *in vitro* in mice, extracellular recordings of TC neuron activity *in vivo* in cats and primates consistently show paired-stimulus enhancement, such that the second of two retinal impulses separated by a brief (<30 msec) interval is more effective at driving a postsynaptic action potential (Mastronarde, 1987; Usrey et al., 1998; Levine & Cleland, 2001; Rowe & Fischer, 2001; Carandini et al., 2007; Rathbun et al., 2007; Sincich et al., 2007, 2009). In part, this contradiction is due to the dependence of short-term depression on the recent history of activity at the synapse. Activation of the retinogeniculate synapse in slice usually follows a period of quiescence, whereas baseline spontaneous activity maintains synaptic transmission in a chronically depressed state *in vivo* (Levick & Williams, 1964; Stoelzel et al., 2015). A train of spikes preceding optic tract stimulation *in vitro* attenuates the degree of synaptic depression (Seeburg et al., 2004; Augustinaite & Heggelund, 2007; Liu & Chen, 2008). Further, neurotransmitter inputs from the brainstem and

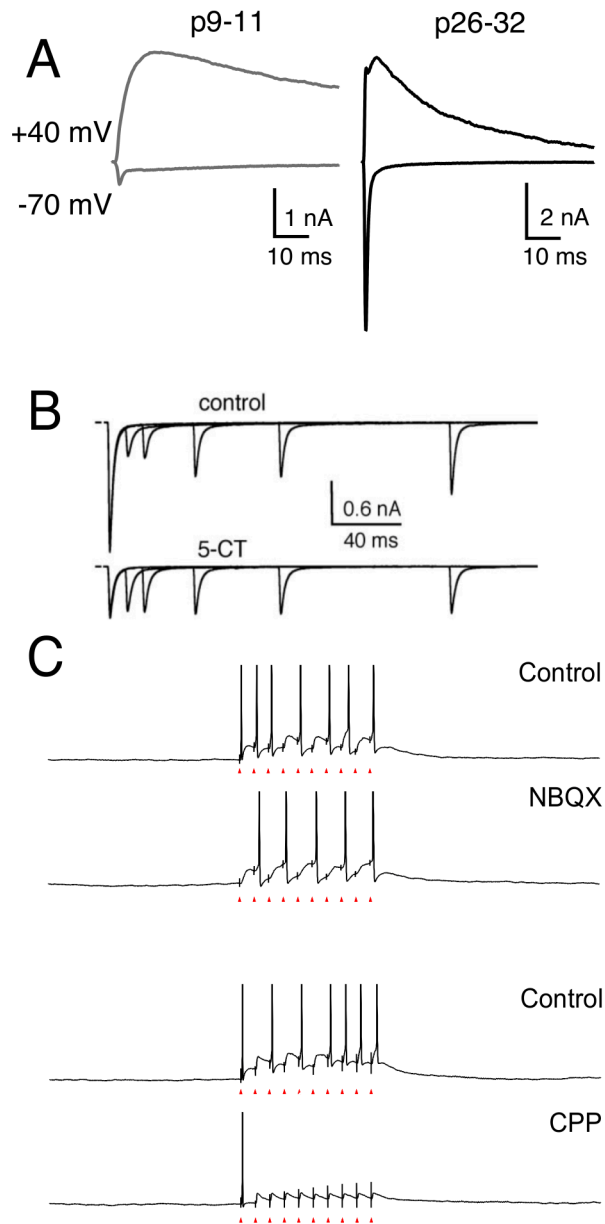


Figure 1.2: Contributions of Retinogeniculate Short-Term Plasticity.

(A). Representative traces of AMPAR and NMDAR mediated currents recorded before eye opening (left) and in a mature mouse (right) in response to the stimulation of the optic tract. Whole-cell voltage clamp recordings were performed with bicuculline to block GABA_A-receptor mediated currents. At -70 mV holding potential, AMPARs mediate the fast activating and decaying current. AMPAR and NMDAR currents both contribute to the EPSCs recorded at +40 mV with AMPARs contributing to the rapid rise of and the NMDAR currents contributing to the slow decay of the EPSC. The average amplitude of AMPAR currents increases over

Figure 1.2 (Continued)

development. (B). 5-CT-mediated activation of serotonin receptors alters retinogeniculate short-term plasticity. Experiments were performed in retinogeniculate slices from mature mice. Top and bottom traces overlay pairs of retinogeniculate EPSCs evoked with varying interstimulus intervals before (top) and after (bottom) the application of 5-CT to activate 5HT-1 receptors expressed in presynaptic retinogeniculate boutons. Application of 5-CT reduces the amplitude of the first EPSC and relieves short-term depression, increasing the amplitude of the second EPSC preferentially at short interstimulus interval. (C). Physiologically relevant stimulation frequencies preferentially diminish the contribution of AMPARs to relay neuron firing. Current clamp recordings of action potential firing in response to trains of optic tract stimulation in the presence of AMPAR (NBQX) or NMDAR (CPP) antagonists. Holding potential -50 mV. Blockade of AMPARs alters the latency to first spike but only minimally reduces the overall number of spikes. In contrast, blockade of NMDARs abolished EPSC summation towards action potential firing; only the first stimulus evokes an action potential, reflecting the contribution of AMPARs that rapidly desensitize after the first pulse. Therefore, NMDAR currents can sustain action potential generation without AMPAR contribution. Adapted from Augustinaite and Heggelund, 2007. All figures reprinted with permission.

inhibitory neurons can modulate retinogeniculate transmission in a context-dependent manner *in vivo*. To understand the relationship between *in vitro* and *in vivo* manifestations of short-term plasticity, I review the prominent sources of modulation of retinogeniculate transmission.

Presynaptic Modulation

Retinogeniculate transmission is known to be modulated presynaptically by a number of neurotransmitter receptors, including GABA_B, serotonin 5HT_{1B} (Chen & Regehr, 2003; Seeburg et al., 2004), as well as adenosine A1 (Yang et al., 2014) and metabotropic glutamate receptors (Hauser et al., 2013; Lam & Sherman, 2013). Activation of the GABA_B or 5-HT_{1B} receptors strongly depresses neurotransmitter release and relieves short-term depression by decreasing the entry of calcium into the presynaptic terminal (See Figure 1.2B; Chen & Regehr, 2003; Seeburg et al., 2004). While these modulators decrease the strength of the retinogeniculate EPSC, they also alter the pattern of action potentials transmitted from the pre- to post-synaptic neuron. For example, activation of presynaptic 5-HT_{1B} receptors leads to preferential transmission of high-frequency over low-frequency activity, essentially acting as a high-pass filter (Seeburg *et al.*, 2004). In some cases, presynaptic modulation can be additive. The combined activation of 5HT_{1B} and adenosine A1 receptors, can convert presynaptic depression into facilitation (Yang et al., 2014). Therefore, the activity of neuromodulatory inputs *in vivo* can dynamically shape retinogeniculate information transfer by modulating the degree of short-term plasticity. It is not known whether the expression of presynaptic receptors differs between RGC types or RGC bouton morphologies. However, any such differences would add an additional layer of modularity to retinogeniculate transmission.

Postsynaptic Modulation

In addition to presynaptic depression, postsynaptic glutamate receptor properties also contribute to short-term depression and shape the efficacy of retinogeniculate transmission.

Postsynaptic AMPA and NMDA receptors both exhibit short-term depression, and perform complementary functions in retinogeniculate transmission.

AMPA channel gating properties and the high density of their expression contribute to the large, rapid activation and decay kinetics of the retinogeniculate EPSC (Tarusawa et al., 2009). Because AMPARs readily conduct at negative potentials, they are effective at initiating postsynaptic spiking, even from a relatively hyperpolarized membrane potential (Blitz & Regehr, 2003; Augustinaite & Heggelund, 2007; Liu & Chen, 2008). However, AMPARs desensitize upon exposure to glutamate and recover with a time constant of ~100 msec (Kielland & Heggelund, 2002; Chen et al., 2002). These properties lead to short-term depression of the AMPAR EPSC. Therefore, AMPARs contribute to the onset of an action potential train transmitted from a RGC, initiating robust short-latency spikes during low frequency activity, but cannot sustain the robust transmission of high-frequency retinogeniculate activity (Blitz & Regehr, 2003). Figure 1.2C demonstrates that pharmacological blockade of AMPAR with NBQX reduces the initial spikes in response to a stimulus train (Turner et al., 1994; Augustinaite & Heggelund, 2007).

NMDA receptor-mediated currents have distinct kinetics and voltage dependence from AMPAR (Figure 1.3A-B). At the retinogeniculate synapse, NMDARs exhibit short-term depression due to their high affinity to glutamate and receptor saturation (Traynelis et al., 2010). Recovery from NMDAR saturation occurs more quickly than from AMPAR desensitization (Kielland & Heggelund, 2002; Chen et al., 2002). TC neuron NMDARs experience incomplete Mg^{2+} block at hyperpolarized potentials, and therefore conduct significant current at negative potentials (Liu & Chen, 2008). Figures 1.3B-C illustrates the contribution of NMDAR to transmission over development. NMDARs conduct current for many tens of milliseconds during a prolonged decay, which permits the summation of closely timed EPSCs, especially within the range of interstimulus intervals (ISIs) that exhibit paired-pulse enhancement *in vivo*, and supports multiple TC neuron spikes even in “tonic” mode (Chen et al., 2002; Blitz & Regehr,

2003; Augustinaite & Heggelund, 2007; Liu & Chen, 2008; Budisantoso et al., 2012). Blockade of NMDAR dramatically reduces retinogeniculate transmission *in vivo* (Sillito et al., 1990; Kwon et al., 1991), and NMDAR current summation *in vitro* can even drive action potential firing in the presence of AMPAR blockers, though with less temporal precision (Figure 1.2C; Chen *et al.*, 2002; Blitz & Regehr, 2003; Augustinaite & Heggelund, 2007; Budisantoso *et al.*, 2012). In fact, the NMDAR component of the first EPSC may sufficiently depolarize a TC neuron to spike threshold, such that a small or depressed AMPAR current can shorten the latency to first spike (Kielland & Heggelund, 2002; Augustinaite & Heggelund, 2007; Budisantoso et al., 2012). Therefore, summation of NMDAR currents enhances the probability of TC neuron spiking in response to the second and later RGC action potentials during a train. Together with modulation and postsynaptic integration (Carandini et al., 2007), the properties of NMDA and AMPA receptor currents can reconcile the robust short-term depression seen *in vitro* with paired-pulse enhancement observed *in vivo*.

An additional factor that could contribute to differences in *in vitro* and *in vivo* short-term plasticity is the expression of calcium-permeable AMPARs. The retinogeniculate synapse differs from other synapses in that the expression of calcium-permeable AMPARs increases over development (see Figure 4A-B; Budisantoso et al. 2012; Hauser et al. 2014; Louros et al. 2014; compare to Kumar et al. 2002; Soto et al. 2007). Calcium permeable AMPARs (those lacking the GluA2 subunit) exhibit stronger desensitization-mediated paired pulse depression (Budisantoso et al., 2012). However, depolarization-mediated reduction of polyamine block may partly rescue this effect (Rozov et al., 1998; Soto et al., 2007), increasing the contribution from AMPARs to transmission later in a train of high frequency activity.

The *in vitro* retinogeniculate preparation has permitted the identification of mechanisms regulating retinogeniculate synaptic transmission at an unmatched resolution. The synaptic mechanisms discussed above are part of a larger array of factors that affect retinogeniculate information transfer, including circuit elements that influence postsynaptic integration in the TC

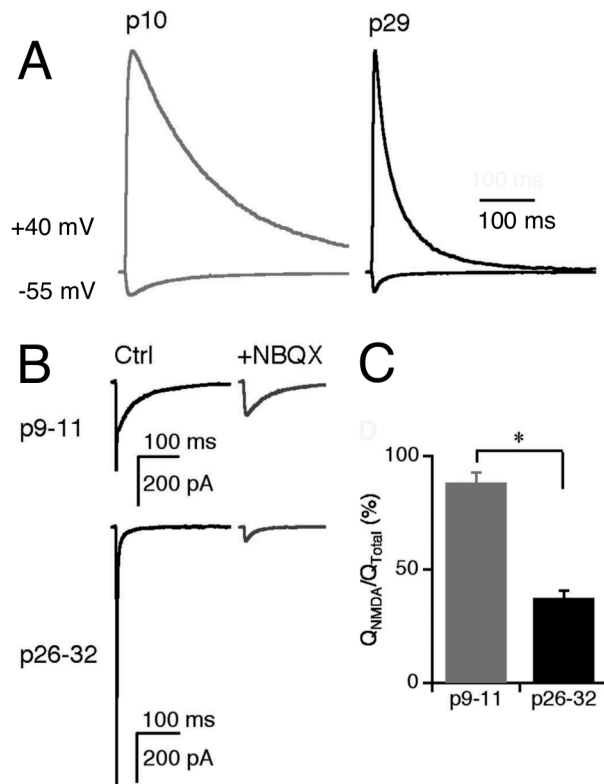


Figure 1.3: Contribution of NMDAR-currents to retinogeniculate transmission over development.

(A). NMDAR EPSCs recorded in the presence of the AMPAR blocker, NBQX, at +40 and -55 mV holding potentials in a p10 (left) and a p29 (right) retinogeniculate slice. Normalized traces are shown. Note the acceleration in NMDAR current decay time over development. (B). Example EPSCs recorded in young (top) and mature (bottom) TC neuron in slice before (left) and during (right) the application of NBQX. Holding potential, -55 mV. C. NMDAR currents contribute more to the total retinogeniculate charge transfer at P9-11 than p26-32; however, even at the mature synapse, NMDARs contribute nearly half of the total charge transfer. Figure adapted from Liu and Chen, 2008. Reprinted with Permission

neuron: local and extrageniculate GABAergic circuits, reciprocal connectivity with the cortex, and brainstem modulatory inputs (reviewed in Sherman & Guillery, 2002). Together, these synaptic and circuit mechanisms impart the dynamic features that regulate transmission of information at the retinogeniculate synapse. Interestingly, the paired-stimulus enhancement of retinogeniculate transmission *in vivo* acts not only to increase the signal-to-noise of retinogeniculo-cortical information transfer, but also encode emergent features in the spike code (Sincich et al., 2009; Rathbun et al., 2010; Wang et al., 2010). Thus these synaptic mechanisms may also impart novel functionality at the level of dLGN. Further, as these mechanisms can rapidly alter the contribution of a particular retinal input to postsynaptic spiking, they may regulate the contribution of strong versus weak RGC inputs to visual processing (discussed below).

Neurotransmission Before Eye-opening

The distinct features of the immature retinogeniculate synapse suggest that the immature dLGN carries out a different set of computations on incoming retinal information than the mature dLGN. Many of the modulatory circuits that shape transmission in the adult dLGN begin to innervate TC neurons shortly before eye-opening: corticogeniculate innervation is not complete in mice until p14 (Jacobs et al., 2007; Seabrook et al., 2013; Grant et al., 2016), and cholinergic innervation develops over several postnatal weeks in cats (Carden et al., 2000). GABAergic interneurons continue to be recruited into the dLGN at the end of the first postnatal week in mice, and GABAergic innervation in rodents and carnivores occurs gradually (Shatz and Kirkwood, 1984; Ramoa & McCormick, 1994a; Pirchio et al., 1997; Ziburkus et al., 2003; Golding et al., 2014). In addition, presynaptic ultrastructural morphology and TC dendritic arbor complexity are immature at eye-opening (Bickford et al., 2010). Therefore, retinogeniculate transmission before eye-opening occurs in a very different environment than after circuits have matured.

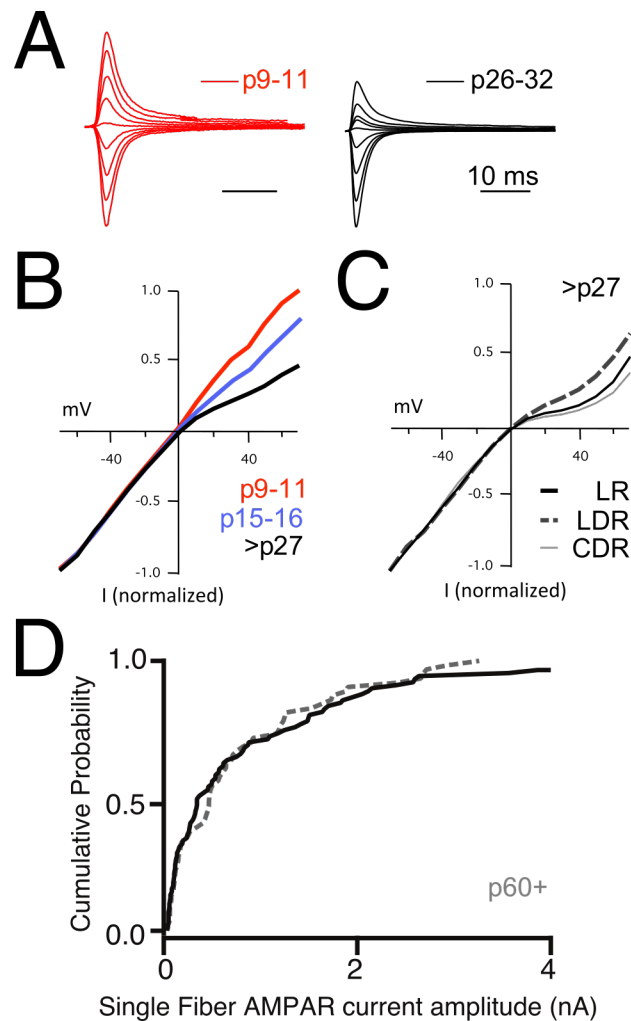


Figure 1.4: Substrates for retinogeniculate plasticity.

(A). Overlaid AMPAR current traces recorded from different holding potentials to assess the current voltage (I-V) relationship. Currents in the presence of CPP to block NMDAR currents and with spermine in the internal solution to examine the degree of I-V rectification. Calcium-permeable AMPARs exhibit a rectifying I-V relationship. Traces were recorded at 20mV increments from -60 to +60 mV holding potentials. Left-example obtained before eye opening; right, example from a mature slice. From Hauser et al, 2014. (B). Change in the average AMPAR EPSC I-V relationship over development. Rectification of I-V currents increases significantly from P9-11 to maturity, indicating a gradual increase in the contribution of CP-AMPA receptors to AMPAR-mediated currents. Modified from Hauser et al, 2014. Red: P9-11; blue: p15-16; black: P27-32. (C). Changes in AMPAR subunit composition in response to visual experience. The effect of visual deprivation from p20 (late-dark rear, LDR) or dark rearing from birth (chronic dark reared, CDR) on the AMPAR EPSC I-V relationship. Rectification of AMPAR currents is reduced in LDR but not in chronically dark reared (CDR) mice when compared to normally reared mice (light rear, LR) mice. $p=0.03$. Recordings performed at P27-32. Modified from Louros et al, 2014. (D). Comparison of the distribution of amplitudes of single fiber RGC inputs in juvenile (p27-34) and adult (P60+) mice show the persistence of weak (small-amplitude) inputs with age. Adapted from Hong et al, 2014. Reprinted with Permission.

Whereas mature TC neurons receive and integrate information from one or several strong retinal inputs that can reach several nA in amplitude, numerous weak inputs, measuring on average ~40pA in amplitude (peak AMPAR EPSC) innervate a TC neuron before eye opening (*in vitro* in mice; Hooks & Chen, 2006). Remarkably, retinogeniculate transmission to cortex does occur before input refinement: both the spontaneous patterns of activity (retinal waves) that prominently feature in the developing retina, and visually-evoked stimuli detectable through the closed eyelid influence the activity of the visual cortex (Katz & Shatz, 1996; Mooney *et al.*, 1996; Feller, 1999; Akerman *et al.*, 2002; Hanganu *et al.*, 2006; Ackman *et al.*, 2012). In slice, the synaptic charge transfer needed to drive TC neuron spiking before eye-opening is relatively small: an AMPAR EPSC with a peak amplitude of 120 pA is adequate (Liu & Chen, 2008). The coincident activation of a subset of the dozen or more converging RGC inputs, perhaps relying on synchronous activity that dominates retinal activity during this period of development, can achieve this amplitude (Wong *et al.*, 1993; Wong, 1999; Butts & Rokhsar, 2001; Feller, 2009).

Multiple mechanisms contribute to the efficacy of neurotransmission at the immature weak retinogeniculate synapse. A study using the slow calcium chelator, EGTA-AM, suggested that the distance between the presynaptic release machinery and calcium channels at retinal terminals is greater at immature presynaptic specializations, resulting in delayed or asynchronous release (Borst & Sakmann, 1996; Hauser *et al.*, 2014). Additionally, the immature nervous system produces a slower action potential waveform (Taschenberger & von Gersdorff, 2000; Murphy & du Lac, 2001) and a lower density of glutamate transporters in surrounding astrocytes (Thomas *et al.*, 2011). These properties of the immature synapse lead to the prolonged exposure of postsynaptic receptors to glutamate, promoting the integration of retinal EPSCs over a longer time scale than after maturation.

Several postsynaptic mechanisms also improve the integration of weak RGC inputs at young ages. The temporal window for postsynaptic summation is much greater before eye

opening (Liu & Chen, 2008). This is due in part to the higher input resistance in immature neurons (Ramoa & McCormick, 1994*b*; Macleod et al., 1997; Pirchio et al., 1997), as well as enhanced conduction through NMDA receptors at negative potentials because of a greater contribution of both NR2B as well as NR2C/D subunits at young synapses (Ramoa & McCormick, 1994*a*; Liu & Chen, 2008). These receptors exhibit slower decay kinetics and a lower sensitivity to magnesium block (compare between ages in Figure 1.3), and their contribution declines over development in an activity-regulated manner (Ramoa & Prusky, 1997; Chen & Regehr, 2000; Liu & Chen, 2008).

AMPA current amplitudes at the immature retinogeniculate synapse are much smaller than later in life (Figure 1.2A,1.3B). In fact, a substantial fraction (22%) of immature RGC inputs are "silent" (lacking detectable AMPAR currents; Isaac *et al.*, 1995; Liao *et al.*, 1995; Chen & Regehr, 2000). Transmission before eye opening therefore seems to rely almost entirely on NMDAR transmission, with AMPARs influencing the latency to spike (Liu & Chen, 2008). Finally, immature neurons also exhibit calcium plateau potentials (Jaubert-Miazza et al., 2005; Lo et al., 2013), and more depolarized resting membrane potentials that are closer to firing threshold (Ramoa & McCormick, 1994*b*; Macleod et al., 1997; Pirchio et al., 1997), increasing the efficacy of individual inputs.

In summary, the developing retinogeniculate synapse exhibits numerous adaptations that permit it to integrate and transfer visual signals to cortex even while it undergoes dramatic synaptic rearrangement. As these signals arise from the summation of multiple weak convergent RGC inputs, the computations that the immature dLGN performs, and therefore its role in visual processing, is substantially different from that of the mature dLGN. In addition to a role in conveying visual information, retinogeniculate transmission is important for cortical map formation (Huberman et al., 2008*b*; Cang & Feldheim, 2013; Owens et al., 2015), though its precise computational role is not yet understood.

Retinogeniculate Connectivity

Developmental Refinement of Retinogeniculate Connectivity

Retinogeniculate refinement is thought to lead to the maturation of receptive field properties in the dLGN. Before eye opening, RGC axons from the two eyes segregate into eye-specific layers: segments of the axon arbor that occupy the inappropriate layer are pruned, while the appropriately positioned portion of the arbor becomes more elaborate in a range of species (Robson, 1981; Mason, 1982; Sretavan & Shatz, 1984, 1986; Campbell & Shatz, 1992; Garraghty & Sur, 1993; Dhande et al., 2011; Hong et al., 2014). *In vitro* studies of the dLGN in rodents show that each TC neuron receives weak inputs from more than a dozen retinal ganglion cells (RGCs). Some of these inputs are subsequently pruned while others strengthen to become dominant drivers of postsynaptic activity (reviewed in Guido 2008; Huberman et al., 2008a; Hong & Chen 2011; Thompson et al., 2017). This refinement occurs over several weeks following eye opening in mice. The earliest phases depend on spontaneous input from the retina, while visual experience maintains the mature configuration and modifies connectivity via feedback from the cortex during a critical period (Hooks & Chen, 2006; Thompson et al., 2016).

The robust refinement of retinogeniculate connectivity demonstrated *in vitro* in mice corresponds temporally to the developmental transformation of initially broad, irregularly-shaped or temporally imprecise receptive fields to smaller, sharper or temporally precise ones that closely match the receptive field of the dominant retinal inputs *in vivo* (cat: Wiesel & Hubel, 1963; Daniels et al. 1978; Tootle & Friedlander, 1989; Gary-Bobo et al., 1995; Cai et al., 1997; Ferret: Tavazoie & Reid 2000, Akerman *et al.*, 2002, Davis *et al.*, 2015; primate: Blakemore & Vital-durand 1985; mouse *in vitro*: Chen & Regehr, 2000; Jaubert-Miazza et al., 2005). Surprisingly, there is a disconnect between structure and function— studies in cats, mice, and primates fail to show large-scale pruning of the axon arbor during this later window of development (Sur et al., 1984, 1987; Lachica & Casagrande, 1988; Hong et al., 2014). A recent study that examined individually reconstructed axon arbors of a subtype of mouse RGCs, the

BD-RGC (ON-OFF direction-selective RGC, Kim *et al.*, 2010), found that their size and branching complexity remain stable in the 2-3 weeks following eye opening. Instead, during the period of robust functional refinement, changes occur in bouton size and distribution along the arbor structure (Hong *et al.*, 2014). Before eye-opening, boutons are distributed broadly along the terminal arbor in mice, but gradually form tight clusters over the later window of development (for examples of mouse and cat RGC axon bouton clustering, see Figure 1.1B-C). This development suggests that an immature axon makes transient contacts with a large number of potential postsynaptic targets, but redistributes its inputs onto a few targets during the period of activity-dependent refinement. Final pruning of the arbor skeleton, however, does not occur until well after the end of the geniculate and cortical critical periods (Hong *et al.*, 2014). These findings are consistent with observations in cat and primate studies of the complexity of mature RGC axon morphology (Figure 1.1A), with multiple segments that can branch off the primary axon within the optic tract (Sur & Sherman, 1982; Hamos *et al.*, 1987; Sur *et al.*, 1987; Garraghty *et al.*, 1988; Dhande *et al.*, 2011; Hong *et al.*, 2014), although the arbors may be more restricted in the primate dLGN (Glees & Le Gros Clark, 1941; Lachica & Casagrande, 1988; Michael, 1988; Conley & Fitzpatrick, 1989). In cat, one RGC axon arbor spans the territory of far more postsynaptic neurons than it contacts (Hamos *et al.*, 1987). Reduction of the X-RGC axon arbor occurs between 4 and 12 weeks postnatal, after the peak of ocular dominance plasticity (Hubel & Wiesel, 1970; Sur *et al.*, 1984).

Therefore, while retinogeniculate development yields a circuit with appreciable functional specificity, the anatomical correlates of this process suggests latent complexity in the mature system. The breadth of the RGC axon arbor, which may impart the potential to synapse onto new TC partners even in the adult, together with short-term plasticity mechanisms that modulate the efficacy of existing contacts, provide the scaffold for dynamic computation beyond the relay of retinal firing patterns to the cortex (Alonso *et al.*, 2006; Martinez *et al.*, 2014; Usrey & Alitto, 2015),

Convergence at the Retinogeniculate Synapse

Retinogeniculate convergence (and divergence) add complexity to visual processing in the dLGN. The simplest circuit, where 1 RGC contacts 1 TC neuron, is most consistent with the concept of a thalamic “relay” (Glees & Le Gros Clark, 1941; Sherman & Guillery, 1996). Adding in complexity of additional converging RGC inputs and/or divergence of single RGC axons onto multiple targets TC neurons, however, increases the likelihood of the emergence of novel visual features or receptive field properties (Dan et al., 1998; Alonso et al., 2006; Koepsell et al., 2009; Usrey & Alitto, 2015; Weyand, 2016; Sherman, 2016). For these reasons, studies quantifying connectivity, and in particular, the degree of retinogeniculate convergence, is an active area of research.

A tour-de-force serial electron microscopy (EM) reconstruction of the synaptic contacts of one branch of an X-type retinal axon in the cat dLGN demonstrated that a RGC axon makes connections selectively rather than randomly. The reconstructed portion of the axon (reproduced in Figure 1.1A) innervated three X-cells and one Y-cell, and its inputs accounted for as much as 33%, 49%, and 100% of total innervation to the X-cells, and as little as <6% to the Y-cell. This study concluded simultaneously that a TC neuron can receive inputs from multiple RGCs (convergence), and that some of those inputs can also contact other TC neurons (divergence/multiplexing; Hamos et al. 1987). However, the single X-cell that received all of its inputs from the labeled axon remains the best-recognized result, serving as exemplary anatomical evidence for low retinogeniculate convergence. In contrast, Robson (1993) estimated that cat Y- cells receive upwards of 10 inputs per cell, suggesting that convergence varies depending on cell type.

Recent studies using new anatomical methods in p30 mice, however, came to a conclusion that counters the general view of low convergence. Morgan & colleagues used an approach that combines serial section EM with circuit tracing, to identify the presynaptic RGC axons that connect to reconstructed postsynaptic TC neurons in the dLGN. They observed at

least 40 RGC axon segments contacting one of these TC neurons (Morgan et al., 2016). Many axons also promiscuously diverged to innervate numerous other TC neurons. Hammer & colleagues reached a number closer to 10 inputs per cell from observations of bouton clustering of multicolor fluorescently labeled RGC axons (Brainbow labeling) in the mouse LGN (Hammer et al., 2015). However, these studies were not able to trace the axon segments to the primary axon, raising the possibility that they were overestimating the number of inputs to a given TC neuron. Overcoming this limitation, and despite low efficiency of rabies tracing, Rompani & colleagues showed that 1-36 RGCs innervate monocular neurons, and up to 91 RGCs from both eyes converge onto binocularly innervated neurons in the mouse dLGN. The three anatomical studies made no distinctions between X- and Y-cells, but the rabies tracing identified three different patterns of convergence in the binocular dLGN region (Rompani et al., 2017). Importantly, these studies cannot determine whether all the identified contacts are functional; many convergent inputs could be nonfunctional remnants of refinement, as final pruning of the axon arbor occurs between P30 and P60 (Hong et al., 2014). Nonetheless, these independent studies using disparate anatomical methods demonstrate that tens of RGCs may converge onto mature mouse TC neurons.

To date, most functional studies have yielded a more conservative estimate of convergence than the ultrastructural literature. In the rodent slice prep, estimates of the number of afferent inputs obtained by varying the intensity of optic tract stimulation yield numbers ranging from 1-5 (Chen & Regehr, 2000; Jaubert-Miazza et al., 2005; Ziburkus & Guido, 2006; Hooks & Chen, 2007; Chung et al., 2013; Lee et al., 2014; Dilger et al., 2015). However, this approach likely underestimates convergence due to the severing of axons in slice. It also averages across the population of TC neurons accessible with this method, with no distinction between TC neuron subtypes with different input convergence that may exist in the mouse dLGN (Krahe et al., 2011).

Estimates of retinogeniculate connectivity from carnivores and non-human primates have largely utilized recordings that assess the correlation of spiking activity of RGC-TC neuron pairs *in vivo* (Levick *et al.*, 1972; Mastronarde, 1987, 1992; Usrey *et al.*, 1998; Rowe & Fischer, 2001; Rathbun *et al.*, 2010; Cleland *et al.* 1971; Kaplan & Shapley 1984; Sincich *et al.* 2007; Carandini *et al.* 2007). Many of these experiments show that a geniculate X-cell (cat) or M or P cell (primate) receives at least one dominant input that reliably drives EPSCs preceding all or most of a TC neuron's spikes (Cleland *et al.* 1971; Cleland & Lee, 1985; Soodak *et al.*, 1987; Sincich *et al.* 2007). Others, however (especially those focusing on Y cells in cats), show that the contribution from individual RGCs exhibits greater variability, and the activity of a single retinal input rarely accounts for the entirety of the activity of its TC neuron partner (Hubel & Wiesel, 1961; Cleland & Levick, 1971; Cleland *et al.* 1971; Levick *et al.*, 1972; Mastronarde 1992). Interestingly, one study using paired recordings across both X- and Y-cells yielded examples of RGCs that drove as few as ~1% to as many as 82% of a TC neuron's action potentials (Usrey *et al.*, 1999); similar results later emerged in the Y pathway (Yeh *et al.*, 2009; Rathbun *et al.*, 2016; considered in detail in Weyand 2016). Furthermore, several studies corroborate anatomical observations of divergence, such that neurons with most closely matching receptive fields exhibit the greatest correlation among their firing patterns (Alonso *et al.*, 1996; Usrey *et al.*, 1998).

The variability in the contribution of a single RGC to postsynaptic spiking in cat dLGN is consistent with anatomical studies, if the number of contacts between a single RGC axon and thalamocortical (TC) cell relates to the functional strength of the individual input (Hamos *et al.*, 1987). The findings in cat are also consistent with *in vitro* functional data from mice. Even in adult mice (P60), the distribution of single RGC input amplitudes ranges from a tens of pA to several nA in strength (Figure 1.4D; Hooks & Chen, 2008; Hong *et al.*, 2014; Thompson *et al.*, 2016). The fact that weak convergent inputs persist into adulthood, in both cats and mice,

suggest that they have relevance for retinogeniculate function (Alonso et al., 1996; Dan et al., 1998; Usrey et al., 1999).

Taken together, the retinogeniculate circuit exhibits organization that is set up to actively tune, select, or elaborate information that is being conveyed from the retina to the cortex, suggesting that the dLGN participates in complex processing of visual information (Sherman, 2016). While similarities across species support this view, insight into the function of dLGN should come from further elucidation of the differences between mice, cat and primates.

Retinogeniculate Plasticity

In addition to short-term plasticity, the retinogeniculate circuit exhibits long-term plasticity of synaptic weights. The findings that both weak and strong inputs innervate mature TC neurons and contribute to their spiking activity highlights the possibility that experience-dependent plasticity of RGC input strength and number relies on the balancing of synaptic weights in the adult circuit (Thompson et al., 2016). The retinogeniculate connectivity map remodels to experience during development, and may also do so in mature animals. Depriving juvenile mice of visual experience for a week starting at p20 (late dark rearing) disrupts retinogeniculate connectivity, decreasing the amplitude of the average retinal input and increasing the overall number of RGC inputs onto TC neurons (Hooks & Chen, 2006, 2008; Narushima et al., 2016). This manipulation also reduces the clustering of RGC axon boutons without significantly altering the size of the arbor or the number of boutons (Hong et al., 2014). Together, these observations suggest that while connectivity between axons and targets is selective, the large size of the arbor builds flexibility into the system: dramatic change in visual experience, such as late dark rearing can resculpt connectivity by rearranging boutons and, and adjusting input strength (Louros et al., 2014) without investing into remodeling the entire axonal arbor. Because excess branches of RGC arbors do not prune down until at least P60 in mice, retinogeniculate connectivity may exhibit substantial plasticity until at least this age (Hong et al., 2014).

A well-established mechanism for altering synaptic strength in response to activity or experience is through changes in AMPAR content of the post-synaptic density (Huganir & Nicoll, 2013). Several studies link the regulation of AMPAR trafficking and function to modulation of the strength of juvenile retinogeniculate synapses. The retinogeniculate synapse is one among several synapses that recruit GluA1-containing AMPARs in response to sensory stimulation (Clem & Barth, 2006; Kiehl et al., 2009; Louros et al., 2014), suggesting that GluA1-dependent AMPAR-driven forms of transmission play an important role in the development and plasticity at this synapse (Figure 1.4A-C; activity-dependent changes in AMPAR subunit composition reviewed in Cull-Candy et al. 2006; Liu & Zukin 2007; Lee et al. 2014). AMPAR subunit context is sensitive to visual experience: mice subjected to late dark rearing exhibited a decrease in AMPAR current rectification, a measure of the fraction of calcium-permeable to calcium-impermeable AMPARs in the postsynaptic density. In contrast, mice that never had any visual experience (chronically dark reared from birth) exhibited normal rectification (Figure 1.4C; Louros et al., 2014). Experience-dependent changes in AMPAR content and function at the retinogeniculate synapse rely in part on stargazin, a transmembrane AMPA regulatory protein that modifies the trafficking and channel kinetics of AMPARs (Straub & Tomita, 2012). Indeed, late dark rearing increases the expression and phosphorylation of stargazin, which can in turn regulate the composition of postsynaptic AMPARs in both a Hebbian (Tomita et al., 2005) or homeostatic manner (Louros et al., 2014). Finally, changes in AMPAR expression also mediate the role of MHC class I molecule H2-D^b in retinogeniculate developmental refinement (Lee et al., 2014). H2-D^b is one of a series of immune-related molecules that shape retinogeniculate development (Shatz 2009; Schafer & Stevens 2010). Mice lacking H2-D^b expression exhibit an increase in calcium-permeable AMPARs at retinogeniculate synapses, corresponding to a deficit in LTD. Together, these studies bespeak a critical role of AMPAR regulation in retinogeniculate synaptic plasticity, which may persist into adulthood.

Both Hebbian and homeostatic mechanisms of synaptic plasticity have been shown to alter retinogeniculate synaptic strength during development (Mooney et al., 1993; Butts et al., 2007; Ziburkus et al., 2009; Krahe & Guido, 2011; Lin et al., 2014; Louros et al., 2014). High frequency stimulation of the optic tract, or low frequency stimulation coincident with postsynaptic depolarization in slices from immature ferret dLGN result in long-term enhancement of the EPSC, with contribution from NMDAR activation (Mooney et al., 1993). However, in rat, the same high-frequency stimulus results in long-term depression in dLGN explants before eye-opening, but long-term potentiation later in development (Ziburkus et al., 2009). Finally, plasticity rules based on burst timing have been identified before eye-opening (Butts et al. 2007 in rat), but these plasticity rules have not been examined in more mature slices. On the other hand, the contribution of homeostatic plasticity in retinogeniculate plasticity has been suggested through studies involving monocular deprivation, chronic dark rearing, manipulation of stargazin, and deletion of *Mecp2* (a transcription factor necessary for homeostatic scaling up in the visual cortex; Blackman et al., 2012; Noutel et al., 2011; Krahe & Guido, 2011; Lin et al., 2014; Louros et al., 2014). Similar paradigms likely also drive synaptic plasticity at the fully mature retinogeniculate synapse.

Recently described instances of rapid plasticity across species could also engage Hebbian or homeostatic mechanisms at the retinogeniculate synapse and cause a shift in the strength of individual retinogeniculate inputs (Moore et al., 2011; Aguila et al., 2017). In fact, dLGN neurons readily adapt to changes in visual input. For example, pharmacologic blockade of On-center RGC activity in adult cats rapidly uncovers Off-center responses in dLGN neurons previously exhibiting On-center responses, instead of silencing them (Moore et al., 2011). Further, acute suppression of cortical feedback in awake monkeys shifted the receptive field position of a subset of TC neurons (Aguila et al., 2017). Finally, rabbit geniculate neurons exhibit bidirectional sensory adaptation that improves signal detection (Stoelzel et al., 2015). While modulatory mechanisms could shape the response of the TC neuron to rapid changes in

upstream inputs, the specificity that TC neuron responses exhibit in these studies indicates instead a role for rapid shifts in the synaptic efficacy of retinogeniculate connections. These changes occur too rapidly to rely on structural rearrangements of retinogeniculate connections, their timecourse is consistent with possible unsilencing or strengthening of functionally silent or weak subthreshold inputs via the insertion of postsynaptic receptors at dormant synaptic sites. Of course, local inhibitory circuits may also contribute to rapid shifts in RGC input efficacy (Fisher et al., 2017). Changes that occur over days rather than hours may also recruit the redistribution of presynaptic boutons along the broad RGC axon arbor. The capacity of the diverse types of retinogeniculate synaptic contacts for functional plasticity remains unexplored.

The expression of a variety of mechanisms for modification of synaptic weights is layered on top of a potentially densely interconnected network that is evident in considerable retinogeniculate divergence and convergence. Combined with the observation that both weak and strong inputs innervate mature TC neurons, these plasticity mechanism may endow the dLGN with a role in visual learning on multiple time scales (Ramos et al., 1976; Albrecht et al., 1990).

Conclusion

Recent work is revealing new complexities of retinogeniculate transmission and circuit organization that further expand the potential role of the dLGN in visual processing beyond its classic attributes (Steriade et al., 1997; Sherman & Guillery, 2001). The morphological diversity of synaptic motifs and complex connectivity patterns, combined with short- and long-term plasticity mechanisms of the retinogeniculate circuit demonstrate that the retinogeniculate synapse makes substantial and dynamic contributions to the processing of visual information. Weak or non-dominant retinogeniculate inputs in the mature dLGN, which have repeatedly been dismissed as insignificant, as errors of development or leftovers from developmental plasticity with no functional relevance (Sur et al., 1984; Garraghty et al., 1985; Hamos et al., 1987), likely

enhance extraction of visual features in the geniculate and visual cortex, and serve as strategic reserves of plasticity. Moreover, the convergence of potentially heterogeneous RGC inputs onto single geniculate neurons could give rise to new receptive field features such as orientation selectivity in mouse dLGN, as recently proposed (Stafford & Huberman, 2017). Finally, the interplay between the strength and short-term plasticity properties of RGC inputs in the context of convergence and divergence adds to the richness of the dLGN circuitry.

Much is still left to understand about the extent and underlying basis of plasticity in the dLGN. However, the idea that the mature geniculate system can utilize activity-dependent plasticity mechanisms to fine-tune the contribution of its individual inputs in response to novel visual challenges, experiences, changes in modulatory state, or retinal degeneration appears to be rapidly gaining experimental support. Future studies are needed to clarify the differences in the number of inputs that converge onto TC neurons between species, because the results may correlate with the degree by which new receptive field features emerge at the level of dLGN. Elucidation of whether and how weak inputs contribute to visual processing in different species will also uncover the richness of thalamic function.

The continually expanding toolbox for interrogating diversity in neuronal circuits is already uncovering nuances in the contribution of different RGC types to TC neuron function (Storchi et al., 2015; Denman et al., 2016). Advances in methods for labeling, activating, and measuring the activity of different neuronal populations that have been deployed extensively in mice may also reveal underappreciated subtleties of retinogeniculate transmission in other species (Scholl et al., 2013; Zaltsman et al., 2015; Zeater et al., 2015; Suresh et al., 2016). Shifting models of the organization of the visual system that take into account the important nuances of retinogeniculate functional organization and plasticity are certain to provide new models of visual system development and function.

CHAPTER 2:

Materials and Methods

Attributions: This chapter combines methods that were published as supplemental materials in Hong YK, Park S, Litvina EY, Morales J, Sanes JR, Chen C. Refinement of the retinogeniculate synapse by bouton clustering. *Neuron*. 2014 Oct 22;84(2):332-9, included here as Chapter 3, with additional details related to Chapters 4 and 5. Sections that are reproduced verbatim or include text from Hong et al, 2014 are clearly marked in the text.

All animal procedures were in compliance with the NIH Guide for the Care and Use of Laboratory Animals and approved by the Institutional Animal and Care and Use Committee (IACUC) at Children's Hospital, Boston.

Transgenic Animals (expanded from Hong et al, 2014)

Animals were maintained on a C57/BL6(J) background. All mouse lines, with references and sources, used for these studies are listed in Table 2.1. Among these are several Cre lines we screened that proved not to label RGCs with sufficient specificity and/or reliability when crossed with the Ai32 reporter line; data from these studies are not included in this dissertation.

For anatomical characterization (Chapter 4, 6) JAMB-Cre-ER and BD-CRE-ER animals were crossed with reporter Thy1-STOP-YFP mice, which express yellow fluorescent protein (YFP) and / or Ai14 mice, which express TDTomato fluorescent protein under a CAG promoter following Cre-mediated excision of a stop sequence (Madisen et al, 2012).

For functional characterization (Chapter 4, 5), Chx10-Cre, BD-Cre-ER, JamB-CreER and CART-Ires2-Cre mice maintained as homozygotes or heterozygotes were crossed with homozygous Ai32 mice yielding progeny heterozygous for each gene and expressing ChR2 in the RGCs (and other layers of the retina—none of the lines examined label purely RGCs). The resulting crosses are referred to as "*Chx10;ChR2*," "*BD;ChR2*" and so on.

A low tamoxifen dose of 1.5-4 $\mu\text{g/g}$ at p0-10 was used for sparse (1-20 RGCs) labeling of BD and J RGCs (Chapter 3); 100-300 $\mu\text{g/g}$ yielded dense labeling (Chapters 3, 5), and was used for control experiments comparing the effect on tamoxifen on retinogeniculate refinement in *Chx10;ChR2* mice. Higher doses of tamoxifen unacceptably raised neonatal mortality.

For functional studies, animals aged p27-34 were included in the "p30" category, P60-100 in "P60," and P9-10 C57BL/6J wild-type (WT) in "P9."

Table 2.1: Animal Lines Used.

Mouse line	RGCs labeled	Reference	Jax #	Notes	Used in Chapter	Obtained From
Selective Cre lines						
BD-CreER	bistratified, ON-OFF direction selective retinal ganglion cells (BD-RGCs), downward motion	Kim et al., 2010		also known as FSTL4-CreER or KIAA-CreER; BAC transgenic	3, 5	Joshua Sanes lab
CART-IRES2-Cre	bistratified, ON-OFF direction selective retinal ganglion cells (BD-RGCs), multiple directions	Kim et al., 2010; Martersteck et al., 2017	028533	knock-in	5	Hongkui Zeng/Allen Brain
JAMB-CreER	J-RGCs, OFF-RGCs selective for upward motion	Kim et al., 2008		BAC transgenic	3, 5	Joshua Sanes lab
Chx10-Cre	all/most RGCs	Rowan & Cepko, 2004	005105	BAC transgenic	4, 5	Connie Cepko Lab
HB9-GFP	bistratified, ON-OFF direction selective retinal ganglion cells (BD-RGCs), downward motion	Arber et al., 1999, Trenholm et al., 2011	005029	transgenic	5	Elizabeth Engle Lab
Non-selective or variable cre lines (data not shown; hetxhet cross with Ai14 or Ai32) examined						
KCNG4-Cre	alpha-RGCs	Duan et al., 2015	029414	variable expression among RGCs/nonspecific labeling in dLGN; knock-in	not used	Joshua Sanes / Zhigang He labs
Hb9-Cre	no RGCs labeled	Arber et al., 1999	006600	targeted mutation	not used	Elizabeth Engle Lab
Rbp4-cre	Several RGC types	Sabbah et al., 2017		Transgenic	not used	Michael Greenberg Lab
Reporter Lines used						
Thy1-STOP-YFP line #15	YFP reporter	Buffelli et al., 2003		THY1 promoter	3, 5	Joshua Sanes
Ai14	TDTomato reporter	Madisen et al., 2012	007908	CAG promoter	5	Beth Stevens Lab
Ai32	ChR2 (H134R) YFP fusion reporter	Madisen et al., 2012	12569	CAG promoter	4, 5	Jackson Labs

Tissue preparation and immunohistochemistry (expanded from Hong et al, 2014)

Mice were anesthetized and transcardially perfused with 0.1M phosphate buffered saline (PBS) immediately followed by 4% w/v paraformaldehyde (PFA) in PBS. Brains were post-fixed overnight in 4% PFA at 4°C and rinsed in PBS. 100 μ m sagittal or 60 μ m coronal sections were made with a vibratome (Leica VT1000). Retinae in Chapter 4, Figure 4.1 were sectioned on a Leica CM3050S cryostat at 16 μ m thickness. The parasagittal slice from an *in vitro* electrophysiology experiment shown in Chapter 4, Figure 4.1A was incubated in 4% PFA for 20 minutes after the end of the experiment and then stored in PBS until immunohistochemistry was performed. Retinae and acute slices were post-fixed after most acute electrophysiology experiments described in Chapter 5. This tissue was used to confirm the density and specificity of labeling.

For young mice (P8-16), we also compared brains dropped directly into 4% PFA to those fixed by transcardial perfusion. We found that the two methods provided comparable quality tissue and labeled axon arbors. Axons arbors from drop-fixed brains were also included in the data sets. Dissected whole mount retinae were post-fixed in 4% PFA for 15-30 min, incubated with primary antibody in 0.5% Triton-X/PBS and 2% donkey serum for 2-3 days, followed by secondary antibody (donkey anti- rabbit Alexa-488, and goat anti-guinea pig Alexa 555 or 594, Invitrogen).

Native YFP fluorescence was amplified using anti-GFP primary antibody staining. Primary antibodies used: rabbit anti-green fluorescent protein (GFP) (1:2000, Millipore), Chicken anti GFP(AVES GFP-1020 1:1000), guinea pig polyclonal anti-vesicular glutamate transporter vGLUT2 (1:2000, Millipore), Guinea-pig polyclonal anti-vesicular glutamate transporter VGLUT1 (1:1000 AB5905, Millipore, MA), mouse monoclonal anti-SV2 (Developmental Studies Hybridoma Bank), and unphosphorylated neurofilament, mouse anti-SMI-32 (1: 1000, Covance), and mouse anti NeuN (1:1000, Millipore MAB 377), Rabbit-anti-CART (H-003–62; Phoenix Pharmaceuticals). Secondary antibodies used: donkey anti-rabbit antibody conjugated to Alexa

Fluor 488 (1:2000, Invitrogen), donkey anti-rabbit antibody conjugated to Alexa Fluor 647 (1:1000, Invitrogen), donkey anti-guinea pig conjugated to Alexa Fluor 555 or 596 (1:1000, Invitrogen), donkey anti-mouse 647 (1:1000), goat anti-mouse 555(1:1000, A31570), goat anti chicken 488 (A11039), and goat anti GP 555 (21437). Tissue was then incubated with DAPI for nuclear detection, mounted and coverslipped with Vectashield (VectorLabs).

Image acquisition (expanded from Hong et al, 2014)

Mouse retinae and brain sections were screened for the presence of YFP positive RGCs under an epifluorescence microscope (Nikon 80i). Images were acquired with a laser scanning confocal microscope (Zeiss LSM 700 or 710) equipped with 4x-60x objectives and a solid-state laser with laser lines 405 nm (5 mW), 488 nm (10 mW), 555 nm (10 mW), 639 nm (5 mW) and a variable secondary dichroic beam splitter. Regions of interest were imaged with 10x (0.25NA, air), or 25x (0.8 NA), 40x (1.3 NA), 63x (1.4 NA), or 60x (1.4NA) oil immersion objectives (Zeiss, Olympus). Tiling (Figure 4.3A) was automated with built-in functions in Zeiss imaging software on the LSM 710. Retina images for Figure 5.8 were obtained on the Olympus DSU inverted spinning disk confocal using a 20X air objective. The image of the retinogeniculate slice in Figure 5.3 of the last study was taken with an Iphone 4S camera through the oculus of the rig microscope.

Image Analysis

Methods exclusively used in Chapter 3 (reproduced verbatim from Hong et al, 2014)

Axons chosen for this study: The axon morphology of BD-RGCs displayed regional differences in size depending on the target location in the LGN, similar to those previously described in the superior colliculus for BD-RGC axons (Hong et al., 2011). Axon terminals within the medial side (where the curvature of the LGN region is greatest and tapers to a point) tend to be smaller, while those in the lateral most LGN where the nucleus is larger, tend to be large. In

order to minimize variability of axon morphology, we restricted this study to axons within a limited zone within the LGN (Supplementary Figure 7.1B). Specifically, we studied contralaterally-projecting axons that were restricted to the dorsal LGN, excluding 150-200 μ m on the most medial and lateral edges of the LGN. This region was chosen because our previously published electrophysiological data was obtained from this zone, and BD axons were most frequently found in this area.

Axon Branching Analysis: For single cell morphology studies, only samples that had 1-2 well-separated RGCs in the retina were used for reconstruction. Semiautomatic tracing of a confocal image stack was performed with the Simple Neurite Tracer ImageJ plugin (Fiji). Axon arbors spanning more than a single section were digitally aligned using Autoaligner (Bitplane) using tissue boundaries and the traversing axon as fiduciary markers. Image stacks were concatenated into a single stack (ImageJ) so the RGC arbor could be fully reconstructed. 3D masks were generated from filled traces in imageJ and imported into Imaris for quantitative analysis—total arbor length, the number of branches, the number of terminals branch length, branch depth, and the number of branch points for each of the 3-D retinogeniculate arbors reconstructions were quantified. Primary axons of BD-RGCs originate from the retina and tend to traverse along the dorso-lateral shell of the LGN and continue on to project to other regions, predominantly to the superior colliculus. Axon collaterals that enter the LGN are considered here to be secondary branches. The secondary branches extend into the LGN with few off-shoots until it reaches the target area deeper within the LGN. Thus, the secondary branches vary in length depending the location of the target area. In order to normalize axons for different locations, we therefore used only the tertiary and higher order axon branches for analysis, and not the primary or secondary axon branches. The volume of the axon was taken to be the convex hull of 3 dimensional space encompassing the axons' tertiary or higher order branches. Volumes were quantified using Imaris software (Bitplane).

Bouton Identification: The numbers and locations of boutons were quantified semi-automatically using the Spots tool in Imaris. We added an additional filter by which only spots marking regions of axons that were > 2 times wider than the surrounding axon segment ($< 10\mu\text{m}$ on either side of the varicosity) were counted as boutons. As a rule, we determined that an axon was unfit for analysis if the primary axon, where boutons should not be present, had varicosities. These were likely due to poor fixation and were excluded from this study. Width measurements were taken as the full-width half max (FWHM) of the intensity profiles of a line drawn perpendicular to the axon segment or bouton. Large boutons were counted as single boutons if the varicosities were not resolvable. The number of boutons at older ages is thus likely an underestimate of the actual number. **Clustering Analysis** Nearest neighbor distance: We chose to measure Euclidian distances between boutons rather than the distance along the branch because RGC axons often take circuitous routes, and clusters are often formed by converging boutons from different branches of the same axon. Analysis was done with custom written macros in Matlab.

Bouton Distribution Comparison of clustering was done by quantifying the nearest neighbor distance (NN) and clustering bouton positions as point processes using mean-shift clustering.

Mean-shift clustering analysis: We applied a mean-shift clustering algorithm to objectively define clusters formed by boutons. Mean-shift clustering is a nonparametric clustering analysis that does not require a priori knowledge of the number or shape of clusters to be defined (Comaniciu et al., 2002; Fukunaga and Hostetler, 1975). Similar methods have been used to define clustering of boutons in visual cortex (Binzegger et al., 2007). The positions of boutons were treated as point processes in 3 dimensional space. The BD axons have regions where bouton density is high relative to its surrounding, forming “islands” of high density surrounded by low density regions. We first qualitatively determined areas of the axon arbor that were distinctly clustered by subjective observers, and found that the average pair-wise distance

between the boutons within the clusters were $\sim 5 \mu\text{m}$. We chose this as the search radius (kernel size). Thus, this parameter is not meant to provide an absolute measurement of bouton clusters, but rather, allow for comparison of the relative degree of clustering (boutons/cluster) at different developmental phases. A bouton cluster was defined as areas that contained 3 or more points. Analysis was done using custom software in Matlab, using a flat kernel for mean-shift clustering.

Colocalization of boutons and presynaptic marker controls: Colocalization of VGLUT2 and YFP was quantified using the semiautomatic colocalization threshold and highlighter tools in ImageJ. Briefly, the colocalization highlighter used threshold values of the individual channels to create a mask for regions where YFP or VGLUT2 channels overlap. This mask was then superimposed on the original YFP channel.

An additional control included an assessment of the degree by which colocalization of VGLUT2 and varicosities could occur by chance. The fraction of co-localization that occurred when the VGLUT2 channel was rotated 180° relative to the GFP channel for each image that we analyzed was $26.7 \pm 9.9\%$ at P8, and $17.2 \pm 11.3\%$ at >P20 ($n=10$ each, SEM, $p=0.04$, student t-test). This difference is consistent with our finding that VGLUT2 staining alone also clusters with age, thus there is a reduced likelihood that colocalization occurs in the old when compared to the young. However, Monte Carlo simulations demonstrated that changes in random colocalization over age did not affect our interpretation of bouton clustering. From 1000 iterations, 27% and 17% of boutons were randomly removed from our bouton localization data set of P8 and P20 arbors, respectively, and the average nearest neighbor distance for the two age groups was calculated. As expected, removal of boutons led to an increase in average nearest neighbor distance for both age groups (from 4.3 ± 0.8 to $4.8 \pm 0.9 \mu\text{m}$ at P20; 5.6 ± 0.8 to $6.5 \pm 0.8 \mu\text{m}$ at P8). However, the nearest neighbor distance was still significantly smaller at P20 than at P8, consistent with an increase in clustering with age (student t-test, $p=0.001$). In addition, there was no detectable difference in the average number of boutons/arbor with age.

Therefore, the scoring of varicosity distribution over development is a reliable method for quantifying bouton clustering.

Image Quantification Methods for Chapters 4, 5:

For quantification of primary visual cortex (V1) *Chx10:ChR2* (YFP) labeling, tiled Z-stacks of YFP and NeuN signal in 60 μ m-thick sections of V1 were acquired on the Nikon Ti Eclipse inverted microscope using a 10x objective; YFP⁺ neuronal cell bodies were counted manually in FIJI using the cell counter plugin. 4 sections each from 4 mice were used for this quantification. Across these sections, there were 14.2 \pm 1.82 (mean \pm SEM) YFP⁺ neurons per V1 L6 section; projection neurons were not distinguished from local interneurons. The number of YFP⁺ neurons was converted to a population percentage using a manually-obtained density of NeuN⁺ cell bodies. This calculation showed that 0.35 \pm 0.009 (mean/SEM)% of NeuN⁺ cells in V1 expressed YFP; in Layer 6 of V1, only 0.381 \pm 0.016 % of NeuN⁺ cells were YFP⁺.

For Chapter 5, Figure 5.1 and 5.8, a preliminary subset (3 fields of view taken at 20x, 3 animals each for BD; 1 randomly selected field of view, 3 animals for CART) of a larger set of images acquired on the spinning disk were used to assess colocalization between signals corresponding to GFP, Brn3A, CART, and DAPI (Figure 5.1) or ChR2-TdTomato, ReachR-mCitrine, DAPI, and CART (Figure 5.8). Preliminary quantification was performed manually and without blinding. To assess the effect of tamoxifen on the density of RGCs, retinæ from 3 HB9-GFP animals injected with high doses of tamoxifen neonatally and 3 animals receiving no injections were compared. Four fields of view were counted and density of RGCs per unit area was compared between groups. To quantify the number of RGCs labeled in *BD;ChR2* retinæ, retinæ from a subset of animals used for acute experiments were immunostained for GFP, flat-mounted, and tiled images of the entire retina were manually collected on the 80i epifluorescent scope using a 10x or 20x objective depending on tissue condition, and were reassembled in Photoshop (Adobe). The number of RGCs was then manually quantified using ImageJ.

In Chapter 5, we use CART immunohistochemistry to identify direction-selective RGCs based on Kay et al, 2011. That study used a random RGC labeling in a Thy1-YFP-H line to show that all CART-immunopositive RGCs exhibit OODSRGC morphology, and more than 95% of YFP⁺ neurons in BD;STP-YFP and DRD4-GFP mice (another OODSRGC-subtype-specific GFP line) are CART-immunopositive at p7. CART also labels amacrine cells, which is the reason we combine immunohistochemistry for CART with Brn3A whenever possible to help identify RGCs (Kay et al, 2011). Therefore, CART immunohistochemistry yields a reliable marker for the identification of OODSRGCs.

Electrophysiology Methods

Slice Preparation

Brain slices containing the optic tract (OT) and LGN were obtained from mice according to a procedure originally developed for retinogeniculate slice experiments in rat (Turner & Salt, 1998) and later adapted for mouse (Chen & Regehr, 2000). Briefly, mice were anesthetized using isoflurane and after decapitation the head was quickly cooled. The brain was then carefully and quickly removed and immersed in oxygenated ice-cold cutting solution containing (in mM): 130 mM K-gluconate, 15 mM KCl, 0.05 mM EGTA, 20 mM HEPES, and 25 mM glucose (pH 7.4) with NaOH (Pressler and Regehr, 2013) for about 30-60 seconds. We found that this cutting solution and maximal cooling of the head and brain improved viability of slices from mice up to and older than p100. The brain was then placed on filter paper for a blocking cut with a steel razor blade placed about 5° off the midline in the left hemisphere for a parasagittal slice orientation. The flat surface created by this cut was then used to glue the brain to a plexiglass wedge angled at 18° from the horizontal on the left side. 250 µm-thick parasagittal slices were sectioned in the cutting solution using a sapphire blade (Delaware Diamond Knives, Wilmington, DE) on a vibratome (VT1200S; Leica, Deerfield, IL) and were allowed to recover at 31°C for 25-35 minutes in oxygenated (95% O₂/5% CO₂) saline solution (in mM: 125 NaCl, 26

NaHCO₃, 1.25 NaH₂PO₄, 2.5 KCl, 1.0 MgCl₂, 2.0 CaCl₂, and 25 glucose (Sigma) adjusted to 310-315 mOsm). Slices were maintained in circulating oxygenated saline solution throughout the duration of acute slice electrophysiology experiments.

Acute Slice Electrophysiology

Slice recordings were made using an Axopatch 200B (Axon Instruments, Foster City, CA), filtered at 1Khz, and digitized at 4-50 kHz with an ITC-16 interface (Instrutech). Thalamocortical neurons were patch clamped in the monocular, mid-to-caudo-ventrolateral region of the dLGN for optimal OT stimulation. DIC optics (Olympus) projected to a separate monitor were used to visualize TC neurons. Whole-cell voltage clamp recordings of TC neurons were performed using glass pipettes (1–2.0 MOhm resistance, Drummond Scientific, Broomall PA pulled on Sutter p87 Flaming/Brown micropipette puller from Sutter Instruments) filled with an internal solution consisting of (in mM): 35 CsF, 100 CsCl, 10 EGTA, 10 HEPES, and the L-type calcium channel antagonist, 0.1 methoxyverapamil (290-300 mOsm, pH 7.3; Sigma). Cells were held at 0mV between trials. For most experiments, trials at -70 mV and +40 mV holding potentials were alternated to isolate AMPAR and access NMDAR current components. Access resistance was monitored throughout the experiment and evaluated in offline analysis. Intertrial intervals were usually 20-25 seconds; they were extended to 40 seconds for experiments where only the amplitude of NMDA receptor currents was measured. Because of the slow recovery from light-induced inactivation of ReachR red-shifted opsin, intertrial intervals preceding ReachR stimulation trials were extended to 60 seconds.

All experiments were performed at room temperature in oxygenated saline solution containing 20 μ M bicuculline (Sigma). In addition to bicuculline, experiments that were designed to compare the amplitude, timecourse, and paired-pulse properties of maximal eEPSC, oEPSCs, and fEPSCs (those presented in Figs 4.3F-G, 4.2 D-F), the following drugs were included in the bath: 50 μ M cyclothiazide to block AMPAR desensitization, 20 μ M CPP to block

NMDAR currents, 10 μ M DPCPX to block A1 adenosine receptors (Yang et al., 2014), 50 μ M LY341495 to block presynaptic mGluRs (Kingston et al., 1998; Hauser et al., 2013), and 2 μ M CGP55845 to block GABA_B. Experiments to assess the development of ChR2 expression using NMDAR currents (Figure 4.9 A-C) were performed in the presence of bicuculline along with 2 μ M CGP55845, 10 μ M DPCPX, and 5 μ M NBQX to block AMPAR currents.

We chose a transgenic strategy over viral-mediated infection to express ChR2 for optogenetic activation of RGC axons in order to avoid damaging the retina and to reduce variability of ChR2 expression level between RGCs and between mice. Viral vectors may also distort presynaptic release, confounding a quantitative analysis of retinogeniculate convergence (Jackman et al., 2014).

Optic Tract Stimulation

Three types of axonal stimulation were used in this study.

For electrical stimulation (to evoke an “eEPSC” referred to in Chapters 4 and 5), a pair of electrodes, filled with saline solution, was placed in the OT in a location that optimized the maximal evoked current. Electrical stimuli were 0.25 msec in duration and ranged in amplitude from 5-400 μ A (100-400 μ A stimuli were used to obtain the maximal eEPSC response, WPI A365). Multiple locations along the portion of the OT bordering the vLGN were sampled to obtain the optimal response; care was taken to avoid stimulating corticothalamic axons at the dorsal edge of the vLGN.

For full-field stimulation of a maximal ChR2-mediated EPSC (the “oEPSC”), a CoolLED pE unit supplied 470nm light through a 60x objective (Olympus LUMplanFL N 60x/1.00W), measuring 83 mW/mm² maximal light intensity (A CoolLED pE 565 unit was used for dual channel experiments in Chapter 5, with maximal light intensity measuring 16.5mW/ mm²). 470nm full-field stimuli were 1-4 msec long with power set at maximal 83 mW/mm² intensity to obtain the maximal oEPSC except in Figure 4.4E-F and 4.9C, where the duration and/or

intensity of full-field stimulation were varied to describe the development of sensitivity of ChR2. 565nm full-field stimuli were 10 msec long. In experiments comparing multiple measurements from the same cell, such as different stimulation types in Figure 4.3F-G and 4.4 B, D-H, or different stimulus intensities in Figure 4.9C, varying trials were interleaved pseudorandomly.

For optical stimulation of the ChR2-expressing OT bundle at a distance from the axonal terminals (to evoke an “fEPSC”), a 200 μm -thick optic fiber, 0.39nA (Thorlabs) was threaded through the barrel of one of the glass stimulating electrodes. The fiber was then positioned over a similar location in the OT as electrical stimulation, taking care to avoid overlap between the light spot and the soma of the patched TC neuron, and lowered onto the tissue, with a resulting elliptical $\sim 1\text{mm}^2$ spot of blue light (0.5 x 0.7 mm) over the OT. 470nm illumination was provided by a CoolLED pE-100^{fiber} system for this fiber (Max light intensity through fiber: 49 mW/mm² (Scientifica). Optic fiber stimuli ranged from 1-4 msec in and from ~ 0.5 -49 mW/mm² in intensity; the maximal intensity was always used to obtain the maximal fEPSC. This fiber set up was also used for 470nm light stimulation in dual channel experiments in Chapter 5. In this case, the fiber hovered above the tissue and the light spot was deliberately positioned to center on the soma to evoke the maximal ChR2-driven oEPSC. 10 msec durations were used for this experiment. Light intensity was measured offline using Thorlabs Compact Power and Energy Meter (PM100D) coupled to a photodiode (S130C). The length of stimulus indicators in figures corresponds to the duration of stimulation used for in individual example experiments.

Single Fiber Stimulation

Single Fiber responses were isolated with either electrical or optical stimulation (through the fiber). A window displaying a ~ 150 pA amplitude range around the baseline in the Igor interface was used to monitor the result of each stimulation during single fiber isolation experiments to ensure that small single fibers were not missed due to display scaling.

To isolate single RGC fiber responses using electrical stimulation, the amplitude of the

stimulus was systematically varied from minimal by increments of $0.25 \mu\text{A}$. Procedures for ascertaining single fibers and silent inputs were followed as discussed in previous publications from the lab (Hooks & Chen, 2006, 2008; Noutel et al., 2011). Another input clearly isolated and at least 5x greater in peak amplitude than the first was also counted as a single fiber. In some cases, second or third fibers were obtained by moving the stimulus to a different location in the OT.

To isolate single fibers using ChR2, blue light minimal stimulation delivered through the optic fiber over the OT was used. The CoolLED control panel provides the ability to increment light intensity by $0.1\text{-}0.15 \text{ mW/mm}^2$ steps up to $\sim 15 \text{ mW/mm}^2$, and at $0.05\text{-}0.1 \text{ mW/mm}^2$ increments up the max intensity (49 mW/mm^2). We took advantage of these small increments to isolate single ChR2-expressing retinal inputs. Both 50% failure and threshold methods of single fiber isolation were adapted and tested for blue light stimulation. In both cases, a narrow range of light intensities around the threshold of a minimal response to stimulation was first identified manually by incrementally varying the light intensity between $\sim 0.5\text{-}15 \text{ mW/mm}^2$ by increments of $\sim 0.1\text{-}0.3 \text{ mW/mm}^2$. For the 50% failure method, stimulation intensity was lowered to the bottom of this range following initial determination of the relevant range of intensities. In the example shown in Figure 4.5Aii, 23 waves were first recorded at the lower intensity (5.41 mW/mm^2), and then the intensity was increased by incrementally (to 5.54 mW/mm^2) and 75 waves were recorded. The probability of obtaining a response for these two intensities was then calculated by dividing the number of trials yielding an EPSC over the total number of trials recorded at that intensity of stimulation ($2/23$ and $37/75$, respectively). For the threshold approach, which was used to obtain the majority of optical single fiber responses, stimulation intensity was lowered 1-2 increments below the bottom of the pre-determined range, and then increased every 2-4 trials until a response could be reliably evoked. As with electrical stimulation, we then gradually increased the stimulation to determine whether a second single fiber could be isolated. Also as with electrical stimulation, the single fiber response sometimes first emerged in response to the

second of two stimuli delivered 50-msec apart before appearing in response to the first stimulus at the next light-intensity increment (Noutel et al., 2011).

Data Acquisition and Analysis (Expanded from Hong et al, 2014)

Data acquisition and offline analysis was performed using custom software written in IgorPro (Wave-Metrics, Portland, OR), Prism (GraphPad Software, Inc.), JMP (SAS Institute) and Excel (Microsoft, Redmond, WA). EPSC kinetics and paired-pulse ratios were calculated using averages of 3-5 trials. EPSC halfwidth (Table 4.2) was computed between the time-point in the rising and falling phases of the EPSC at which the amplitude was 50% of the peak. To normalize based on EPSC amplitude, the halfwidth value was divided by the amplitude.

All data sets were evaluated for normality using the Kolmogorov-Smirnov test. For nonparametric distributions, the Mann-Whitney ("MW") or Wilcoxon signed ranks test were used for unpaired or paired comparison. For multiple comparisons of nonparametric data, the Kruskal-Wallis ("KW") ANOVA with post hoc Dunn's multiple comparison test was used. For normally distributed data sets, we used the Student's t test and one-way ANOVA with Tukey's multiple comparison test. For all figures, * $p < 0.05$; ** $p < 0.01$; *** $p < 0.001$. In Chapter 3, for groups P8, P12, P16, P20, P31, P60, and LDR at P31, $n = 8, 8, 8, 7, 12, 11$, and 8, respectively. Unless otherwise specified, all box plots indicate the median (line within box), 25-75% quartile range (box), and 10-90% range (whiskers). Amplitudes are generally reported in nA unless otherwise specified. N's for each experiment are noted in figure legends and/or tables.

Fiber Fraction Assessment

Afferent convergence was calculated by computing the fiber fraction (single fiber current amplitude/maximal current amplitude) for each single fiber and separately for AMPAR and NMDAR currents (Hooks & Chen, 2006, 2008); these values were then averaged to obtain a single fiber fraction value for each cell. Separate fiber fractions were calculated using synaptic

currents evoked with optical or electrical stimulation. Electrical single fiber and maximal amplitude were used to calculate the electrical fiber fraction (eFF); single fibers isolated with the optic fiber stimulus and oEPSC maximal currents were used to calculate the optical fiber fraction (oFF).

Data Comparison from Prior Publications

The data presented in Figure 4.6 summarizes previously published data combined from several previous publications from our lab. All data sets include recordings from LGN slices of p27-34 C57/BL6(J)-background WT animals prepared with different cutting solutions. The “Choline” cutting solution was used in Hooks & Chen, 2006, Figs 4-6 and Noutel et al., 2011, Figure 2; 25% sodium replacement: (mM) NaCl 78.3, NaHCO₃ 23, glucose 23, choline chloride 33.8, KCl 2.3, NaH₂PO₃ 1.1, MgCl₂ 6.4, CaCl 0.45. The “Enhanced Choline” solution, which replaced 73% sodium concentration with choline, and added 3.1mM sodium pyruvate and 11.6mM sodium ascorbate, was used in Figure S5 of Thompson et al, 2016: 73% sodium replacement: choline chloride 110, sodium pyruvate 3.1, sodium ascorbate 11.6, NaHCO₃ 25, glucose 25, MgCl₂ 7, KCl 2.5, NaH₂PO₄ 1.25, CaCl₂ 0.5. The “K-Gluconate” solution, which replaced 100% of sodium with potassium gluconate, was used in Hong et al, 2014, which is Chapter 3: 100% Sodium replacement: 130, KCl 15, EGTA 0.05, HEPES 20, glucose 25 pH 7.4. Table 4.5 shows the statistics for these three data sets.

Evaluating Percent of RGCs expressing ChR2 in Chx10;ChR2 retinæ (Chapter 4)

The estimates of the number of afferent inputs using ChR2 stimulation depend on the number of RGC expressing the opsin. Just as with all Cre technologies, Cre-driven expression was not absolute in *Chx10;ChR2* retina. Because the majority of retinal cell types express YFP in *Chx10;ChR2* retina and produce a very bright signal, it was not possible to directly quantify the percent of RGCs do express YFP express. Instead, we took a functional approach to

quantifying the expression of ChR2 in the population of RGC axons that can be stimulated in the OT. To estimate the proportion of RGC axons that can be stimulated with ChR2, we quantified the fraction of the eEPSC that can be occluded with an oEPSC prepulse stimulus. This experiment is conceptually similar to the approach we took to assess whether optical and electrical stimulation activate the same or different single fibers (Figure 4.5B). Figure 4.4H shows an example maximal occlusion experiment and simple algebraic assumptions used to infer this fraction. If all axons in the OT express ChR2, then the amplitude of the depressed maximal eEPSC following an oEPSC stimulus should be similar to the amplitude of the depressed maximal eEPSC following an eEPSC stimulus—both would activate all of the axons accessible to electrical stimulation in the OT. On the other hand, if a subset of axons in the OT don't express ChR2, and therefore can only be stimulated with an electrical stimulus, then the eEPSC following an oEPSC should be larger than the eEPSC following another eEPSC. The difference between the two second-pulse eEPSCs should correspond to the RGC axons that don't express ChR2. Using data from 24 cells among 10 slices and values from eEPSC:eEPSC, oEPSC:oEPSC, and oEPSC:eEPSC trials, we calculated that $86 \pm 2.7\%$ (mean; SEM) of all stimulated axons expressed ChR2 in the OT. Similar values were obtained by replacing the oEPSC:eEPSC trials with the eEPSC:oEPSC trials, as shown in Figure 4.4H, and by examining the distribution of the maximal fEPSC/eEPSC ratio from experiments in Figure 4.3G. This observation should be kept in mind when comparing the amplitudes of electrically and optically stimulated currents in our experiments, and suggests that the oEPSC includes more, yet not necessarily all, RGC inputs to a TC neuron. The resulting estimate of convergence, therefore, is slightly conservative.

Simulation of Retinogeniculate Convergence (Chapter 4)

To calculate the number of functionally relevant inputs that a TC neuron can receive on average at different ages, we carried out a simulation by randomly resampling from sets of

maximal and single fiber EPSC amplitudes. AMPAR current data was used for p30 simulations, whereas NMDAR current data was used for P9-10 simulation

Single fiber values used for simulation

The set of 271 single fibers (Figure 4.7B) was compiled using data from ~p30 cells, with single fiber from data published in Hong et al, 2016/Chapter 3 and unpublished data. For the P9 simulation, a data set consisting of n=35 single fibers recorded from P9-10 C57 animals using electrical stimulation were used. NMDAR single fiber amplitudes corresponding to both AMPAR-containing and AMPAR-silent single fibers was used. The proportion of silent single fiber inputs in these recordings was similar to that previously reported in Chen & Regehr, 2000.

Maximal values used for simulation

All available oEPSC values from ~p30 *Chx10;ChR2* slices were used for this data set, n=68 in all, 1 maximal value from each cell across n=23 animals. For the P9 simulation, n=48 NMDAR eEPSC maximals were used, 1 per cell from n=9 animals. The control experiments shown in Figure 4.4 indicate that any contribution from ChR2 channel-mediated enhancement of the amplitude of oEPSC maximals is likely to be very small.

The simulation

A single trial of the simulation consisted of (1) random drawing of a maximal value, (2) randomly choosing single fibers one by one to match the chosen maximal. Two constraints were placed on this process. (1) If the first randomly chosen single fiber was larger than the randomly chosen maximal, this single fiber was discarded and another was chosen (this was a rare occurrence). (2) Single fibers were randomly drawn from the source distribution until the summed amplitudes of n inputs exceeded 1.05x of the chosen maximal amplitude. The sum of n single fibers and the sum of (n-(last chosen single fiber)) were then compared to the chosen

maximal, and the set of single fibers that yielded a closer value to the chosen maximal was used to tabulate the number and amplitude distribution of single fibers for that simulated cell. The final set of single fibers was then binned into 100-pA bins (Figure 4.7E).

This single trial was repeated 50,000 times for both the p30 and P9 data sets. The resulting distribution of the number of single fibers per maximal are summarized in Figure 4.7. P9 and p30 distributions were compared using a single Mann-Whitney test on 250 randomly chosen values from each 50,000 distribution (4F). About 20-25% of identified P9 inputs are likely to be silent (Chen & Regehr, 2000). Binned single fibers were used to determine the contribution of different single fiber amplitudes to the overall convergence. The ratio of the sum of the selected single fibers and the magnitude of the chosen maximal ($(\sum(\text{single fibers}))/\text{chosen maximal}$) was 0.994 ± 0.17 (mean, SD) for p30 data set and 1.032 ± 0.032 (mean, SD) for the P9 data set.

Assumptions Inherent in the Simulation of Convergence

The simulation, like the fiber fraction and step counting, relies on several important assumptions. First, it assumes that the single fiber isolation method randomly samples single fibers, reflecting the statistics of the population. Second, this simulation ignores potential differences between TC neuron subtypes (see review for refs), which we do not attempt to classify. However, as we often isolate both a strong and a weak single fiber input in most recordings, it is unlikely that we are conflating separate populations that exhibit a low vs. high degree of convergence. Third, our slice recordings may bias the population we can analyze. Differences in TC neuron morphology, which could correspond to differences in convergence (Weyand, 2016), may differentially affect cell health and therefore stability of recordings. The requirement of an intact OT also limits the region of the LGN where single fibers can be reliably isolated, potentially biasing our sample to a retinogeniculate pathway that exhibits greater

convergence. Notably, our recordings are performed in a monocularly-innervated region of the dLGN (Hong 2011, Howarth 2014).

Reconstruction of the location of recorded TC neurons

The locations of patched TC neurons were recorded using a reference grip map, with Y-coordinates numbered 1-4 and x-coordinates: A-E. Locations were noted as an intersection of these coordinates (i.e. “3-4, D-E” corresponds to center of a box defined by the grid near the caudoventral edge of the dLGN). A python script was used to plot the location of each point by adding noise to the x and y coordinates so that every point was plotted closest to its recorded grid coordinates, with noise scaled to the number of points recorded at each coordinate. Using these individualized coordinates maps, were generated in JMP software.

Viral Injections

To enable dual channel experiments (Figure 5.7), we performed eye injections into the left eye of three CART-IRES2-Cre heterozygous mice. After isoflurane anesthesia put the mouse to sleep, the eye ball was exposed, and a sterile 30G needle tip was used to make a small hole in the side of the eye above the region where the retina lines the eye cup. A blunt 30G Hamilton Syringe was then inserted into the hole, 1-1.5 μ l of virus was injected, and the needle remained in place for 10-20 seconds to prevent the contents of the injection from leaking out. The area was then treated with topical lidocaine and subsequently meloxicam for analgesia was administered. AAV2/2 were made by the Viral Core at Boston Children’s hospital from plasmids provided by Minsuk Hyun and Bernardo Sabatini. For these injections, we combined a 1:1 mixture of “Cre-off-ChR2” rAAV2/CBA-FAS-ChR2(H134)-MCherry (Saunders et al., 2012) $>10^{12}$ molecules/mL and “Cre-on-ReachR” rAAV2/hSyn-Flex-ReachR-mCitrine (Lin et al., 2013; addgene 50955) $>10^{13}$ molecules/mL. Three mice used for these experiments had healthy retinae and lenses at the time of sacrifice.

CHAPTER 3

Refinement of the Retinogeniculate Synapse by Bouton Clustering

Attributions: This chapter is a published manuscript: Hong YK, Park S, Litvina EY, Morales J, Sanes JR, Chen C. Refinement of the retinogeniculate synapse by bouton clustering. *Neuron*. 2014 Oct 22;84(2):332-9, reprinted with permission. The primary contribution of EYL was for electrophysiology and dense RGC labeling aspects of this study. YKH, JRS, CC were responsible for the conception and design of research; YKH, SP, EYL performed experiments; YKH, SP, EYL, CC analyzed data; YKH, EYL, JRS, CC interpreted results of experiments; YKH, EYL prepared figures; YKH, EYL drafted manuscript; JRS, CC edited and revised manuscript; JRS, CC approved final version of manuscript. Supplementary figures may be found in the appendix, and supplementary methods have been incorporated into Chapter 2: Materials and Methods.

Refinement of the Retinogeniculate Synapse by Bouton Clustering

Y. Kate Hong^{1,2,3}, SuHong Park¹, Elizabeth Y. Litvina¹, Jose Morales¹, Joshua R. Sanes² and

Chinfei Chen^{1*}

¹F.M. Kirby Neurobiology Center

Department of Neurology

Boston Children's Hospital

Harvard Medical School

300 Longwood Avenue

Boston, MA 02115

²Department of Molecular and Cellular Biology

Center for Brain Science, Harvard University

52 Oxford Street

Cambridge, MA 02138

³Present address: Department of Neuroscience

Columbia University, New York, NY 10032

To whom correspondence should be addressed:

F.M. Kirby Neurobiology Center

Boston Children's Hospital

300 Longwood Avenue, CLS 12250

Boston, MA 02115

Phone: 617-919-2685, Fax: 617-919-2772

chinfei.chen@childrens.harvard.edu

ABSTRACT

Mammalian sensory circuits become refined over development in an activity-dependent manner. Retinal ganglion cell (RGC) axons from each eye first map to their target in the geniculate and then segregate into eye-specific layers by the removal and addition of axon branches. Once segregation is complete, robust functional remodeling continues as the number of afferent inputs to each geniculate neuron decreases from many to a few. It is widely assumed that large-scale axon retraction underlies this later phase of circuit refinement. On the contrary, RGC axons remain stable during functional pruning. Instead, presynaptic boutons grow in size and cluster during this process. Moreover, they exhibit dynamic spatial reorganization in response to sensory experience. Surprisingly, axon complexity decreases only after the completion of the thalamic critical period. Therefore, dynamic bouton redistribution along a broad axon backbone represents an unappreciated form of plasticity underlying developmental wiring and rewiring in the central nervous system.

INTRODUCTION

In many mammalian neural circuits, connections are refined over development with synapse elimination and strengthening. The canonical view of refinement involves large-scale retraction of axons. This view is derived in large part from studies of peripheral motor and autonomic axons (Keller-Peck et al., 2001; Purves and Lichtman, 1980; Tapia et al., 2012). In only in a few cases have axonal dynamics been analyzed during circuit refinement in the central nervous system (Cheng et al., 2010; Hashimoto et al., 2009; McLaughlin et al., 2003; Sugihara, 2005). It therefore remains unclear whether the model of axon retraction applies generally to central projections.

Here, we use the retinogeniculate synapse to address this issue. Initially, retinal ganglion cell (RGC) axons from each eye form imprecise maps in the dorsal lateral geniculate nucleus (LGN), with individual axons innervating neurons across eye-specific layers with a broad retinotopic expanse. By adulthood, these maps are retinotopically precise with axons targeted to specific monocular layers and low afferent convergence onto geniculate neurons. This transformation occurs in at least three phases (Figure 3.1A). First, axonal arbors become topographically refined and segregate into eye-specific layers (Dhande et al., 2011; Sretavan and Shatz, 1984). In mice, this phase occurs by ~P10 (Hong and Chen, 2011; Huberman et al., 2008), prior to eye-opening at ~P12. Second, continuing until ~P20, functional studies show that the number of axons that innervate each LGN neuron decreases several-fold (synapse elimination) and the connections that persist become stronger (synaptic strengthening) (Chen and Regehr, 2000; Jaubert-Miazza et al., 2005). This phase, like the first, depends on spontaneous activity but not vision. Third, refinement continues and becomes dependent on visual experience between P20 and P30. Visual deprivation during this phase reduces synaptic strength and increases the number of afferent RGC inputs onto relay neurons (Hooks and Chen, 2006, 2008).

Classical studies have analyzed structural correlates of the first phase of refinement in several mammalian species. Axons segregate into eye-specific layers by the removal of sprouts from “incorrect” layers and elaboration of new branches and synapses in “correct” layers (Sretavan and Shatz, 1984). Little is known, however, about structural alterations that underlie later phases. Here, to elucidate the structural basis for changes in functional connectivity during development, we used transgenic mice in which a functionally defined subset of RGCs (BD-RGC) can be sparsely labeled (Kim et al., 2010), and reconstructed individual RGC arbors over development and in response to sensory deprivation. We find that rather than axon retraction, changes in presynaptic bouton size and distribution underlie late synaptic refinement and experience-dependent plasticity at the retinogeniculate synapse. Structural pruning does occur, however, during a fourth, previously unrecognized phase of refinement that follows the period for vision-directed plasticity. Together, our results suggest that bouton rearrangement, rather than arbor pruning, underlies functional refinement, and that axon retraction serves to limit synaptic plasticity in the adult.

RESULTS

To visualize RGC axon arbors, we used transgenic mice that express a tamoxifen-activated Cre recombinase (CreER) in BD-RGCs, which are bistratified, ON-OFF direction selective cells that respond to downward motion (Kim et al., 2010). When these mice are crossed to mice in which expression of YFP is Cre-dependent (Buffelli et al., 2003), BD-RGCs are indelibly marked following administration of tamoxifen. The use of ligand-activated Cre allowed us to control the number of cells labeled in the retina by titrating the dose of tamoxifen administered, and thus visualize single-cell morphology (Figure 3.1B-E). BD-RGC axon arbors target the area where we and others have previously characterized retinogeniculate synaptic refinement by slice electrophysiology (Chen and Regehr, 2000; Jaubert-Miazza et al., 2005;

Koch and Ullian, 2010; Stevens et al., 2007). By focusing on one RGC subtype, structural heterogeneity arising from the existence of multiple RGC subtypes can be minimized. Our analysis was restricted to arbors that projected to the dorsal lateral portion of the LGN (Supplementary Figure 7.1A-B), which spans both the shell and core regions of the LGN (Cruz-Martín et al., 2014; Krahe et al., 2011).

Spontaneous Activity-Dependent Phase of Structural Refinement

We first analyzed axons between P8 and P20, which spans the last days of eye-specific segregation, eye opening (P12-14), and experience-independent synapse elimination (Hong and Chen, 2011; Huberman, 2007). The number of afferent inputs per relay neuron decreases from >10 to half during this period, and the remaining inputs strengthen ~20-fold (Chen and Regehr, 2000; Hooks and Chen, 2006).

Surprisingly, average arbor size and complexity did not decrease during this period. Instead, the axon total length and complexity increased significantly between P8 and P12 (Figure 3.1F, H, I), consistent with previous observations (Dhande et al., 2011; Snider et al., 1999; Sretavan and Shatz, 1984). While this period of axon expansion corresponds to growth of the LGN (Supplementary Figure 7.1C), the estimated number of LGN neurons encompassed by a single BD-RGC axon arbor volume did not change significantly (Supplementary Figure 7.1D-F). Arbor growth between P8 and P12 was also concurrent with an increase in the number of branch points (Figure 3.1I), suggesting elaboration of the arbor and increase in potential contacts between pre- and post-synaptic partners. Between P12 and P20, a period of active functional synapse elimination, there was little change in the total or average segment length, number of segments, branch points, terminals or branch order of arbors (Figure 3.1F-K). Together, these results reveal dissociation between functional synaptic elimination and structural pruning.

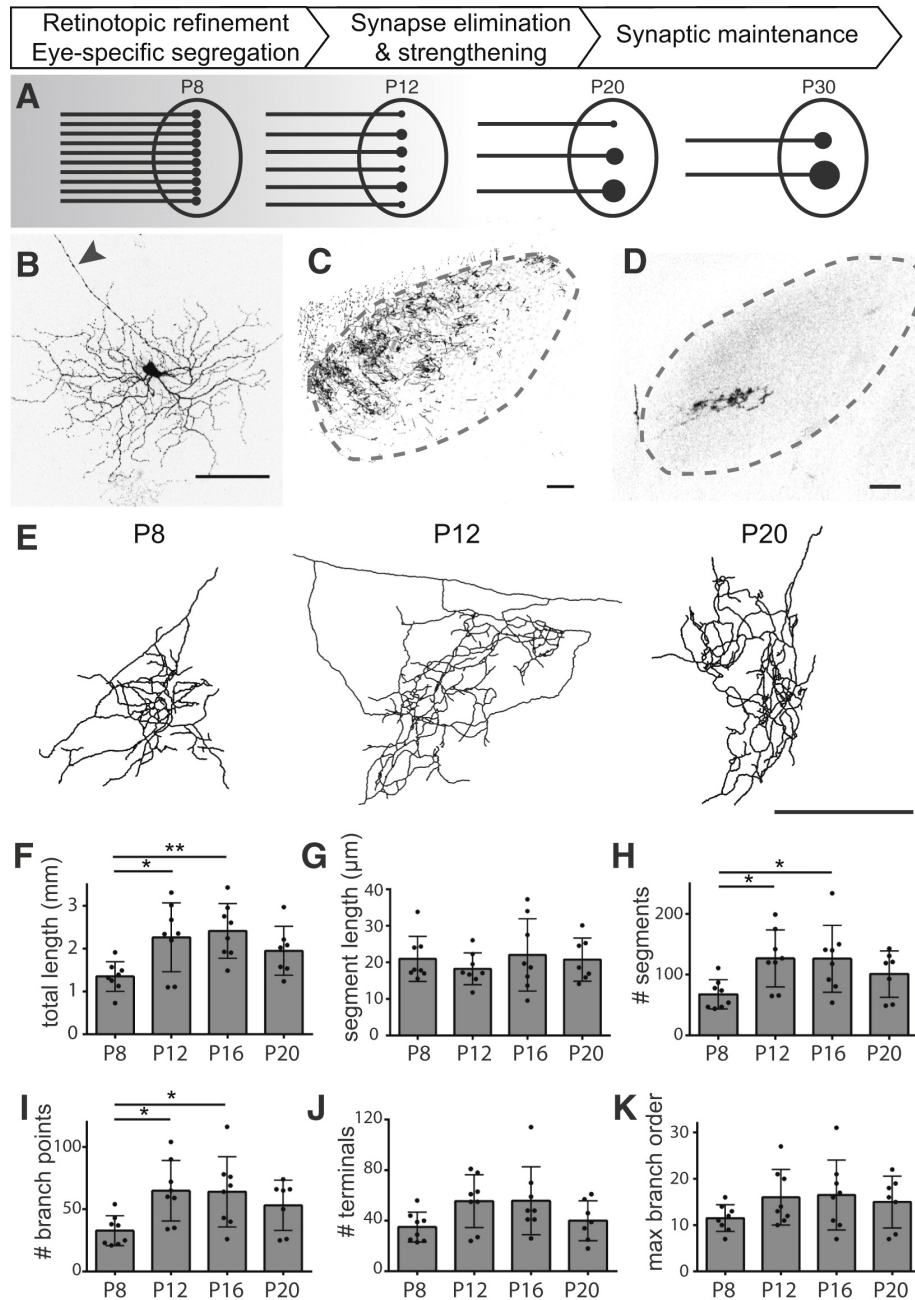


Figure 3.1: Development of BD-RGC axon terminals in the LGN.

(A) Schematic of functional pruning at the retinogeniculate synapse. LGN neurons (large ovals) and RGC inputs (black lines) of varying strength (black circles). Adapted from Hong and Chen, 2011. (B) Confocal images of BD-RGC labeled in the retina of BD-YFP double transgenic mice. Arrowhead: primary axon. (C) Dense labeling of BD-RGC axons in the dorso-lateral region of LGN (sagittal view). (D) Single axon labeled by low-dose of tamoxifen. Dashed lines indicate LGN boundary. (E) Examples of reconstructed BD-RGC axon arbors. Quantification of (F) total axon length, (G) average segment length, number of (H) segments, (I) branch points, (J) terminal endings, and (K) maximum branch order. B-D: Image gray values inverted for clarity. Scale bars: 100 μm. Error bars: SEM. See also Figure S1.

Spatial redistribution of presynaptic boutons occurs with development

Detailed examination of the reconstructed arbors provided insight into the structural basis of developmental refinement. The most striking changes between P8 and P20 were in the size and location of bouton-like varicosities along the axon terminal (Figure 3.2A-C). We defined boutons as regions of the arbor where the width of axons was greater than twice the diameter of the flanking axon (Materials and Methods). The average bouton diameter increased significantly between P8 and P20 ($P < 0.001$, Kruskal-Wallis one way ANOVA and Dunn's post hoc test; Figure 3.2L, Supplementary Figure 7.2A-C). Previous ultrastructural studies have indicated that in the adult LGN, the number of release sites is correlated to the volume of boutons (Hamos et al., 1987). Thus, an increase in bouton size may correspond to the addition of synapses within each bouton as connections are strengthened over development.

In order to determine whether structural boutons contained presynaptic elements, we quantified the degree of colocalization of boutons with vesicular glutamate transporter 2 (VGLUT2), a presynaptic marker for RGC, but not cortical, inputs in the LGN (Land et al., 2004) (Figure 3.2D-I). Colocalization was high at both immature and mature axons and did not significantly differ with age ($88.2 \pm 4.1\%$ at P8 vs. $92.5 \pm 6.5\%$ at P20-30, mean \pm SD, $p = 0.09$, student's t-test, $n = 10$, statistical power = 0.8, Materials and Methods, Figure 3.2G). We also quantified the fraction of VGLUT2 positive puncta within BD axons that did not co-localize to boutons. This may reflect less mature synapses, or trafficking of synaptic elements along the axon early in development. Consistent with this notion, VGLUT2 puncta outside of boutons was significantly higher in young than old axons ($18.5 \pm 8.0\%$ vs. $10.9 \pm 5.1\%$, mean \pm SD, $n = 10$, $p = 0.02$, Supplementary Figure 7.2G). Thus, over development, varicosities are reliable markers for presynaptic boutons representing more mature synapses.

In addition to size, the spatial distribution of boutons changed dramatically as the synapse matured. At P8, boutons were relatively evenly dispersed throughout the axon arbor. In contrast, by P20, boutons were densely clustered in restricted regions of the axon, leaving large

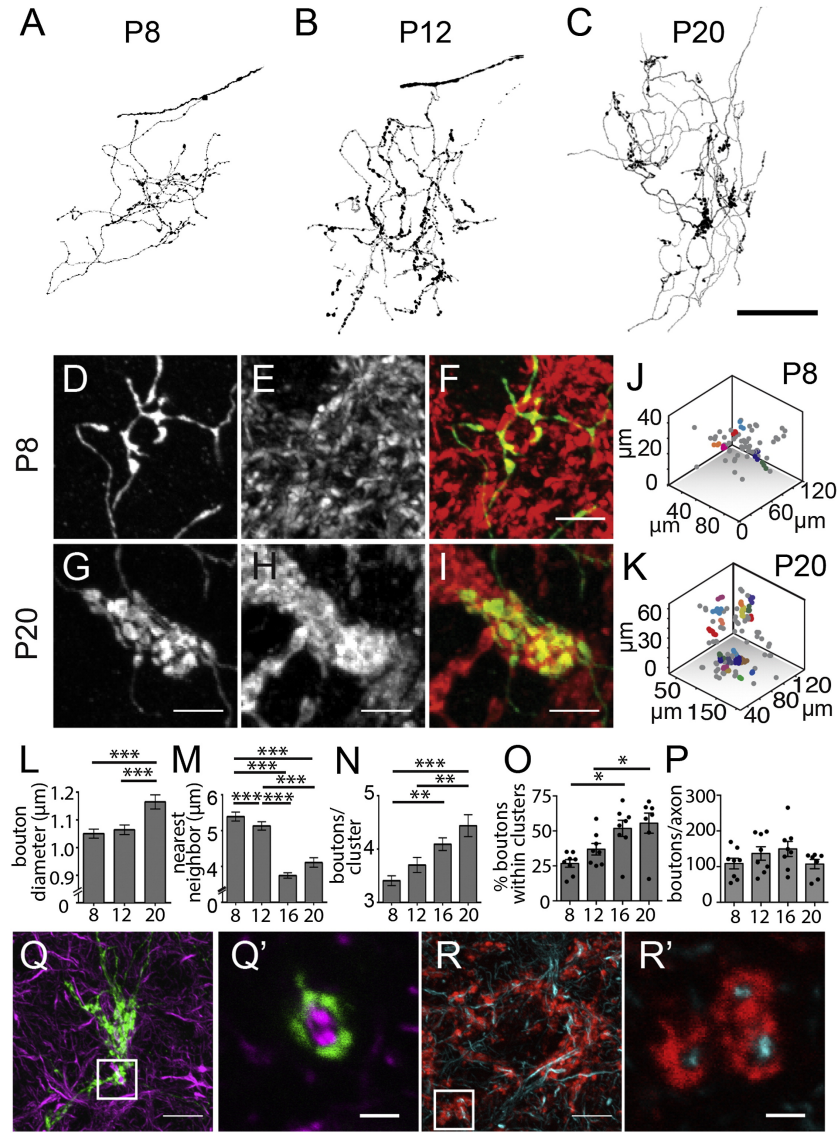


Figure 3.2: Boutons cluster over development.

(A-C) Confocal images of single YFP-labeled BD-RGC axons at different ages. LGN from P8 and P20 BD-YFP mice coimmunolabeled against YFP (D,G), VGLUT2 (E,H) and merged images (F, I; VGLUT2, red; YFP, green). (J, K) Example outcomes of mean-shift clustering analysis for boutons in x, y, z space for axons shown in A and C. Colored dots represent boutons within clusters; grey dots lie outside clusters. (L-P) Quantification of bouton diameter, NN distances, cluster size (boutons/cluster, >2 boutons) determined by mean-shift clustering analysis, % boutons within clusters, and # boutons per axon. Maximum projection images of confocal stacks of P22 LGN labeling BD-RGC (green) SMI-32 (magenta) (Q,Q'); VGLUT2 (red) and SMI-32 (cyan) (R, R'). Q',R': magnified images of single optical section of inset shown in (Q, R), respectively. Scale bars: A-C: 50 μ m, D-I: 5 μ m, Q, R: 10 μ m, Q',R': 2 μ m. Error bars: SEM. See also Figure S2, S3.

stretches of the axon arbor without boutons (Figure 3.2A-C, Supplementary 7.3G,H). We determined the 3-D x,y, and z positions of each bouton along the arbor of singly labeled axons (Figure 3.2 J,K), and quantified clustering in two ways: nearest neighbor distance and mean-shift clustering (see Materials and Methods). The average nearest neighbor (NN) distance decreased significantly from $\sim 5.5 \mu\text{m}$ at P8 to $\sim 4 \mu\text{m}$ at P20, by which point clusters of boutons are visibly discernible (Figure 3.2A-C, M). Likewise, cluster size and the percent of boutons within clusters gradually increased between P8 and P20 (Figure 3.2N,O). Despite the spatial redistribution of boutons with maturation, the average number of boutons/arbor remained unchanged over development (Figure 3.2P). Taken together, our results suggest that an immature RGC makes weak synaptic contacts broadly onto many LGN neurons within the territory covered by its arbor, and functional retinogeniculate refinement occurs by spatially redistributing a limited number of boutons over a broad axon scaffold such that they are concentrated onto a few postsynaptic neurons.

Coimmunolabeling revealed that YFP-positive bouton clusters were frequently nested within a larger cluster of VGLUT2 islands (Figure 3.2G-I, Supplementary 7.2D-F). This suggests that single axon arbor clusters were part of larger groups of boutons contributed by other, unlabeled RGC axons. As VGLUT2 is expressed in most RGC terminals (Land et al., 2004), of which a minority are BD-RGCs ($\sim 4\%$ of RGCs in the retina; Kay et al., 2011), bouton clustering is likely a general mechanism used by other RGC types. The bouton clusters were frequently found to form rosette- or donut-like structures (Supplementary Figure 7.2D-F,H,I) in which the “holes” contained processes labeled by antibodies against unphosphorylated neurofilament (SMI-32), a marker of somata and proximal dendrites of LGN neurons, (Figure 3.2Q-R', Jaubert-Miazza et al., 2005). Thus, clustering is likely to reflect numerous synapses from one or a few cells onto proximal dendrites of relay neurons (Hamos et al., 1987). RGC inputs that contribute to the same cluster may be functionally similar, as suggested by studies in other regions of the CNS (Winnubst and Lohmann, 2012).

Experience-Dependent Anatomical Refinement

The vision-independent developmental period is followed by a later phase of experience-dependent plasticity spanning P20-P31. Under normal light rearing (LR) conditions (12 hr light/dark cycle), visual experience stabilizes and maintains the refined circuitry, and electrophysiological studies show no substantial changes in strength or connectivity between P20 and P31. However, extreme changes in visual experience, such as dark rearing during this period (from P20 for > 7 days, referred to as late dark-rearing, LDR), leads to weakening of synaptic strength to 50% of LR mice, and a doubling of afferent inputs onto each relay neuron (Hooks and Chen, 2006).

To assess structural changes that underlie functional plasticity during LDR, we compared RGC arbors reconstructed from LR and LDR mice (Figure 3.3A,B). Consistent with functional studies, average axon arbor length, complexity, number of boutons/cluster and boutons/axon did not change significantly under normal LR conditions between P20 and P31 (Figure 3.3C-H, black lines, and Supplementary Figure 7.4). Analysis also revealed no significant difference in the size or complexity of axons from LR and LDR mice at P31 (Figure 3.3C-E). However, there was a reduction in the degree of bouton clustering and size in deprived mice. While the average number of boutons did not differ (Figure 3.3F), the NN distance between boutons was greater (Figure 3.3G) and there were fewer boutons per cluster in LDR when compared to LR arbors (Figure 3.3H). Consistent with a decrease in synaptic strength after LDR, the bouton diameter of P31 LDR axons was significantly smaller than those of LR mice (Figure 3.3I). Therefore, small-scale changes in the position and distribution of boutons accompany the rewiring between RGC and relay neurons in response to sensory experience, supporting the idea that bouton size and clustering correspond with the functional connectivity and strength of the retinogeniculate synapse.

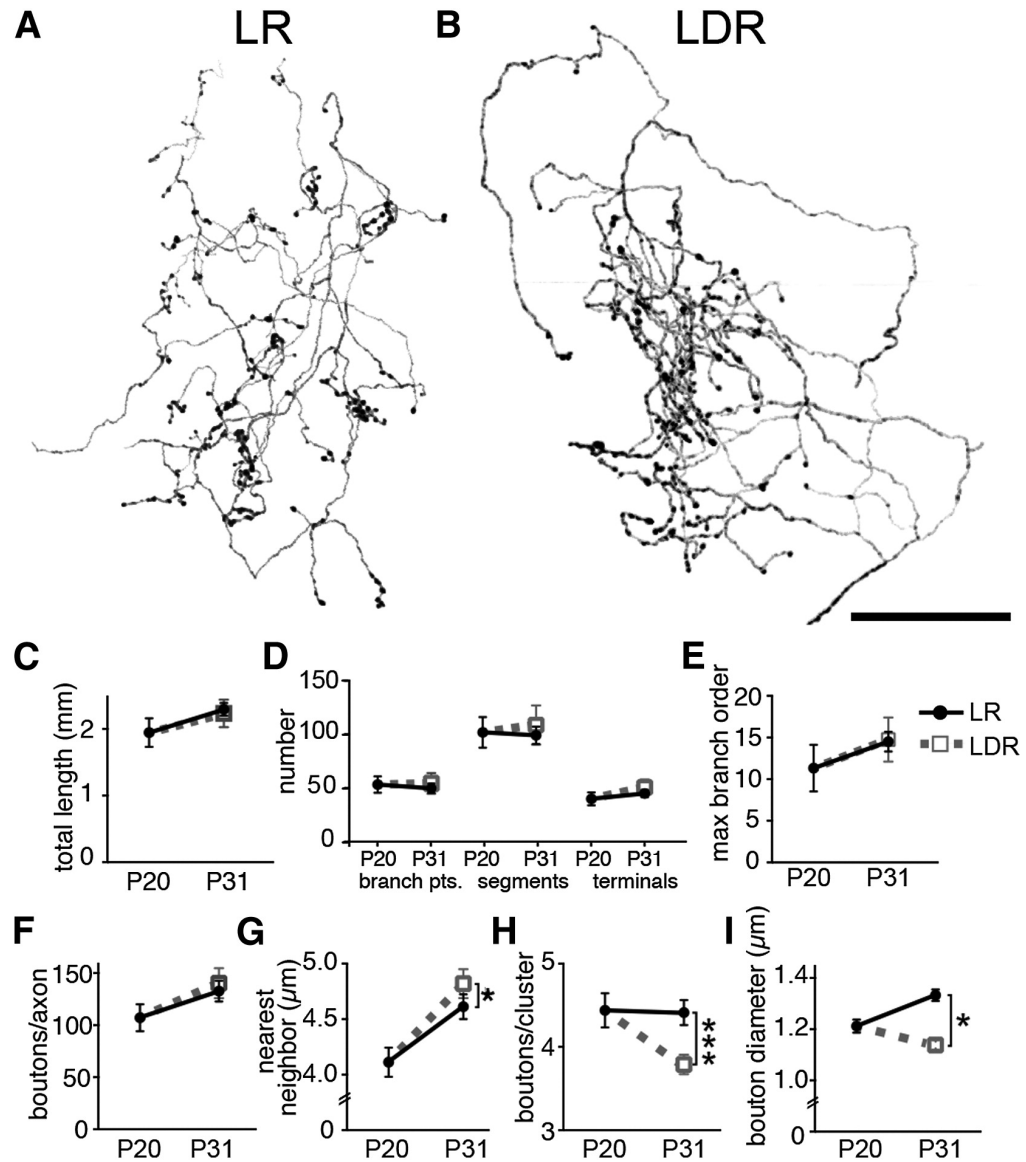


Figure 3.3: Sensory-dependent Axonal Remodeling.

Maximum Projection images of (A) LR and (B) LDR BD-RGC axons. Quantification of average axon (C-E) and bouton (F-I) parameters between P20 and P31 in LR (black) and LDR (grey) mice. P20 data set is the same as in Figure 1-2, shown for comparison. Scale bars: $50\mu\text{m}$. Error bars: SEM.

Axon Refinement following Sensory-Dependent Plasticity

Finally, we extended our analysis to one month beyond the sensory-dependent phase of synapse remodeling (P31-60). Remarkably, significant axon pruning occurred during this interval: total axon length, complexity and the number of boutons/axon decreased (Figure 3.4A-E), while the average diameter of the remaining boutons continued to increase (Figure 3.4F). In contrast to the structural refinement of the axon backbone, NN distance decreased slightly but there was little change in boutons/cluster (Figure 3.4G,H) or the number of clusters per axon (14.75 ± 5.4 vs. 9.27 ± 6.0 , mean \pm SD for P31 and P60 respectively; $p > 0.05$ Mann-Whitney). Thus, overall structural pruning occurred only after the phase of experience-dependent synapse refinement.

To test whether the reduction in arbor complexity with age corresponded to a previously undetected change in functional connectivity, we recorded from mature mice (\geq P60, Figure 3.4I). We found that the average single fiber strength in P60 mice were statistically indistinguishable from P31 mice (Figure 3.4J). However, the fiber fraction, an estimate of the number of inputs innervating a relay neuron, significantly increased largely due to a reduction in the maximal currents (P31 vs. P60, in nA: Max AMPAR 4.1 ± 0.2 vs. 3.02 ± 0.2 ; Max NMDAR 3.3 ± 0.3 vs. 1.93 ± 0.2 mean \pm SEM, both $p < 0.001$) (Figure 3.4K). The additional functional pruning at the retinogeniculate synapse between P31 and P60 is consistent with our findings of a decrease in the total number of boutons. These findings suggest that once the appropriate connections between RGCs and relay neurons have stabilized, excess axon segments and boutons are removed.

DISCUSSION

Studies of randomly labeled RGCs in cat and mice have demonstrated that after eye-specific segregation is complete, axon arbors continue to grow and elaborate in the correct LGN layer

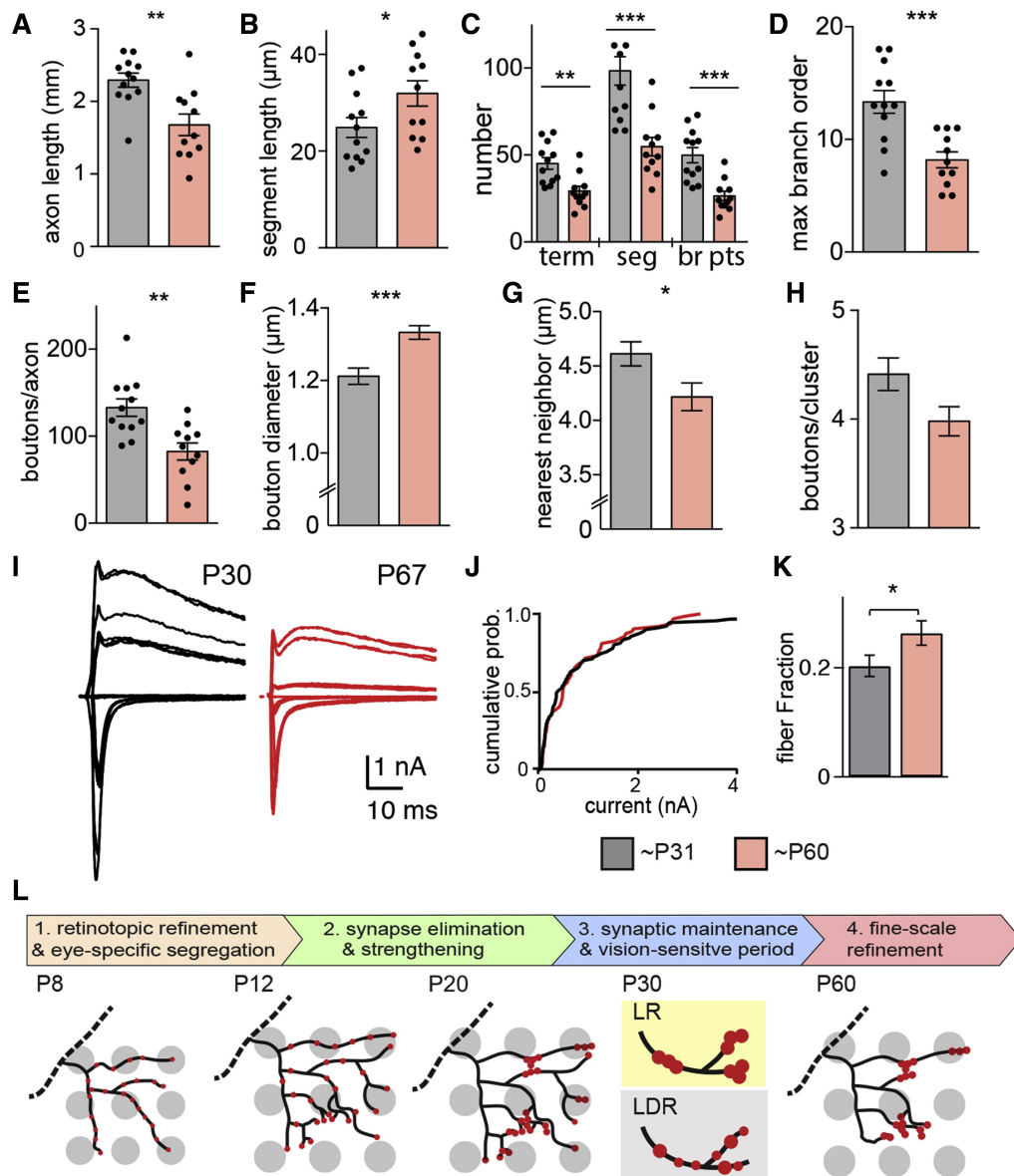


Figure 3.4: Structural axonal pruning occurs between P31-60.

Axon backbone (A-D) and bouton (E-H) parameters at P31 (grey) and P60 (red). P31 data set is the same as Figure 3. (I) Representative retinogeniculate slice recordings at P30 and P67. (J) Cumulative probability distribution of single fiber AMPAR strength shows no significant difference. (K) The fiber fraction increases with age. J-K, grey includes P27-34, and red, P60-75. (L) Summary schematic of structural plasticity of RGC axons in LGN. (1) During retinotopic refinement and eye-specific segregation, the axon arbor elaborates and becomes more complex in the monocular layer. (2) During the period of functional synapse elimination and strengthening, the overall structure of the BD-RGC axon backbone is maintained, but the synaptic boutons are redistributed to form clusters and grow in size. (3) During the vision-sensitive period, LDR results in declustering of boutons and decrease in bouton size when compared to LR mice. (4) Finally, between P30-P60, further axonal and synaptic pruning takes place, with a reduction in axon size and complexity. Error bars: SEM. See also Supp. Figure 7.4.

(Dhande et al., 2011; Snider et al., 1999; Sretavan and Shatz, 1984; Sur et al., 1984). Over development, these arbors remain large despite known physiologic convergence of RGC afferents onto relay neurons (Cleland et al., 1971; Hamos et al., 1987; Mastronarde, 1992). Here we describe a previously unappreciated presynaptic mechanism of circuit refinement that explains the dissociation between structure and function. Instead of axon pruning, rewiring of a network occurs by small-scale changes in bouton position and size (summarized in Figure 4L). Rather than thinking of the immature axon structure as an imprecise attempt to make proper connections, we suggest that the axon arbor is best viewed as an opportunity map of appropriate pre-and post-synaptic connections.

Bouton Clustering

Between P8-P20 the boutons form clusters, focusing on a small subset of the many postsynaptic neurons with which the arbor could, in principle, contact. This period corresponds to a developmental window when the number of inputs to the LGN neuron decreases by ~50% (Chen and Regehr, 2000), suggesting that clustering acts both to increase connections with some partners and to eliminate connections with others. By P20, when boutons have clustered, the axon backbone is larger than functionally necessary. Therefore, developmental 'synapse refinement' does not simply mean the removal of synaptic contacts in the form of axon branches (Purves and Lichtman, 1980). For the postsynaptic relay cell, the total number of synaptic contacts does not change, but the presynaptic cells associated with these contacts have pruned down (Hooks and Chen, 2006).

Bouton clusters have been described in retinal axons as well as other neurons throughout the mammalian CNS (Binzegger et al., 2007; Kleindienst et al., 2011; Mason, 1982; Sur and Sherman, 1982; Takeuchi et al., 2014). Here, by fully reconstructing RGC arbors at different developmental time points, we show that bouton redistribution occurs with age. Consistent with our clustering data, reconstruction of a single RGC axon in adult cat LGN

showed that a section of the arbor made synaptic contacts with only 4 of 40 possible postsynaptic partners, including >200 contacts onto one neuron (Hamos et al., 1987). Thus, bouton clustering onto the same cell, in combination with increased number of synaptic release sites within each growing bouton (Hamos et al., 1987; Yeow and Peterson, 1991), contributes to the 20-fold average strengthening of RGC inputs to LGN neurons.

RGC axon terminal morphologies in the rodent LGN vary in different LGN laminae (Erzurumlu et al., 1988), thus it is likely that distinct forms of pruning occur among RGC subclasses (Sur et al., 1984). While we studied only one of >20 RGC subtypes in detail (BD-RGCs), we observed similar alterations in J-RGCs (Kim et al., 2008) (Figure S3I,J), as well as in the distribution of VGLUT2 alone, which labels synaptic boutons of most RGC subtypes (Figure S3A,D). Thus clustering is likely to occur in non-BD RGC boutons as well. The mechanism of refinement by bouton clustering may be generalizable to other species, as bouton clusters have been well documented for RGCs in several species (Famiglietti and Peters, 1972; Ling et al., 1998). Moreover, broadening of axon arbors has been observed in randomly labeled RGCs throughout the LGN during the early stages of development (Dhande et al., 2011; Snider et al., 1999; Sretavan and Shatz, 1984).

Retinogeniculate axon reorganization is a continuous and dynamic process involving active axon branch addition and removal, in a similar manner as has been shown in other systems (Meyer and Smith, 2006; Portera-Cailliau et al., 2005; Ruthazer et al., 2006). However, our data indicate that there is no *net* decrease in total arbor length and complexity during the period of robust functional refinement. Rather, axon complexity increases during early stages (P8-16) accompanied by significant clustering of presynaptic boutons. Why some synaptic connections refine by extensive die-off of terminal branches while others remodel with bouton clustering is still not clear. One possibility is that some presynaptic neurons, such as motor neurons, exclusively form synapses at the terminal end of axon branches, whereas others form *en passant* synapses that can undergo elimination without changing the axon backbone. With

rewiring during the sensory-dependent developmental period, extension and retraction of the axon arbor could be difficult at ages when the extracellular matrix is dense and complex. Thus, a more straight-forward means of remodeling a circuit may involve the addition of boutons and release sites to a pre-existing large axon scaffold. In this scenario, the axon arbor structure does not accurately reflect functional connectivity.

Experience dependent changes in structure

With the onset of vision-dependent plasticity, the positions of the boutons can be adjusted along the axon arbor based on sensory experience. As in the case of LDR, small changes in bouton clustering can lead to significant rewiring of pre and post-synaptic partners. Previous structural studies of experience-dependent plasticity in several species have focused on changes in the axon structure (Antonini and Stryker, 1993; Hua et al., 2005; Ruthazer et al., 2006). Interestingly, much like the retinogeniculate synapse, the thalamocortical axon backbone does not reflect rapid functional changes that occur in response to monocular deprivation (Antonini et al., 1999). Why functional ocular dominance plasticity precedes the shrinkage of the axon arbor by days has been a subject of ongoing debate. Studies looking for changes in synaptic density along segments of thalamocortical arbors (Silver and Stryker, 1999), or in visual cortex (Coleman et al., 2010) reported conflicting results. However, these studies did not reconstruct whole arbors to determine whether there were changes in the spatial distribution of synapses. Perhaps bouton rearrangement precedes the withdrawal of axon branches (Antonini and Stryker, 1993). Indeed, dynamic remodeling of boutons along a stable backbone has been observed in other areas accessible to time-lapse imaging (Morgan et al., 2011; De Paola et al., 2006; Stettler et al., 2006; Wierenga et al., 2008).

Late Axon Pruning

Once experience-dependent plasticity has closed, the RGC axon scaffold is reduced,

limiting the potential range of pre- and postsynaptic connectivity. During this final phase of refinement, between P31 and P60, single fiber strength is unchanged, but the maximal currents decrease, leading to a more refined circuit. The number of boutons/cluster and the total number of clusters/axon do not change significantly, but the total number of boutons per axon decreases, suggesting that the elimination of boutons outside of clusters lead to the decrease in maximal current. During this phase, the removal of boutons coincides with a reduction in axon complexity. These findings are consistent with time lapse studies in *Xenopus* showing that axon branches containing few synaptic puncta retract, while those with many puncta stabilize (Li et al., 2011; Ruthazer et al., 2006).

CONCLUSION

A broad axon scaffold that persists into adulthood has deep implications in development as well as in diseases involving synaptic connections. As long as the axon scaffold exists, circuit rewiring is possible. An example of the potential of an axon scaffold can be seen in barn owls whose visual field has been shifted using prisms. Young owls are able to realign their visual and auditory fields by permanently extending their axon arbor. These arbors remain broad into adulthood, and functional specificity has been proposed to arise from inhibition of inappropriate synaptic contacts and by bouton clustering (Linkenhoker et al., 2005; Zheng and Knudsen, 2001). The broad arbors allow older barn owls with previous prism experience to adapt to changes in visual maps more easily than naïve birds of the same age, suggesting that the axon backbone represents a structural history of previous connections (Knudsen et al., 2000; McBride et al., 2008). Here we show that at the retinogeniculate synapse, bouton clustering underlies the development of functional specificity. However, the remnants of the RGC axon arbor may allow rapid re-establishment of previously eliminated connections during experience-dependent plasticity. With the final retraction of the axon arbor after sensory-dependent synaptic remodeling, plasticity is substantially reduced.

ACKNOWLEDGEMENTS

This work was supported by NIH R21EY018308, RO1 EY013613 and PO1HD18655 to CC and RO1 NS29169 to JS, and F31 NS055488 to YKH. We thank J. Hauser, A. Thompson, J. Leffler, B.H. Lee, B.M. Hooks, J. Lichtman, T. Hensch, M. Fagiolini and B. Stevens for helpful discussion and comments and R. Bruno for his continued patience and support for the project.

CHAPTER 4

Functional Convergence at the Retinogeniculate Synapse

Attributions: This chapter consists of a manuscript in preparation for submission. All experiments were designed in collaboration with CC and carried out by EYL, with technical help in perfusions and immunohistochemistry from Sally Curtiss. This draft was written by EYL and edited in collaboration with Chinfai Chen. It has benefited from discussion with the entire Chen lab and DAC committee as listed in acknowledgements section. Supplementary figures have been incorporated into the main flow of this version of the text.

Functional Convergence at the Retinogeniculate Synapse

Elizabeth Y Litvina and Chinfai Chen*

Department of Neurology, F.M. Kirby Neurobiology Center, Children's Hospital, Boston, 300

Longwood Avenue, Boston, MA 02115

Program in Neuroscience, Harvard Medical School, 220 Longwood Avenue, Boston, MA 02115

*To whom correspondence should be addressed:

F.M. Kirby Neurobiology Center

Boston Children's Hospital

300 Longwood Avenue, CLS 12250 Boston, MA 02115

Phone: 617-919-2685, Fax: 617-919-2772

chinfai.chen@childrens.harvard.edu

ABSTRACT

The retinogeniculate synapse has classically been described as a simple relay between the retina and the primary visual cortex. Consistent with this view, electrophysiological measurements have previously estimated that 1-3 retinal ganglion cells (RGC) synapse onto a mouse geniculate relay neuron (Chen & Regehr, 2000; Jaubert-Miazza et al., 2015). However, technical limitations have set these estimates as the lower bound of possible retinogeniculate convergence. Recent advances in connectomics and rabies tracing have yielded much larger estimates of the number of connections between RGC axons and postsynaptic thalamocortical (TC) neurons (Morgan et al, 2016; Rompani et al, 2017), but it is not clear what fraction of these contacts may be functionally relevant to retinogeniculate information transfer. To determine the overall number of functionally relevant retinogeniculate inputs that contact TC neurons in mice, we took advantage of optogenetics to measure total retinal synaptic drive onto a TC neuron. We combined these measurements with the distribution of amplitudes of single retino-geniculate contacts to determine that ~10 RGCs on average converge onto a TC neuron in adult mice, in contrast to >70 inputs present before developmental refinement. However, only ~3 mature retinogeniculate inputs exceed the threshold for being reliable drivers of activity. Thus, using a novel quantitative optogenetic approach, we provide an updated estimate of retinogeniculate convergence, showing that mature TC neurons in mice receive a small number of strong and several additional weak inputs from the retina. These results bear important implications for using anatomical data to understand circuit connectivity, and for the role of the dLGN in visual processing.

INTRODUCTION

Divergent and convergent connections in the synaptic circuits of the CNS form the substrate for the complex computations underlying the transmission of information between neurons. In the visual system, information is relayed from the retina to the visual cortex via the retinogeniculate synapse. This synapse is an experimental workhorse for studies in developmental as well as systems neurobiology. Decades of anatomical and functional studies across many adult species have shown that 1-3 retinal ganglion cells (RGCs) innervate a thalamocortical (TC) neuron of the dorsolateral geniculate nucleus (dLGN). This simple wiring diagram suggested a limited role for the dLGN (and indeed the thalamus in general) in sensory processing beyond functioning as a relay (Cleland & Levick, 1971; Hamos et al., 1987; Mastronarde, 1992; Chen & Regehr, 2000; Jaubert-Miazza et al., 2005; Sincich et al., 2009). It also supported the view that the visual system is organized into distinct retino-geniculo-cortical pathways of information that are integrated in higher-order cortical areas (Livingstone & Hubel, 1988; Sherman & Guillery, 2001; Nassi & Callaway, 2009).

Recent anatomical studies in mice using novel large-scale connectomics and retrograde viral tracing approaches have challenged this generally accepted view of retinogeniculate functional organization (Hammer et al., 2015; Morgan et al., 2016; Rompani et al., 2017). They have shown that up to 91 RGCs may converge onto single TC neurons. These observations undermine the idea of parallel subcortical visual streams, and posit significant integration or processing of visual information in the thalamus. However, these studies focused on age ranges that overlap with the thalamic critical period, a late developmental window when connectivity between retina and TC neurons is still plastic (Hooks et al, Thompson et al). Therefore, the possibility exists that many of the morphologically identified inputs are remnants of the refinement process (Hong et al., 2014; Chen et al., 2016). Anatomical approaches also cannot distinguish between functionally strong, weak, and silent contacts. This distinction is important at the retinogeniculate, because single input strength can vary widely, and inputs stronger than

600 pA in amplitude are much more likely to drive TC neuron activity than weak inputs (Liu & Chen, 2008). Therefore, to understand the nature and degree of information coding that occurs in the dLGN, we sought to enumerate the fraction of presynaptic RGCs that are strong enough to have functional relevance for the activity of mature TC neurons.

To determine the overall number and strength of functionally relevant converging retinogeniculate inputs, we here turn to optogenetics in mouse dLGN slices, which allow us to stimulate previously inaccessible retinal inputs. We found that optogenetic stimulation recruits nearly twice as many retinal axons as electrical stimulation of the optic tract (OT). Moreover, single fiber optogenetic stimulation activates RGC inputs with strengths that range several orders of magnitude. Finally, we use these data to simulate retinogeniculate convergence across the sampled TC neuron population. This simulation shows ~10 functionally detectable RGC inputs per TC neuron. These results support anatomical observations of a high degree of convergence of RGCs onto TC neurons. However, we demonstrate that only ~30% of inputs are likely to be strong drivers of TC neuron spiking.

RESULTS

Optogenetic stimulation recaptures axons cut off in slice

Estimates of retinogeniculate convergence in rodents have relied on brain slice recordings and electrical stimulation of the OT. This approach underestimates the total number of RGC inputs, as many of the axons are severed in the slice preparation. To circumvent this limitation of slices, we expressed channelrhodopsin (ChR2 H134R) in all RGCs transgenically. *Chx10-Cre* mice, which express Cre recombinase as early as embryonic day 9 (E9) in RGCs and other retinal layers (Rowan & Cepko, 2004; Kim et al., 2010) were crossed with *Ai32* mice, which express Cre-dependent ChR2(H134R)-EYFP (Madisen et al, 2012).

Postnatally, *Chx10-Cre;ChR2* mice express YFP in multiple layers of the retina,

including in RGC somas (Figure 4.1A) and RGC axon terminals in the LGN (Figure 4.1C, 4.2). Coimmunostaining with the presynaptic marker VGLUT2 demonstrated substantial overlap with YFP (Figure 4.2A; Fujiyama et al, 2013). While some colliculothalamic inputs express VGLUT2 (Cetin & Callaway, 2014), we found no expression of ChR2 in neurons of the superior colliculus (Figure 4.1B). Therefore, the YFP⁺, VGLUT2 terminals are retinal in origin. To confirm that ChR2 is selectively expressed in RGC terminals in dLGN, we first examined expression of YFP in the visual cortex. While we found sparse neuronal, glial, and vascular labeling in the brains of *Chx10;ChR2* mice, YFP-positive cells amounted to just 0.38% of NeuN⁺ cell bodies in visual cortex layer 6, which sends feedback projections to dLGN (Figure 4.2C). Importantly, YFP expression was absent in the corticothalamic bundle innervating dLGN (Compare Figs 4.1 C'-C''). We also ensured that ChR2-expressing corticothalamic axons did not contribute to YFP labeling in the dLGN by immunostaining for VGLUT1, a marker for corticothalamic inputs (Fujiyama et al., 2003). Figure 4.2 B shows minimal overlap between YFP⁺ and VGLUT1⁺ synaptic puncta, indicating no significant ChR2 expression in corticothalamic feedback projections to dLGN. Finally, the absence coexpression of YFP with NeuN or SMI32, a label of proximal dendrites of TC neurons, confirmed that ChR2 was not expressed in dLGN TC neurons (Figure 4.1D,E). Together, these experiments show that *Chx10-Cre;ChR2* mice selectively expressed ChR2 in RGC inputs in the dLGN.

We took advantage of this selective ChR2 expression to re-examine retinogeniculate convergence. Our lab has favored the fiber fraction method to characterize convergence of the retinogeniculate synapse in slice (Hooks and Chen, 2006). Bulk OT stimulation provides an estimate of overall retinal drive onto the TC neuron (the rough sum of individual input strengths), while minimal stimulation measures the strength of single RGC inputs that make up the bulk. The fiber fraction divides the maximal into the single fiber to provide a rough estimate of the contribution of an average RGC input to the total retinal drive. This measure has proven to be a valuable, unbiased tool for relative comparisons of convergence over different ages and

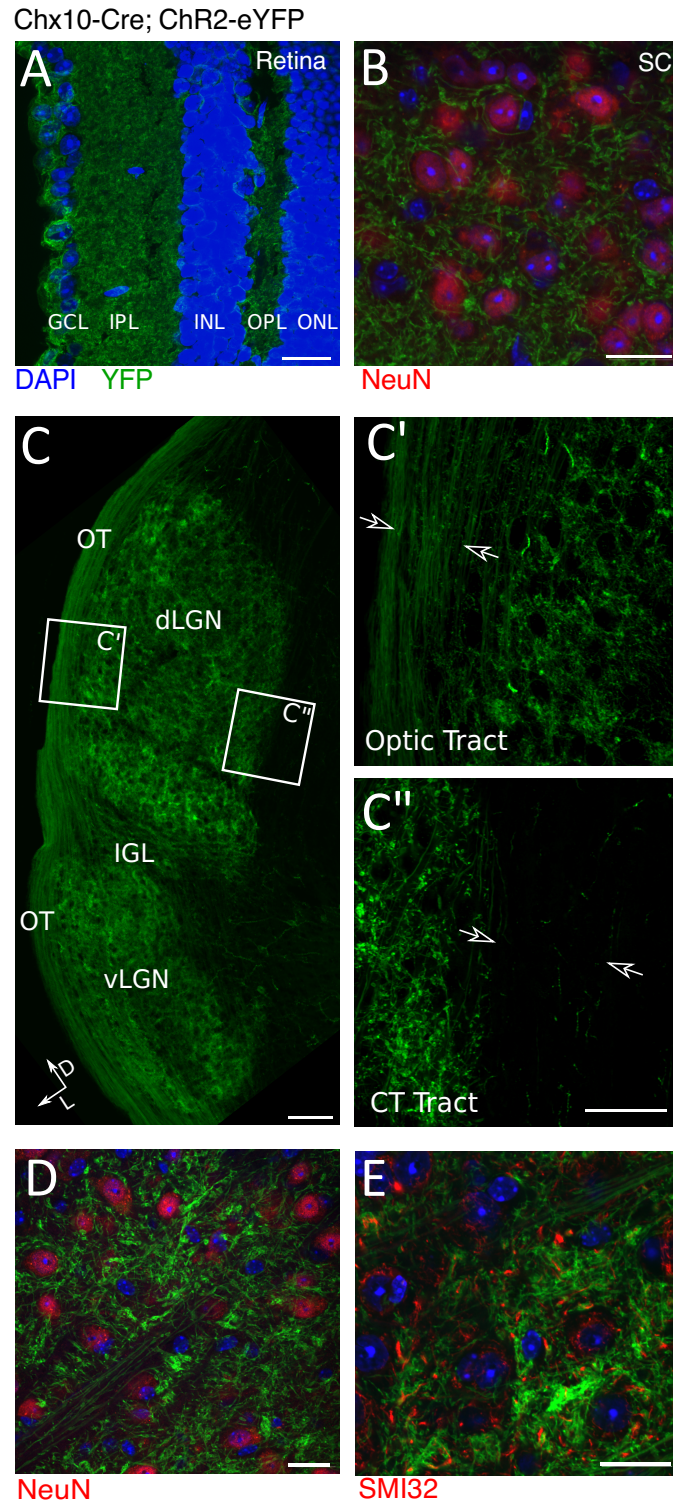


Figure 4.1: ChR2 expression is restricted to retinogeniculate afferents in *Chx10-Cre;ChR2* mice.

(A) Transverse section of a *Chx10-Cre;ChR2* retina shows expression of YFP in multiple layers of the retina, including RGC layer. (B) High-magnification view of the superior colliculus (SC)

Figure 4.1 (Continued)

showing YFP⁺ axons and bouton clusters (green), NeuN-positive cell bodies (Red), and DAPI-stained nuclei (blue); YFP expression is strictly absent from SC neurons. (C) Representative image of geniculate YFP labeling in *Chx10-Cre;ChR2* mouse. Inset views of YFP labeling in Optic Tract (OT) and its absence in the Corticothalamic Tract (CT) indicated in boxes. C', C'' Magnified views of corresponding boxed regions in C; filled arrows indicate YFP⁺ retinal axons in the OT, and empty arrows indicate near-complete absence of YFP signal in the region where corticothalamic axons enter the dLGN. Scale Bars: C:100 μ m, C':50 μ m (D) High-magnification view of the dLGN showing ChR2 expression in retinal axons (green), NeuN staining for neuronal cell body (red), and DAPI-stained nuclei (blue); on NeuN⁺ neurons express GFP. (E) High-magnification view of the dLGN showing ChR2 expression in retinal axons (green), SMI32-positive proximal TC neuron dendrites (red), and DAPI-stained nuclei (blue); YFP expression is absent from dLGN neuron dendrites. Scale Bar A, B, D, E=20 μ m

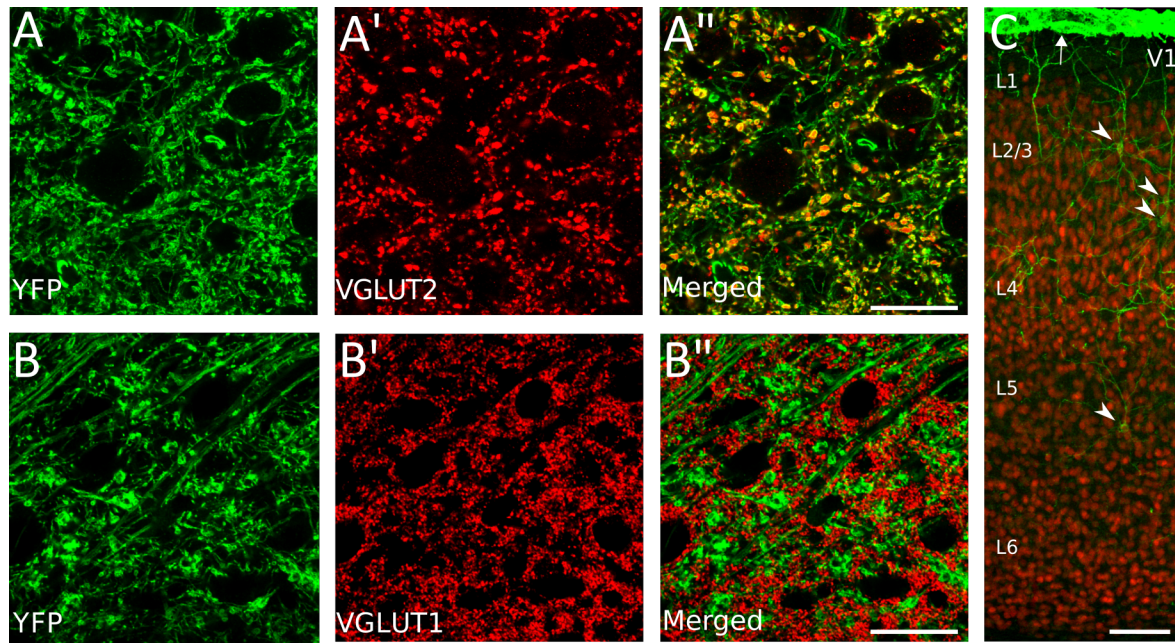


Figure 4.2: ChR2 expression in the dLGN is restricted to retinogeniculate afferents in *Chx10-Cre;ChR2* mice.

(A) High magnification view of dLGN, with YFP⁺ afferent boutons labeled in green and VGLUT2 stained in red. Most YFP⁺ boutons are also positive for VGLUT2. Scale Bar 20 μ m (B) High magnification view of dLGN; YFP⁺ afferent boutons in green and VGLUT1 staining in red. No YFP⁺ boutons co-localize with VGLUT1 puncta. (C) Representative view of leaky YFP labeling in *Chx10-Cre;ChR2* mice in the V1. Arrowheads: YFP⁺ neurons; arrow: YFP⁺ non-neuronal labeling. Quantification in text/methods. Scale Bar 100 μ m

experimental conditions. We therefore compared the maximal and minimal synaptic responses to electrical vs. optical stimulation.

Parasagittal slices of the dLGN from *Chx10-Cre;ChR2* mice were prepared at postnatal day (p) 27-34 and whole-cell voltage-clamp recordings performed as previously described (Figure 4.3A). These dLGN slices offered three ways to evoke retinogeniculate EPSCs: 1) distally with a stimulating electrode positioned in the OT (“eEPSC”; our established approach; Figure 4.3B); 2) distally with an Optic Fiber connected to a 470 nm LED light source (“fEPSC”, Figure 4.3B), and 3) proximally with full-field 470 nm optical stimulation through a 60x objective (“oEPSC”, Figure 4.3C).

We first assessed the synaptic response to maximal stimulation of retinal inputs by full-field optical stimulation. We compared a TC neuron’s eEPSC response following maximal electrical stimulation of the OT (0.2 msec, 400 μ A, black trace) to the oEPSC following full-field blue light stimulation (1 msec, 83 mW/mm², blue trace; experimental schematic as in Figure 4.3C). The oEPSC resembled the eEPSC in activation and decay kinetics, consisting of an inward current isolated at -70 mV holding potential with a fast dominant AMPAR component and slower activating and decaying NMDAR-mediated currents dominant at +40 mV (Figure 4.3D, 4.4B). oEPSCs were entirely abolished with the application of glutamate receptor antagonists (Figure 4.4B), ruling out the contribution of non-glutamatergic currents to the overall light-evoked response.

We found that the oEPSC exhibited a larger maximal peak amplitude than the eEPSC, with the median oEPSC 1.71 times greater than that of eEPSC (Figure 4.3E, Table 4.1). This difference was evident in both AMPAR and NMDAR-mediated currents; the ratio of AMPAR to NMDAR peak currents was not significantly different between eEPSCs and oEPSCs (Table 4.1).

Our data suggest that optogenetic stimulation activates severed axons that are not evoked by electrical stimulation of the OT. However, the large amplitude of the oEPSC

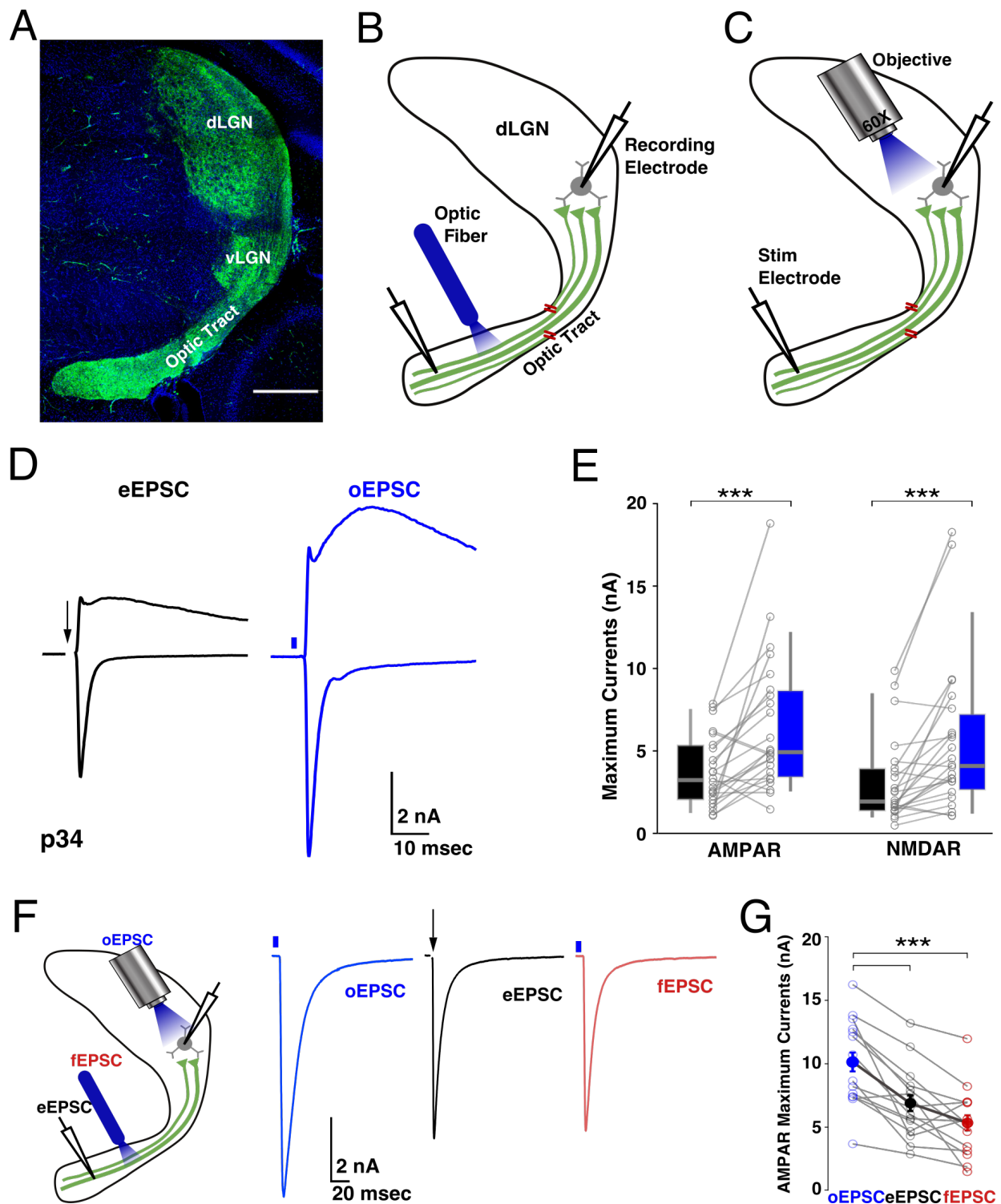


Figure 4.3: ChR2 stimulation of proximal retinal axons drives larger retinogeniculate maximal synaptic currents than OT stimulation.

(A) Low-magnification tiled confocal image of a post-fixed *Chx10-Cre;ChR2* parasagittal slice containing dLGN (B-C). Schematic of stimulation paradigms used in this study. Three different

Figure 4.3 (Continued)

types of stimuli are used to evoke EPSCs while recording from a TC neuron in whole-cell voltage clamp. (B) A glass pipet filled with saline inserted into the OT is used to deliver electrical stimulation (the response is termed “eEPSC”). 470nm light stimulation is delivered via a 200- μ m thick optic fiber positioned over the OT (“fEPSC”), or (C) via the 60x objective for full-field illumination to obtain maximal ChR2-driven currents (“oEPSC”). Intact and truncated axons are schematized (green; red dashed indicated axon severing in slice). (D) Representative eEPSCs (black) and oEPSCs (blue) recordings from the same TC neuron in a slice from *Chx10;ChR2* p34 mouse (holding potentials +40 and -70 mV). This experiment corresponds to schematic 2C. Here and subsequently, a black arrow indicates the location of a electrical stimulus artifact, whereas a blue bar indicates the timing of an optical stimulus. (E) Pairs of AMPAR (left) and NMDAR (right) maximal eEPSCs and oEPSCs were recorded from n=24 TC neurons. Grey markers connect responses from the same neuron, and box plots summarize each population of responses. For most cells, the oEPSCs was larger than the eEPSCs. N=24 cells from 13 animals. (F–G) Comparing peak responses to full-field blue light and localized stimulations of the OT from the same cell. (F). Left: experimental schematic. Right: Maximal AMPAR oEPSC (blue), eEPSC(black), and fEPSC(red) recorded from the same neuron in a p29 slice. Each trace averages 3-4 trials. (G). AMPAR peak EPSC data from experiment in 2F performed in 13 cells from 8 slices. Filled circles and black lines denote population averages with SEM, whereas gray lines connect empty circles that correspond to EPSCs from the same cell. See Table 4.1, 4.2 for detailed statistics.

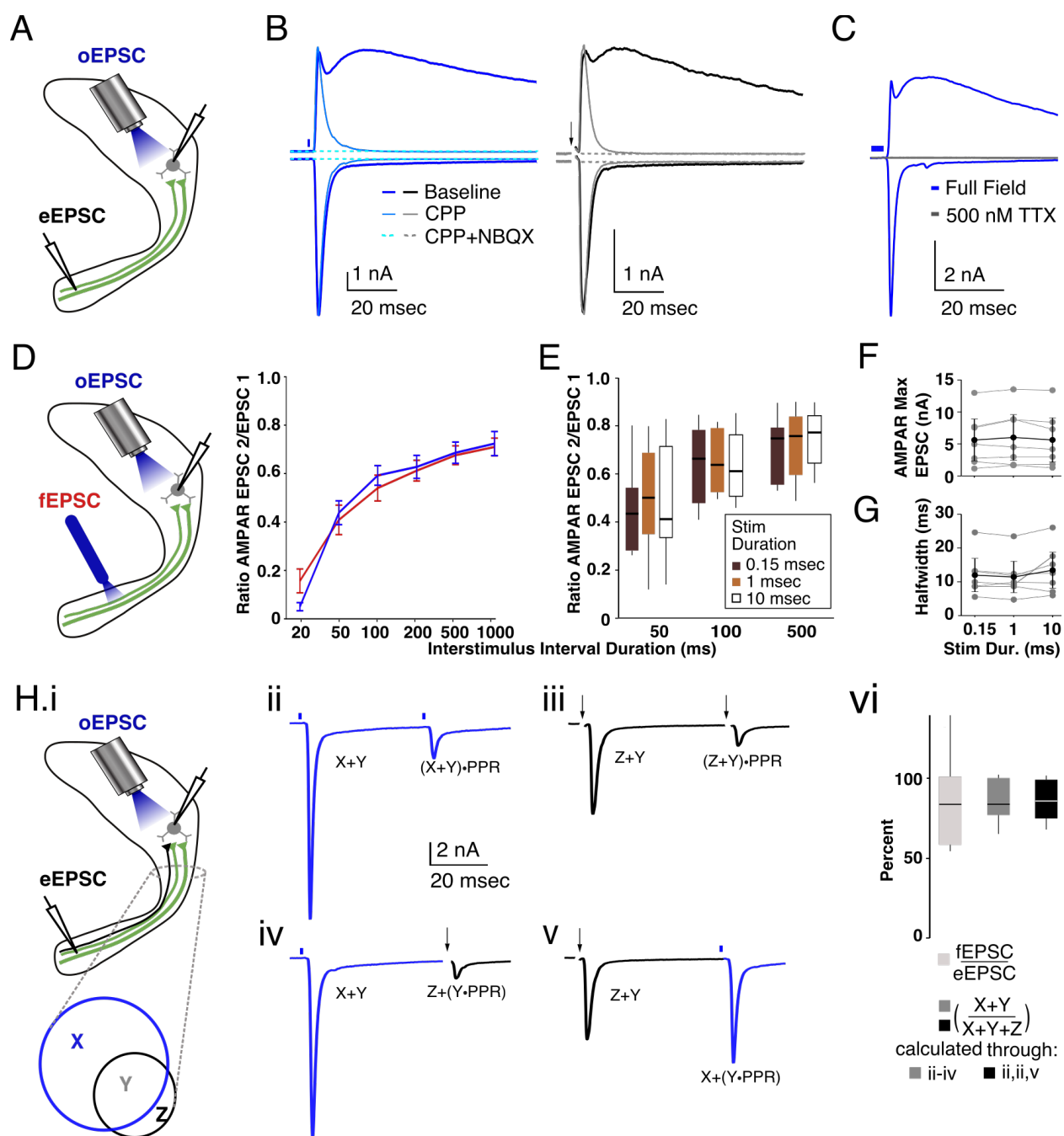


Figure 4.4: No Evidence of Disruption in Neurotransmitter Release with Full-Field Chr2 Stimulation.

(A) Experimental schematic for Figure 4.4B. (B). oEPSCs and eEPSCs have similar kinetics and pharmacologic sensitivity. Left, oEPSCs (blue traces) and right, eEPSCs (gray, and black traces) recorded at -70 and +40 mV before (darkest shade) and following the addition of CPP (20 μ M, thin light blue and gray lines) and NBQX (5 μ M, dashed lines) from the same p32 TC neuron. Traces average 3-5 trials. (C). Application of 0.5 μ M TTX completely abolishes the oEPSC. Representative example trace. Similar results were obtained from n=6 slices, mice

Figure 4.4 (Continued)

aged P55-100; Traces average 3 trials. (D) Left: Experimental Schematic. Right: Stimulation of the RGC axons several hundred micros from the presynaptic boutons (foEPSC, red) and near the release sites (oEPSC, blue) have similar timecourses of recovery. (E-F). No effect of stimulus duration on the oEPSC. Paired-pulse depression (E; $P=0.9$ Two-way Anova.), AMPAR EPSC amplitude (F; $p>0.09$ Wilcoxon), and halfwidth of AMPAR oEPSCs (G; $P>0.15$ Wilcoxon) do not vary with stimulation duration (0.15, 1, and 10 msec blue-light-on durations). Population data in F; cell-by-cell data in G, H. N.S. ANOVA. (G) Majority, but not all RGC axons express ChR2. Experimental schematic and rationale (i), example experiment traces from 1 cell (ii-v), and summary data (vi) of occlusion experiment to quantify % of RGC axons that express ChR2 in *Chx10;ChR2* mice. (i.) Venn diagram conceptualizing the population of axons in the OT of *Chx10;ChR2* mice. Blue circle refers to all axons that express ChR2; black circle refers to all axons that can be stimulated electrically within the OT; X refers to the proportion of ChR2-Axons that can't be stimulated in the OT; Y—axons that can be stimulated in the OT and also express ChR2; Z—axons that can be stimulated in the OT but do not express ChR2 and therefore cannot be stimulated with blue light. (ii-v). Example maximal occlusion experiment. Each trace averages 2-3 trials. Expressions adjacent to each peak refer to the venn diagram representation in 4.4Hi. PPR=paired-pulse ratio calculated for each cell by dividing the amplitude of the second eEPSC in ii or iii over the first (50 msec ISI). (ii). Two oEPSCs evoked 50 msec apart. (iii). Two eEPSCs evoked 50 msec apart. (iv) An oEPSC is followed by an eEPSC. (v). an eEPSC is followed by an oEPSC. (vi). Comparison of the the percent of all axons that can be stimulated with blue light and express ChR2, calculated from $n=25$ cells from $n=10$ slices to (right) the ratio*100% of the fEPSC/oEPSC from data shown in Figure 4.3G. As only 3 out of the four traces are necessary to calculate the proportion of each axonal population, we calculated it twice, through traces ii, iii, and iv and through ii, iii, and v; the two darker gray bars correspond to these two sets of calculations. $p>0.7$ Wilcoxon.

Table 4.1: Data Table Related to Figure 4.3E.

Analysis of AMPA and NMDAR EPSC maximals obtained with electrical and full-field optical stimulation of retinal inputs to the dLGN. For each cell, AMPAR and NMDAR EPSCs were obtained using both types of stimulation and were therefore compared using a paired non-parametric Wilcoxon test. oEPSC amplitudes are significantly larger than eEPSC amplitudes, but there is no difference in the AMPA:NMDA ratio, hinting that both types of stimulation activate portions of the same overlying population of synapse. oEPSC:ePSC mean =1.86 without 1 strong outlier.

	Matched Maximal EPSCs						
N Mice	13						
N Cells	24						
	AMPA (nA)		NMDA (nA)		AMPA:NMDA Ratio		oEPSC: eEPSC (AMPA and NMDA)
Stim Type	oEPSC	eEPSC	oEPSC	eEPSC	oEPSC	eEPSC	
Median	4.93	3.23	4.09	1.93	1.38	1.38	1.71
75% Q	8.63	5.33	7.21	3.91	2.04	1.73	2.52
25% Q	3.43	2.08	2.67	1.40	0.92	1.00	1.27
Mean	6.45	3.75	5.53	3.08	1.48	1.41	2.13
SEM	0.83	0.43	0.92	0.52	0.13	0.12	0.32
Wilcoxon (paired) p value	<0.0001		<0.0001		>0.66		

could be an overestimation, as aberrant enhancement of presynaptic release with ChR2 stimulation has previously been described at CNS synapses (Jackman et al., 2014). The results of a battery of controls argue against this explanation of our observations. First, blockade of action-potential-driven release by bath application of 0.5 μ M TTX, a sodium channel inhibitor, abolished the oEPSC in its entirety (Figure 4.4C; n=6), indicating that activation of ChR2 channels is insufficient by itself to stimulate neurotransmitter release from retinal boutons. Second, comparison of the peak amplitude of the oEPSC and eEPSC to the fEPSC recorded from the same cell (with the optic fiber placed at a location close to the site of electrical stimulation) showed that, like maximal eEPSCs, maximal fEPSCs were significantly smaller than oEPSCs evoked from the same cell (4.3F,G, Table 4.2). These findings argue against the possibility that ChR2 expression in axons broadens the action potential waveform leading to prolonged neurotransmitter release and larger EPSCs. Consistent with this conclusion, the response to pairs of pulses, separated by varying interstimulus intervals, was similar between oEPSCs and maximal fEPSCs despite their difference in amplitudes, indicating no effect of direct blue light bouton stimulation on the probability of release (Figure 4.4D). Further, varying the duration of full-field blue light stimulation (0.15-10msec) did not alter the probability of release, amplitude, and decay timecourse of the oEPSC (Figure 4.4E-G). Notably, a maximal occlusion paradigm showed that ~85% of RGC axons express ChR2 in these mice (Figure 4.4H; see methods). Together these experiments show that the larger amplitude of the oEPSC, when compared to responses to distal OT stimulation (eEPSC and fEPSC), is not a result of ChR2-mediated enhancement of neurotransmitter release, but can be attributed to the activation of a greater number of RGC axon terminals.

ChR2 stimulation isolates weak and strong single fiber inputs

We have previously shown that single RGC inputs to TC neurons can vary in amplitude from tens of pA to several nA, even in mature animals (Chen & Regehr, 2000; Hooks & Chen,

Table 4.2: Data Table Related to Figure 4.3 F-G.

Analysis of AMPAR EPSC amplitude and kinetics in response to three types of stimulation (Full-field, electrical, and optic fiber stimulations of RGC inputs) recorded from the same cells; data shown in Figure 4.3F. Paired Wilcoxon p-values are listed for each paired comparison (Bonferroni Correction p value =0.0167).

		Matched Maximal AMPAR EPSCs								
N Mice		7								
N Cells		13								
		EPSC Peak (nA)			Halfwidth (ms)			Norm. Halfwidth (ms/nA)		
Stim Type		eEPSC	fEPSC	oEPSC	eEPSC	fEPSC	oEPSC	eEPSC	fEPSC	oEPSC
Median		6.01	5.46	10.71	11.32	9.31	13.27	1.55	1.81	1.59
75% Q		8.64	6.99	13.14	15.52	15.41	23.42	2.55	2.69	2.31
25% Q		4.50	3.31	7.53	7.42	8.32	12.54	1.34	1.45	1.08
Mean		6.84	5.65	10.36	11.82	11.81	6.90	2.24	2.97	2.05
SEM		0.84	0.75	0.97	1.59	1.38	1.80	0.60	0.87	1.79
Wilcoxon (paired) p value	eEPSC		0.057	<0.001		0.84	<0.001		0.08	0.79
	fEPSC			<0.001			0.005			0.08

2006; Thompson et al., 2016). We therefore wondered whether the larger maximals obtained with optical stimulation of retinal inputs resulted from the inclusion of previously-missed strong fibers, or from a larger number of heterogeneous or weak single fibers. To distinguish between these possibilities, we adapted minimal stimulation protocols used with electrical stimulation (see supp methods of Noutel et al, 2011) for optic fiber stimulation of the OT (Figure 4.5A). Single fibers could be isolated with blue light delivered through an optic fiber. To find the minimal threshold stimulus intensity, the power of blue light was adjusted over a range of ~0.5-10 mW/mm². An example overlay of the responses at the ~50% failure intensity (Figure 4.5Aii) and the Current vs. Power plot (Figure 4.5Aiii) shows that with incremental increases in light intensity, the probability of evoking an fEPSC increased from 8.7% to 49.3%, confirming reliable activation of an EPSCs consistent with single fiber isolation. Figure 4.5A iv-v shows a single fiber response identified using the threshold approach in a different cell, where we incrementally increased the power intensity while sampling both the AMPAR and NMDAR responses. Because of its efficiency, we primarily relied on the latter threshold method to isolate single fibers using ChR2.

We next took advantage of the pronounced paired-pulse depression to pairs of stimuli—a characteristic of retinogeniculate synapses—to ask whether we could activate the same afferent axonal input using optical and electrical stimulation. While recording from a TC neuron, we could independently evoke a single fiber of similar amplitude and degree of short-term plasticity when placing the optic fiber and electrical stimulating pipet close to one another along the OT (Figure 4.5Bi). We reasoned that if the eEPSC and fEPSC recruit two different RGC axons, then stimulating the eEPSC should have no effect on the amplitude of the subsequent fEPSC, and vice versa. On the other hand, if the same axon generates the eEPSC and fEPSC, then the response to the second stimulus should reflect the previous short-term activity of that input — that is, the amplitude of the second stimulus will be depressed with any combination of stimuli. Figure 4.5Bii-iv shows an example of a single fiber input that exhibited similar paired-

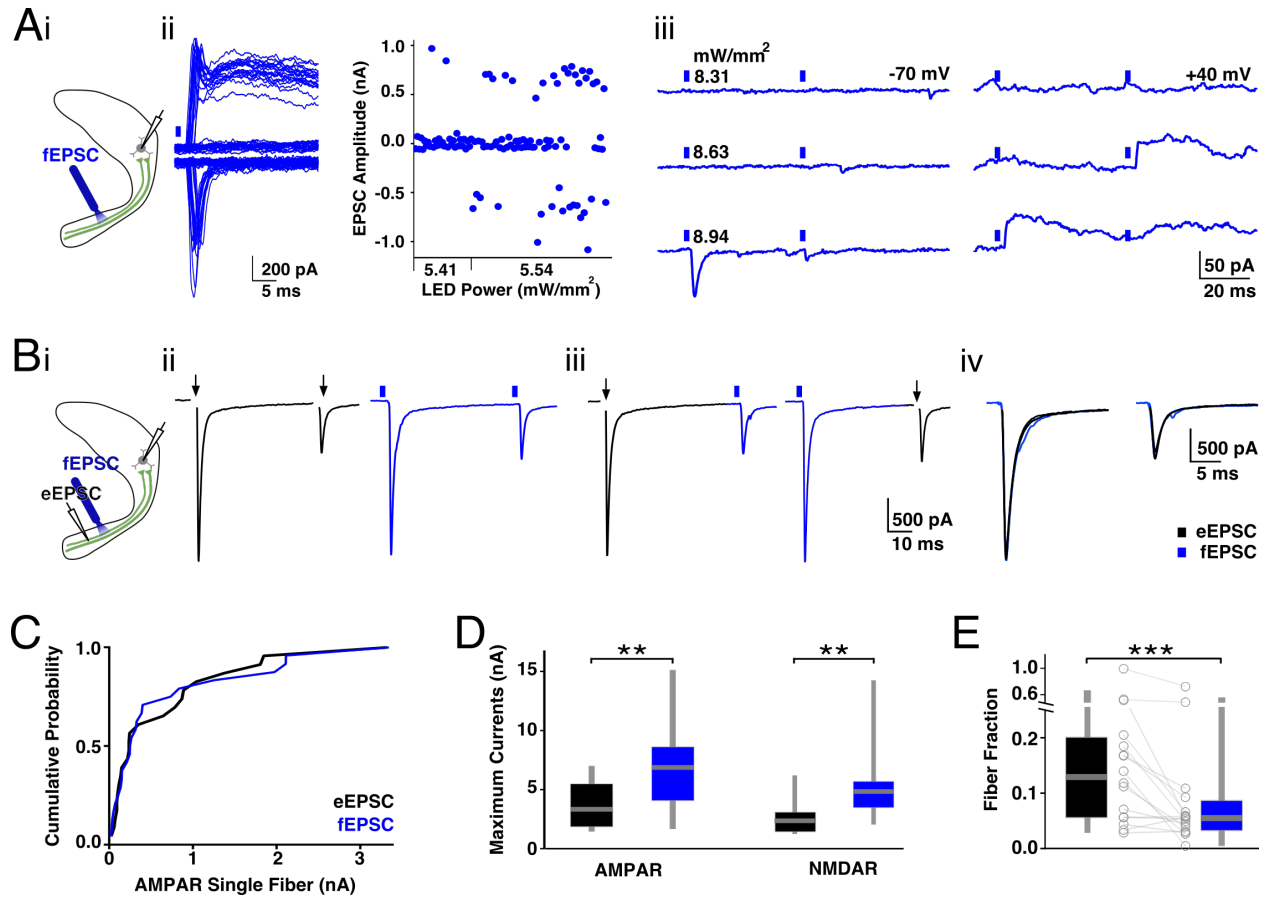


Figure 4.5: Isolation of Single Fibers with Chr2 reveals higher estimate of retinogeniculate convergence.

Single Fibers can be isolated with blue light illumination of the OT using either the failures (A) or threshold (B) methods. For Stats, see Table 4.3.

(A) (i). Experimental Schematic for single fiber isolation using an optic fiber to distally stimulate axons in the OT. (ii,iii). Failures method of single fiber isolation. Multiple fEPSC trials were recorded from a p32 TC neuron at light intensity set slightly below threshold at +40 and -70 mV holding potentials. This regime rarely (6.7%) evoked a single fiber input. The intensity was then increased slightly to threshold, where 49.3% of trials evoked a response. ii: Overlaid traces recorded at -70 mV (left) and +40 mV (right) at 5.4 mW/mm². iii: Current vs. power plot of all fEPSCs peak amplitudes, recorded below and at threshold light intensities. iv, v: Threshold method of single fiber isolation is another cell. fEPSCs were recorded while light intensity (mW/mm²) was incrementally increased from failure to produce a mixture of failures and successes. Two stimuli (separated by 50 msec) were used in each trial. Light intensity was increased gradually until the single fiber response became reliable while recording alternating trials at -70 (i) and +40 (ii) mV holding potentials. (B) Example isolation of the same single fiber using optical and electrical stimulation. Electrical stimulating electrode (top left) and optic fiber (i) positioned at a similar location along the OT were each used to isolate a single fiber of similar amplitude using method in 3B (ii). The AMPAR EPSCs for both stimuli exhibit similar paired pulse depression. Alternating optical (blue stim and trace) and electrical (black stim and trace) stimulation in pairs of pulses (iii) shows interaction between the two stimuli, confirming

Figure 4.5 (Continued)

that the two methods activate the same RGC axon. Each trace is the average of 3 trials.(vi) Responses to first (left) and second (right) stimulus from panels ii-v are overlaid. (C) Cumulative probability distribution of single fiber amplitudes obtained from the n=16 p30 cells where at least one single fiber was isolated using each of the two types of stimulation. $P>0.99$ Wilcoxon matched pairs. Note, this is a different set of cells than those in Figure 4.3E. (D) Group maximals from the same n=16 cells plotted in C. (E) Average fiber fractions from the same n=16 cells. Pairs of fiber fractions obtained using optical and electrical data are connected by a line. Fiber fractions obtained with electrical stimulation data are larger than with optical stimulation data from the same cells. Detailed Statis in Table 4.3.

Table 4.3: Detailed single fiber, maximal, and fiber fraction data for Figure 4.5C-E.

This table corresponds to the data plotted in Figure 4.5C-E, showing optically and electrically evoked data from the same set of cells. This set of Maximal EPSCs is distinct from the set shown in Figure 4.3.

N=12 mice	Single Fiber EPSC (nA)				Maximal EPSC (nA)				Fiber Fraction		eFF:oFF
	AMPA		NMDA		AMPA		NMDA				
	eEPSC	fEPSC	eEPSC	fEPSC	eEPSC	oEPSC	eEPSC	oEPSC	eFF	oFF	
N Sf or Cell	23		23		16		16		16		16
Median	0.24	0.27	0.23	0.15	3.34	6.88	2.37	4.84	0.12	0.06	1.57
75% Q	0.10	0.11	0.61	0.66	1.87	4.09	3.08	5.69	0.20	0.09	3.59
25% Q	0.95	0.81	0.09	0.07	5.48	8.61	1.43	3.49	0.06	0.33	1.06
Mean	0.64	0.65	0.37	0.42	3.58	6.52	2.47	5.48	0.21	0.12	3.81
SEM	0.17	0.18	0.08	0.12	0.47	0.88	0.31	0.81	0.06	0.05	1.55
Wilcoxon (Paired) p value	0.99		0.79		0.0021		<0.0001		0.01		

pulse depression with all stimulus combinations, indicating optical and electrical stimulation recruit the same single fiber input. These experiments demonstrate the feasibility of using light stimulation of RGC axons to isolate ChR2-expressing single fiber afferents.

To further confirm that the optical and electrical single fiber isolation protocols recruited the same population of retinal axons, we examined the distribution of single fiber responses obtained with both types of stimulation. Figure 4.5C compares the cumulative distributions of single fiber amplitudes isolated from 16 cells for which both optic fiber and electrical stimulation identified a single fiber input (not necessarily the same input). Both distributions span a range from tens of pA to several nA in amplitude and are statistically indistinguishable. A larger data set incorporating cells where only one type of stimulation was used to isolate a single fiber also showed no differences between eEPSC and fEPSC single fiber amplitudes (Table 4.4). Our data therefore demonstrate that optical stimulation of the OT can be used alongside electrical stimulation to assess SF amplitude distribution.

Lower fiber fractions reflect higher convergence with optical stimulation

We have so far shown that optical stimulation can provide a more accurate measurement of maximal retinal drive onto a given TC neuron by accounting for severed axons in a slice preparation while evoking the same distribution of single fiber inputs as electrical stimulation. With this approach, we reassessed the degree of convergence at the murine retinogeniculate synapse by first comparing the fiber fraction ratio (max EPSC/SF EPSC) of TC cells using electrical and optical stimulation data shown in Figure 4.5C (single fibers) and Figure 4.5D (maximals). Figure 4.5E plots the pairs of electrical (eFF) and optical (oFF) fiber fractions calculated for these cells; the median eFF was 1.6 times larger than the oFF in this dataset and also in a larger combined dataset including cells in which only an eFF or oFF was obtained (Table 4.3). Optical stimulation therefore identifies more inputs per TC neuron when compared to electrical stimulation, leading to a fiber fraction of 0.06.

Table 4.4: Detailed Single Fiber and Fiber Fraction Data related to Figure 4.5.

Additional data from cells where only one type of stimulation was successfully applied to obtain single fiber and maximal information has been included; As these contain unpaired data, an unpaired nonparametric Mann-Whitney test was applied to these data sets.

	Single Fiber EPSC (nA)				Fiber Fraction	
	AMPA		NMDA			
	eEPSC	fEPSC	eEPSC	fEPSC	eEPSC	fEPSC
N Sf or Cell	35	37	35	36	23	26
Median	0.23	0.28	0.16	0.17	0.07	0.05
75% Q	0.09	0.12	0.38	0.46	0.19	0.09
25% Q	0.85	0.67	0.09	0.07	0.04	0.03
Mean	0.54	0.56	0.30	0.36	0.17	0.10
SEM	0.12	0.12	0.06	0.08	0.05	0.03
Mann-Whitney p value	0.94		0.95		0.0297	

Both oFF and eFF from our current study are substantially lower than the initial estimate of 0.27 (Hooks and Chen, 2006, Noutel et al 2014, Table 4.6). In part, this difference arises from advances in brain slice preparation. To formally demonstrate this, we compared fiber fraction data reported in our previous studies obtained in different cutting solutions (Figure 4.6). With changes in the cutting solution, we found that acutely cut LGN slices contained more cells with a healthy appearance and allowed for longer-lasting, stable recordings. With improvements in slice health, our fiber fractions have declined (Figure 4.6A, Table 4.5). Maximal peak EPSC amplitudes measured through either glutamatergic AMPA or NMDA postsynaptic receptors were more than doubled in the optimized slices (Figure 4.6B also see Table 4.5). In contrast, the distributions of single fiber EPSC peak amplitudes were not statistically different among all three cutting solutions (Figure 4.6C), indicating that the improved solutions are not causing retinal axon sprouting or non-specific changes in postsynaptic glutamatergic receptors. Therefore, the enhanced cutting solutions preserve both the integrity of the cells and more of the severed retinal axons, and improve recording conditions for cell health, leading to increased maximal currents and a higher estimate of retinogeniculate convergence than previously estimated, decreasing the fiber fraction nearly 2-fold. Full-field optogenetic stimulation in the healthier slices recruited ~50% more inputs, further reducing the fiber fraction.

Simulation identifies many weak, few strong retinogeniculate contacts onto mature TC neuron

The fiber fraction was initially designed to compare the relative degree of retinogeniculate convergence over different conditions, but never intended to provide an exact measure of the number of inputs a TC neuron receives, because it relies on averaging over a broad range of single input strengths (See Materials and Methods in Hooks & Chen, 2008, Figure 4.5D). Thus, we sought to estimate convergence in a manner that takes into account differences in the synaptic weight of individual inputs by implementing a resampling simulation

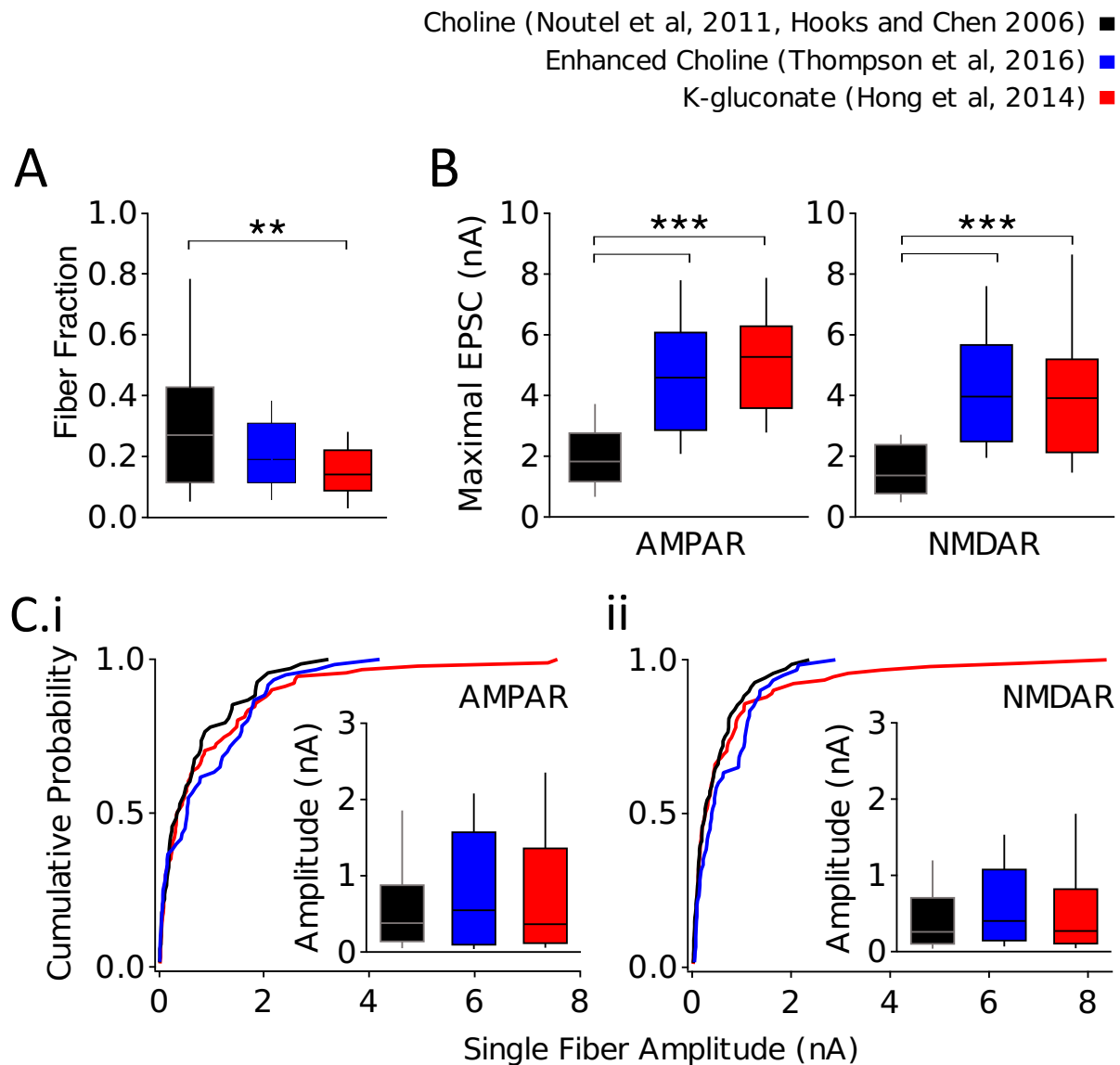


Figure 4.6: Higher convergence in healthier retinogeniculate slices.

A comparison of published data from mouse retinogeniculate slices prepared in three different cutting solutions (see methods). For stats, see Table 4.5. (A) Slices prepared in Enhanced Choline and K-gluconate cutting solutions, which improve the health of the slice relative to standard choline, produce a lower fiber fraction estimate of convergence. (B). Maximal AMPAR (left) and NMDAR (right) EPSCs amplitudes are larger in healthier slices. (C). Cumulative probability distributions of AMPAR (i) and NMDAR (ii) single fiber amplitudes from the three cutting solutions. Insets: box plot representation of the same data. N.S. K-W with Dunn. Data from B and C were collected from the same cells, and one average fiber fraction value combining AMPAR and NMDAR EPSC data for each cell were used in group comparisons in A.

Table 4.5: Detailed Single Fiber, Maximal, and Fiber Fraction Data for Figure 4.6.

	Single Fiber EPSC (nA)						Maximal EPSC (nA)						Fiber Fraction		
	AMPA			NMDA			AMPA			NMDA					
	Chol	Enh Chol	KGlu	Chol	Enh Chol	KGlu	Chol	Enh Chol	KGlu	Chol	Enh Chol	KGlu	Chol	Enh Chol	KGlu
N Mice	12	8	10	12	8	10	12	8	10	12	8	10	12	8	10
N Sf or Cell	68	60	91	68	60	91	45	32	41	45	32	41	45	32	41
Median	0.38	0.55	0.37	0.26	0.40	0.27	1.86	4.60	5.27	1.37	4.12	3.92	0.27	0.19	0.14
75% Q	0.88	1.57	1.37	0.71	1.08	0.82	2.85	6.13	6.28	2.40	5.69	5.19	0.43	0.31	0.09
25% Q	0.14	0.10	0.12	0.10	0.15	0.11	1.23	3.05	3.58	0.79	2.62	2.13	0.11	0.11	0.09
Mean	0.68	0.90	0.94	0.47	0.66	0.74	2.10	4.70	5.15	1.58	4.58	4.28	0.33	0.21	0.15
SEM	0.09	0.12	0.14	0.06	0.08	0.14	0.17	0.35	0.31	0.13	0.46	0.42	0.03	0.03	0.03
KW with Dunn	Enh Chol	1		>0.19			<0.0001			<0.0001			0.414		
	KGlu						<0.0001	1		<0.0001	1		0.001	0.192	

using our available datasets of oEPSC and electrically and optically isolated single fiber current amplitudes from P30 animals. Figure 4.7A shows the histogram distribution oEPSCs (n=68) obtained from *Chx10;ChR2* P30 animals that were used for this simulation. Figure 4.7B shows the amplitudes of 271 AMPAR single fibers obtained from p27-34 animals, pooling previously published and unpublished data (Figure 3.4J in Chapter 3/Hong et al, 2014, and other unpublished C57B6 experiments). Given that we find that eSF and fSF distributions are similar, we also included the electrical and optical single fiber amplitudes obtained for the present study. A single trial of the resampling simulation consists of two steps: 1) a maximal current is randomly chosen (Figure 4.7A); 2), single fiber inputs are then randomly chosen from the distribution (Figure 4.7B), and summed until the total current reaches that of the chosen maximal current. 50,000 trials generated a population of simulated cells, for which we recorded the number and amplitude (binned by 100 pA increments) of single fibers required to reach the maximal.

The simulation showed that 10.6 ± 6.5 (Mean; 1SD; SEM=0.03, median 9, IQR 6-14; 50,000 Runs) RGC inputs converge onto an average TC neuron (Figure 4.7C). However, these inputs range widely in amplitude (Figure 4.7B). Because strong single fibers are likely to drive TC neuron spiking more effectively than individually activated weak single fibers, it is important to determine the relative strengths of converging inputs to know how many presynaptic RGCs make a substantial contribution to the activity of postsynaptic TC neuron. If we define the "threshold strength" as the peak amplitude of an retinogeniculate AMPAR EPSC that can drive TC neuron spiking in response to one or a pair of OT stimuli, we can plot the number of single fibers that exceed threshold for each simulation trial as a function of the threshold strength (in 100 pA intervals, Figure 4.7E). In an *in vitro* study, we previously showed that the retinogeniculate threshold strength is 600 pA at P30 (Liu et al, 2008). We therefore applied his threshold to our simulated results to determine the proportion of all functionally detectable inputs that can robustly drive TC neuron inputs. "Weak" inputs (smaller than 600 pA)

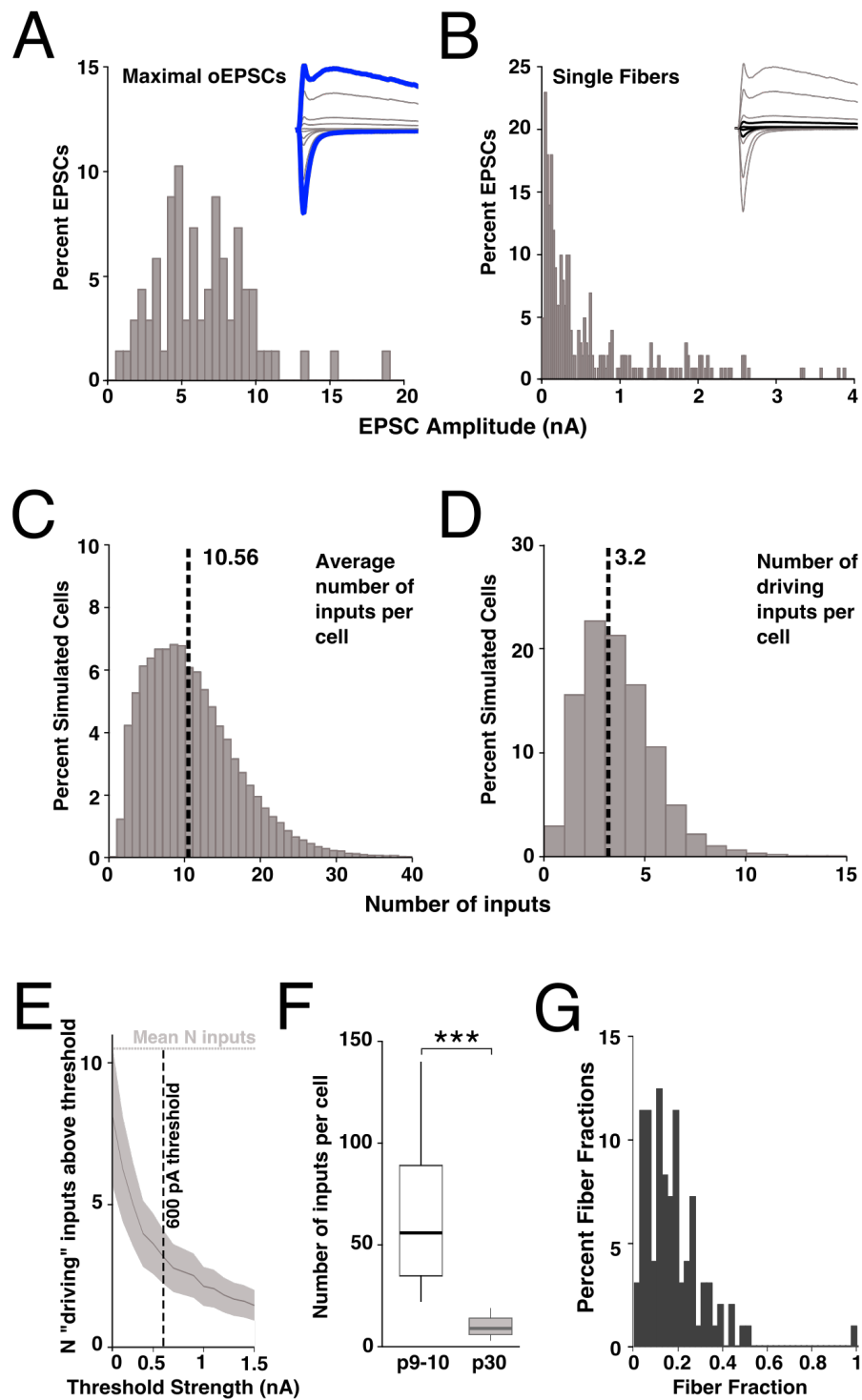


Figure 4.7: Simulation of Retinogeniculate Convergence.

(A, B). Simulation Inputs. Histogram distributions of maximal $n=68$ oEPSC amplitudes from P30 *Chx10;ChR2* animals (A) and distribution of 271 single fibers combined from multiple studies

Figure 4.7 (Continued)

P30 (B). Inset traces illustrate the type of data plotted. (C-D) Histogram distributions of simulation results. (C). Plot showing that average number of inputs across the population of 50,000 simulated cells. The mean is indicated with a black dashed line. Median: 9, IQR 6-14. (D) Plot showing the average number of “driving” inputs that exceed 600 pA cell across the population of 50,000 simulated cells. Average number of driving inputs indicated with black dashed line. Median: 3, IQR 2-4. (E) The mean $\pm 1/2$ SD number of “driving” inputs is plotted as a function of changing the threshold strength for categorizing “driving” inputs. Threshold analysis of simulated LGN cells was performed at 100-pA increments. (F) A box plot compares simulation results for the average number of convergent inputs at P9-10 vs. P30. *** $p < 0.001$ MW. (G) Histogram plot showing the distribution of $n=96$ electrical-data p30 fiber fractions, combining those obtained for this study (Figure 4.5, Table 4.4) and those previously published in Thompson et al, 2016.

made up 7.4 ± 5.3 (Mean, 1SD; median 6, IQR 3-10) inputs onto each cell, whereas “strong” inputs (greater than 600pA) comprised 3.2 ± 1.9 (Mean, 1SD; 3 median, 2-4 IQR) inputs per cell (Figure 4.7D, dotted line). Therefore, on average, ~34% of inputs to a TC neuron are substantially strong enough to reliably drive AP firing in TC neurons alone.

Many RGC inputs are functionally eliminated over development

The observations of higher convergence than previously estimated in P30 mice raise the possibility that the degree of developmental retinogeniculate refinement has been overestimated (Hammer et al, 2015). Indeed, at face value the low mean fiber fraction obtained using ChR2 stimulation (0.097) is in a similar range to previously reported immature fiber fraction (~0.1 Hooks 2006). However, these values cannot be directly compared because, as we have shown here, ChR2 stimulation captures substantially more inputs than electrical stimulation.

To reassess developmental refinement, we first asked whether expression of ChR2 is sufficiently strong in *Chx10;ChR2* RGC axons to drive oEPSCs in slices prepared from young animals (P9-10). We took advantage of the fact that retinogeniculate synapse development involves insertion of AMPAR into synapses that already contain NMDARs. Indeed, the amplitude of maximal NMDAR EPSCs is already very large at P10, and does not significantly increase with age, whereas maximal AMPAR EPSC strengthen substantially with development (Figure 4.8B; Table 4.6, Chen and Regehr 2000). Therefore, we could use the peak amplitude of the NMDAR EPSCs to assess the relative level of ChR2 expression. Figure 4.9A shows that oEPSC amplitudes increase dramatically between P9-P16. However, comparison of the maximal eEPSC amplitudes to that of oEPSCs from the same cell (ratio of eEPSC/oEPSC amplitude) shows that blue light can only stimulate ~20% of the maximal electrically stimulated EPSC at P9. The ratio of eEPSC/oEPSC amplitude declines to mature levels between P9-16, consistent with a gradual increase in ChR2 expression (Figure 4.9B, Table 4.7). Graded increase in blue light stimulus intensity and duration over development further confirmed the

slow increase in ChR2 expression (Figure 4.9C). We therefore concluded that, despite embryonic onset of expression of the Cre driver (Rowan and Cepko, 2004), ChR2 expression in *Chx10;ChR2* animals does not functionally mature until at least P16, after the bulk of refinement is complete, and is therefore unsuitable for early developmental assessment.

To circumvent the slow onset of ChR2 expression during development, we opted for a direct comparison of the electrical single fiber amplitudes obtained at P9-10, P30 (the same data used above), and a small P60+ data set in conditions that produced healthier slices. Consistent with previously reported results, both AMPAR and NMDAR single fiber amplitude distributions grossly favored the very weak before eye opening (Figure 4.8C, Table 4.7). As a result, the eFF before eye opening was considerably smaller than at P30 (same data as above) or P60 (Figure 4.8A, Table 4.7). These results demonstrate not only that we can still detect developmental pruning with optimized slice conditions, but that the fiber fraction can continue to function as a robust tool for comparing different ages or conditions.

Finally, we reran our resampling simulation with the P9-10 electrical single fiber and maximal NMDAR EPSC data sets. In order to account for the axons that cannot be stimulated electrically in slice, we assumed that if ChR2 was fully expressed at P9-10, the distribution of ratios of oEPSC/eEPSC would be similar to that at P30. Therefore, each randomly chosen P9-10 maximal eEPSC was multiplied by a randomly drawn oEPSC/eEPSC ratio from the P30 distribution to simulate a population of likely oEPSC P9-10 maximals. This simulation resulted in an average of 73 (SD 62) inputs per P9-10 neuron, ($p < 0.001$ from P30; Figure 4.7F). Our previous *in vitro* studies demonstrated that the threshold strength at P9-10 is 100 pA (Liu & Chen, 2008). Therefore, only $8.5 \pm \text{SD}4.9$ (<10%) inputs are strong enough to drive AP firing.

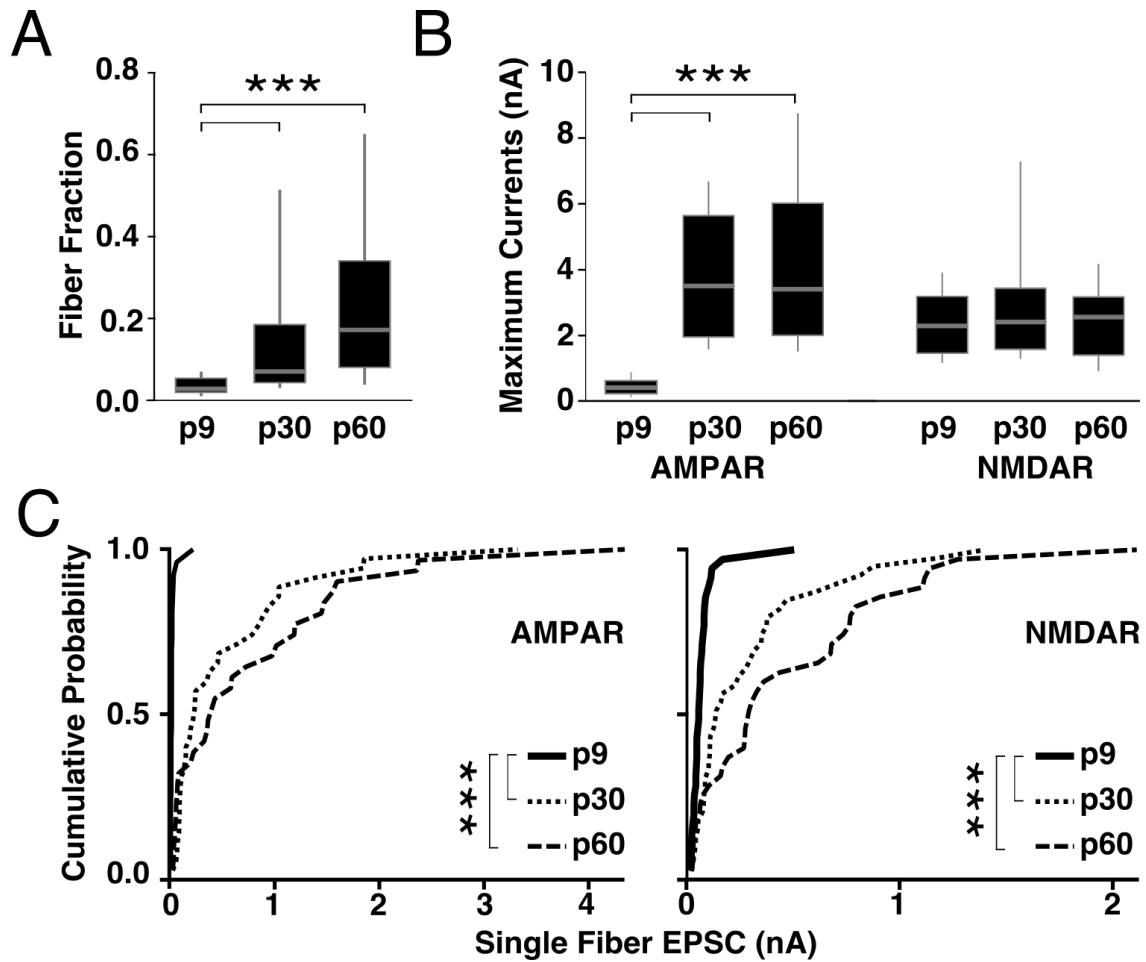


Figure 4.8: Retinogeniculate Development re-assessed with the electrical fiber fraction.

(A). The eFF significantly significantly increases after eye opening. (B). Maximal AMPAR eEPSCs dramatically increase over development, whereas Maximal NMDAR eEPSCs are robust before eye opening. (C). Cumulative probability distributions of single fiber eEPSC amplitudes recorded from P9-10, P30, and P60 animals. Both the single fiber AMPAR and NMDAR EPSCs are much smaller before eye opening than at P30 or P60. The P30 data in Figs A-E replots eEPSC data presented in Figure 4.5 and Table 4.3.

Table 4.6: Detailed single fiber, maximal, and fiber fraction change over development, related to Figure 4.8.

		Single Fiber EPSC (nA)					
		AMPA			NMDA		
Age Group		p9	p30	p60	p9	p30	p60
N Mice		8	13	10	8	13	10
N Sf or Cell		26	31	31	35	31	31
Median		0.02	0.23	0.40	0.06	0.17	0.28
75% Q		0.02	0.89	0.12	0.08	0.38	0.68
25% Q		0.01	0.10	0.07	0.04	0.09	0.06
Mean		0.02	0.56	0.78	0.07	0.31	0.44
SEM		0.01	0.13	0.17	0.01	60.17	0.08
KW/Dunn p value >	p30	0.0001			0.0001		
	p60	0.0001	1.000		0.0001	1.000	
		Maximal EPSC (nA)					
		AMPA			NMDA		
Age Group		p9	p30	p60	p9	p30	p60
N Mice		8	13	10	9	17	11
N Sf or Cell		28	23	18	28	23	18
Median		0.38	3.50	3.41	2.29	2.41	2.56
75% Q		0.27	5.64	6.03	3.19	3.43	3.17
25% Q		0.60	1.95	2.00	1.46	1.58	1.40
Mean		0.45	3.87	4.18	2.39	2.98	2.44
SEM		0.04	0.37	0.41	0.30	0.33	0.38
KW Dunn p value >	p30	0.0001			1.000		
	p60	0.0001	1.000				
		Fiber Fraction			AMPA:NMDA Ratio		
		p9	p30	p60	p9	p30	p60
N Mice		9	13	10	9	17	11
N Sf or Cell		28	23	18	49	43	28
Median		0.03	0.07	0.17	0.19	1.34	1.57
75% Q		0.05	0.19	0.34	0.13	1.01	1.23
25% Q		0.02	0.04	0.08	0.25	1.77	2.03
Mean		0.05	0.17	0.23	0.20	1.45	1.64
SEM		0.01	0.05	0.05	0.01	0.08	0.11
KW Dunn p value >	p30	0.0001			0.0001		
	p60	0.0001	0.060		0.0001	1.000	

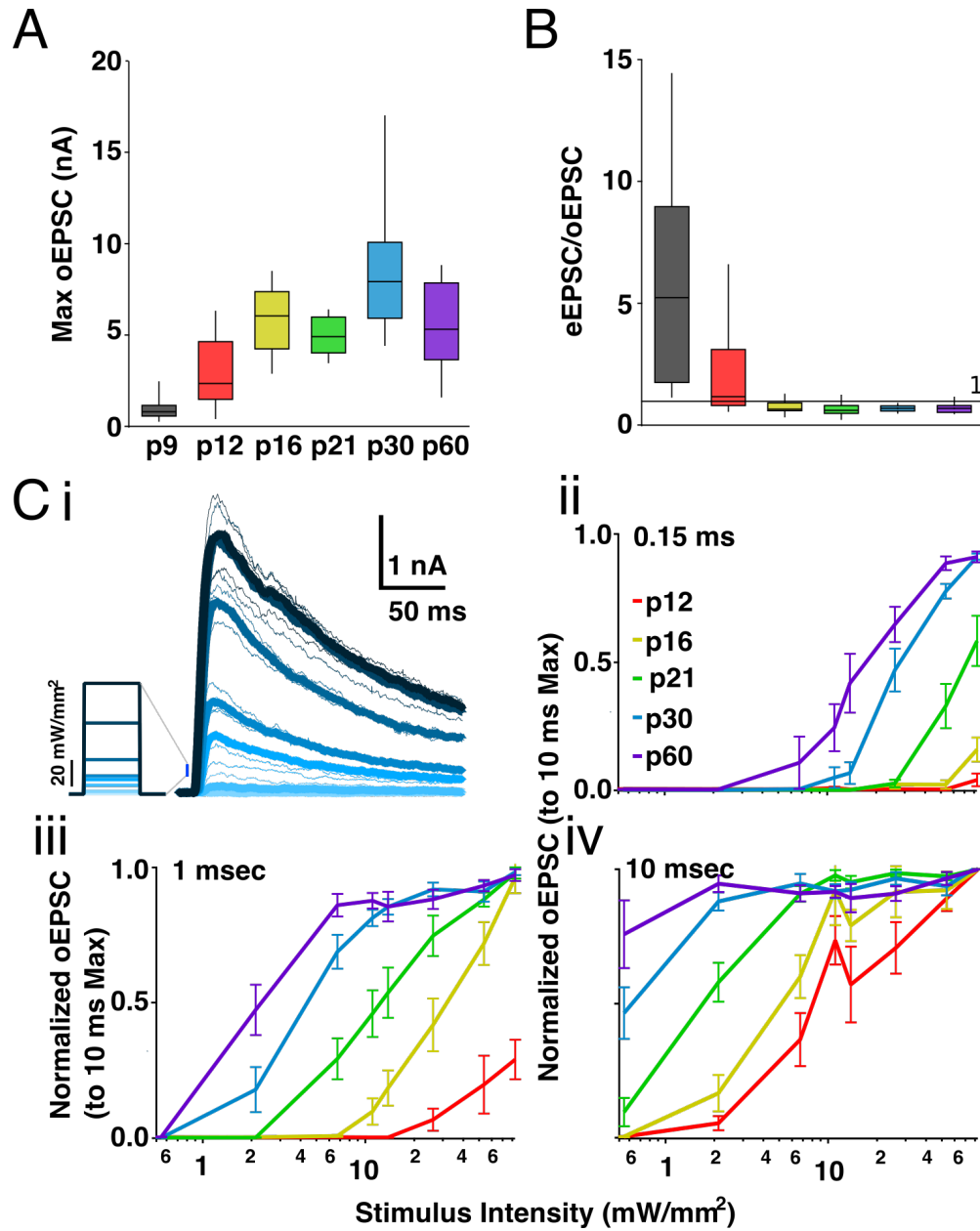


Figure 4.9: ChR2 expression in *Chx10;ChR2* increases throughout development.

NMDA receptor currents were recorded in dLGN TC neurons in parasagittal slices from *Chx10;ChR2*. Colors correspond to ages as marked in A. Stats for this figure are listed in Table 4.7. (A). The amplitude of NMDAR oEPSCs increases from P9-P16. (B). The ratio of maximal NMDAR eEPSCs to oEPSCs across slices prepared from different ages, corresponding to the proportion of electrically-accessible retinogeniculate axons that also express ChR2. eEPSCs are much larger than oEPSCs at P9 and P12, but oEPSCs exceed eEPSCs after P16. (C). Sensitivity to blue light stimulation across development. (i). Example (p21) recording of oEPSCs evoked with blue light of different intensities, with thicker lines

Figure 4.9 (Continued)

corresponding to the average of thinner traces of the same color. Shades of blue correspond to the magnitude of light intensity used to evoke those oEPSCs, as indicated with the stimulus steps on the left. (ii-iv). The NMDAR oEPSC (normalized to the maximal response evoked with full power 10 msec long light pulses) is plotted against the intensity of 0.15, 1, and 10 msec-long blue light pulses. Much higher light intensities are required to evoke responses in younger than older animals. The highest available intensity is insufficient to stimulate all inputs until p21 at 1 msec pulse duration.

Table 4.7: Detailed analysis and statistical test for assessment of the development of ChR2 expression shown in Figure 4.9

	Peak NMDAR oEPSC Amplitude (nA)						KW with Dunn p values					
Age	p9	p12	p15	p21	p30	p60		p9	p12	p15	p21	p30
N animals	5	6	4	5	4	4	p9					
N cells	13	23	13	10	18	15	p12	0.4267				
Median	0.81	2.35	6.05	4.92	7.92	5.32	p15	0.008	0.460			
IQR	0.58	3.15	3.13	1.78	4.15	4.21	p21	0.5407	1	1		
Mean	0.99	2.95	5.89	4.94	8.67	5.45	p30	<0.001	0.0008	0.995	1	
SEM	0.20	0.46	0.52	0.32	0.92	0.67	p60	0.019	1	1	1	0.41
	NMDAR ePESC/oEPSC						p9					
							p12	0.8391				
Median	5.23	1.17	0.65	0.64	0.68	0.68	p15	0.0005	0.1441			
IQR	7.21	2.30	0.32	0.34	0.21	0.28	p21	0.6601	1	1		
Mean	5.88	2.14	0.76	0.67	0.68	0.71	p30	<0.0001	0.0081	1	1	
SEM	1.29	0.43	0.08	0.09	0.04	0.07	p60	0.0013	0.2195	1	1	1
	Peak NMDAR eEPSC amplitude (nA)						p9					
							p12	1				
Median	3.31	3.08	3.88	3.02	5.07	3.28	p15	1	1			
IQR	3.50	1.88	2.32	1.64	2.95	2.32	p21	1	1	1		
Mean	3.92	3.55	4.36	3.01	5.62	3.65	p30	0.5401	0.0167	1	0.058	
SEM	0.64	0.44	0.60	0.33	0.50	0.46	p60	1	1	1	1	0.23

DISCUSSION

In this study, we used ChR2 expression to quantify the total functional drive from retinal inputs onto TC neurons. Together with measurements of single fiber strength and a resampling simulation, we estimate the functional convergence at the retinogeniculate synapse, taking into account the diversity of RGC input strengths. Our estimate shows that the average P30 mouse dLGN neuron receives ~10 afferent RGC inputs. However, only a third of these inputs are strong enough to independently drive activity of the TC neuron. Our results highlight the critical importance of evaluating the functional correlates of connectivity schemes identified by anatomical methods, and suggest flexibility in the retinogeniculate system that may permit dLGN neurons to perform diverse roles depending on the context of retinal and modulatory state. More broadly, a more nuanced view of the dLGN as a model thalamic nucleus highlights a growing recognition of the contribution of subcortical circuits to sensory processing normally attributed to the cortex, and informs more broadly the role of thalamic circuits in complex sensory and cognitive processes (Sherman, 2007; Schmitt & Halassa, 2016).

Comparing Functional Retinogeniculate Convergence across species

We report a higher functional convergence of retinogeniculate inputs than has been previously appreciated in mice or other mammals. Our results differ from prior *in vitro* work in mice largely because we have used novel tools to activate previously inaccessible axons (Chen & Regehr, 2000; Jaubert-Miazza et al., 2005; Lee et al., 2014). However, they also differ from the prevailing view of high specificity of connectivity between RGCs and LGN neurons (Bishop et al., 1958; Mastronarde, 1987; Carandini et al., 2007; Sincich et al., 2007). This view is based largely on *in vivo* recordings that correlate spiking activity of RGC-TC neuron pairs in cats and primates (to our knowledge, these experiments have not been repeated in rodents). These studies report one of several dominant RGCs that drive TC neuron firing, but do not rule out the

presence of additional weaker inputs (Hubel & Wiesel, 1961; Cleland & Levick, 1971; Cleland et al., 1971; Levick et al., 1972; Usrey et al., 1999; Yeh et al., 2009).

Studies that most strongly support a high degree of retinogeniculate specificity largely use the s-potential—a small signal that usually precedes a TC action potential in a single unit extracellular trace— as proxy for the behavior of a dominant RGC input, reflecting the EPSC that follows synaptic transmission (Bishop et al., 1962; Coenen et al., 1972; Lee et al., 1983; Wang et al., 1985; Kaplan et al., 1987; Sincich et al., 2007). However, only very large or several coincident inputs are needed to drive a detectable s-potential, likely reflecting the synchronous activity of multiple RGC inputs (Hubel & Wiesel, 1961; Bishop et al., 1962; Kaplan & Shapley, 1984), as visual stimulation enhances the synchrony of RGC activity (Usrey et al., 1999; Rowe & Fischer, 2001; Shlens et al., 2008). Furthermore, classic EM and functional observations have proposed differences in the retinogeniculate convergence among two streams of information in cat LGN: TC X-cells receive one dominant RGC input, whereas TC Y-cells can be innervated by 10 or more RGCs (Mastronarde, 1987, 1992; Hamos et al., 1987; Robson, 1993). There is morphological evidence for analogous X- and Y- streams in mice (Krahe et al. 2011; El-Danaf et al. 2015), but functional distinctions are still controversial (Denman & Contreras, 2016; Morgan et al., 2016; Sriram et al., 2016). We did not find evidence of functional separation between high vs. low-convergent TC neurons in our own analysis of >90 fiber fractions (Figure 4.7G).

Simultaneous *in vivo* recordings of RGCs in retina and TC neurons rather than s-potentials in cat have shown that single RGCs can drive as little as 1% to as much as 82% of postsynaptic spiking of both X and Y neurons (Alonso et al., 1996; Usrey et al., 1999; Rathbun et al., 2010). No X or Y TC neuron received all of its inputs from only one RGC in these samples. The finding that the majority of isolated RGCs contribute <50% of the postsynaptic neuron's activity is consistent with the broad distribution of the single fiber population we show *in vitro* in mice, and corroborates prior *in vivo* observations that multiple RGCs can drive TC neurons (Hubel & Wiesel, 1961; Cleland & Levick, 1971; Cleland et al., 1971; Cleland & Lee, 1985; Mastronarde,

1992; Dan et al., 1998). Indeed, the landmark study that reconstructed a single cat X-RGC axon arbor and showed one TC X-cell that received all of its 176 synapses/ 59 terminals from just one RGC axon also described three other TC neurons, including one Y-cell, that received weaker inputs from the same axon (Hamos et al., 1987). While dual-recording or EM reconstruction experiments have not been extended to the primate, work in the koniocellular TC neurons of marmosets showing orientation selectivity and binocular convergence suggests that primate TC neurons can also support the integration of multiple RGC inputs (Cheong et al., 2013; Zeater et al., 2015).

Taken together with our findings, the literature shows that RGC inputs that dominate TC neuron firing are only a subset of a larger number of convergent inputs in mammals. Differences in the exact number of convergent inputs, and the relative weights of these inputs may distinguish mice from other species.

Structure versus Function at the Retinogeniculate Synapse

Functional convergence of multiple retinogeniculate inputs is consistent with recent EM connectomics and retrograde rabies tracing studies of the mouse dLGN, which identify multiple RGCs contacting TC neurons (Hammer et al., 2015; Morgan et al., 2016; Rompani et al., 2017). However, these anatomical studies reveal a much higher range for the number of converging inputs than our functional estimate— up to 40-91 inputs. These numbers are much harder to reconcile with existing models of retinogeniculate function and basic observations about receptive field size and diversity than is our data (Alonso et al., 2006; Sincich et al., 2009; Martinez et al., 2014; Usrey & Alitto, 2015).

The dissociation between the functional and anatomical studies may reflect an artifact of development. As replicated again here, the retinogeniculate synapse undergoes robust functional refinement between the ages of P10-30 (Chen & Regehr, 2000; Ziburkus & Guido, 2006). In this system, synapse elimination precedes axon retraction by many weeks. The

decrease in the number of converging RGC inputs and the strengthening of remaining inputs corresponds with changes in synaptic bouton size and spatial location that occur up to P30. Nonfunctional axon branches, however, do not retract until well after P30 (Hong et al., 2014). Anatomical characterizations of retinogeniculate connectivity in mice have all been performed around P30 (Hammer et al., 2015; Morgan et al., 2016; Rompani et al., 2017). This raises the possibility that EM tracing may have identified boutons lacking functional glutamate receptors (silent synapses) as viable contacts, while rabies tracing particles could have infiltrated not only functional synapses but also functionally eliminated but unretracted remnant synaptic structures of closely juxtaposed pre- and post-synaptic membranes (Callaway, 2008). Further, these studies were performed within the thalamic critical period (p21-35), a window of time when connectivity is still quite plastic (Hooks & Chen, 2006; Thompson et al., 2016), and remodeling of afferent inputs can easily occur with the insertion or removal of synaptic release sites and AMPARs (Kiehl et al., 2009; Louros et al., 2014).

Choice of focus on different LGN regions may also explain discrepancies in structural and functional convergence estimates. Rompani and colleagues restricted their study to the binocular region of the dLGN, which exhibits different integrative properties than the monocular region where we performed our studies (Howarth et al., 2014). Notably, Morgan and colleagues explored the monocular region, but saw many more convergent axons than both the monocularly-innervated neurons identified by rabies tracing and our functional estimate. However, they point out that their estimate may exaggerate actual convergence by a factor of 2 or 3, because they were not able to account for potential axon branching at the level of the OT (Dhande et al., 2011; Chen et al., 2016).

Despite differences in species, maturation stage, technical approach, and study focus, anatomical studies agree that multiple RGCs can contact the same TC neuron in a variety of configurations (Hamos et al., 1987; Robson, 1993; Hammer et al., 2015; Morgan et al., 2016; Rompani et al., 2017). The contribution of our work to this literature is to emphasize the

importance of verifying the functional relevance of anatomically detectable contacts. Together, these results show that neither connectomics nor functional analysis alone can fully describe even a simple “relay” circuit. Instead, synergy between multiple approaches is critical to understanding the relevance of any one piece of evidence.

Implications of Convergence

Our results demonstrate that in addition to a few strong retinal drivers, many weak retinal inputs also provide functional contacts to mature TC neurons. The functional role of weak RGC inputs that persist into adulthood in both mice and other species remains unclear. Our analysis in mice shows no clear separation between populations of strong drivers and weak remnants at any level of analysis, suggesting a continuity of functional relevance. While the threshold strength is 600 pA for a single or pair of EPSCs to drive TC neuron firing *in vitro*, weaker inputs may contribute to TC spiking if they are active alongside strong inputs, or under modulated conditions that change the membrane resistance (Ramoia & McCormick, 1994; Kielland & Heggelund, 2002; Augustinaite & Heggelund, 2007; Budisantoso et al., 2012). Weak inputs have been proposed to synchronize the activity of groups of dLGN neurons, providing effective coincident stimuli for the activation of cortical neurons, which receive many converging geniculate inputs (Alonso et al, 2006; Usrey & Alitto, 2015). Moreover, retinogeniculate convergence can increase signal-to-noise in thalamic circuits to improve perceptual acuity, create novel receptive fields that increase the continuity in visual or temporal space or form novel feature detectors absent in the retina (Mastrorade, 1992; Usrey et al., 1999; Alonso et al., 2006; Martinez et al., 2014).

The persistence of small inputs lends support to a shift in conceptualizing the function of the LGN, from a simple relay to rather a complex network (Sherman, 2007; Kaplan, 2012; Weyand, 2016). Using rabies tracing, Rompani and colleagues (2017) have detected convergence of putative contacts from anatomically diverse. Although it is still not known

whether these contacts are functional, the finding suggests that inputs of different subtypes of RGCs may converge onto the same TC neuron to generate novel receptive field features in LGN, adding a new dimension to thalamic processing. For example, information encoding features of visual space that are not typically probed with the classic visual stimulation paradigms *in vivo*, such as that of intrinsically photosensitive RGC, may provide diffuse weak contacts that broadly modulate the integration of information from classical RGC subtypes.

During the thalamic critical period (P20-35), changes in visual experience and cortical feedback can increase the functional convergence of the retinogeniculate synapse (Hooks & Chen, 2006; Thompson et al., 2016). Experience can modulate retinogeniculate synaptic weights by activity- or experience-dependent insertion or removal of AMPAR subunits (Kielland et al., 2009; Louros et al., 2014). This mechanism is thought to fine-tune connectivity between RGCs and TC neurons to adapt to the visual environment. If this plasticity persists further into adulthood, it may enable plasticity of integration of various information streams by TC neurons or neuron networks. This plasticity could eventually serve as a tool for correcting circuit defects secondary to development or disease.

CHAPTER 5

Examining the Functional Integration of Multiple Types of RGCs in Mouse dLGN Thalamocortical Neurons

Attributions: This chapter is a work-in-progress manuscript drafted by EYL in consultation with Chinfei Chen. All experiments were designed in collaboration with Chinfei Chen. EYL performed all experiments and data analysis with the exception of technical assistance in the form of genotyping, perfusions, tissue preparation and dissection, immunohistochemistry and imaging of retina from Sally Curtiss and eye injections from Genelle Rankin. CART-Cre mice were generously provided by Hongkui Zeng at Allen Brain Institute. Constructs for viruses used in the dual channel experiment were generously provided by Minsuk Hyun and Bernardo Sabatini; these constructs were transformed and packaged into AAV2/2 by Chen Wang and BCH Viral Core. Foster Nichols V provided advice and programming expertise for producing response maps in Figure 5.3.

ABSTRACT

The organization of retinogeniculate connectivity has long been interpreted in the context of a framework of parallel pathways or labeled lines, according to which different types of visual information encoded in the firing patterns of diverse retinal ganglion cells (RGCs) are relayed to the cortex through independent retinogeniculate labeled lines. While this framework approximates the intricately layered structure of the primate visual system, similar organizational nuance has been difficult to demonstrate in the mouse visual system. In this study, I test whether different types of RGCs can functionally innervate common TC neurons. Optogenetic dissection of the retinogeniculate connectivity shows that genetically identified direction-selective (DS) RGCs do frequently converge with other RGCs onto the same neuron. However, they provide a strong or dominant input to ~30% of their target neuron population. This pattern persists past the last stage of retinogeniculate refinement. I therefore show that the parallel pathways framework does not adequately describe functional retinogeniculate connectivity in mice.

INTRODUCTION

The textbook view of mammalian visual processing describes the visual system as anatomically and functionally distinct parallel streams, channels of information, or labeled lines that flow from retina to the visual cortex through the dLGN (Livingstone & Hubel, 1988; Sherman & Guillery, 2001; Nassi & Callaway, 2009). These pathways carry different visual information encoded by different types of ganglion cells in the retina and recombine in the visual cortex to enable visual processing. Much of the evidence for these retino-geniculo-cortical pathways is based on decades of study in primate and cat visual systems focusing on the receptive field feature selectivity and physiological response properties of RGCs and dLGN neurons (Lennie, 1980; Kaplan & Shapley, 1982; Livingstone & Hubel, 1988; Mastronarde, 1992; Casagrande &

Xu, 2004; Van Hooser et al., 2005; Nassi & Callaway, 2009). However, evidence for clearly segregated parallel pathways in mice has been less clear (Krahe et al., 2011; Piscopo et al., 2013; Cruz-Martín et al., 2014; Dhande et al., 2015; Denman & Contreras, 2016; Morgan et al., 2016; Suresh et al., 2016; Sriram et al., 2016; Rompani et al., 2017; Stafford & Huberman, 2017). At the same time, the unprecedented genetic and imaging access to the mouse retina has revealed an unanticipated diversity of RGC types: well more than 30 have now been identified, and novel types are regularly added to the literature (although not all of these participate in the retinogeniculate visual pathway; Sanes & Masland, 2014; Sümbül et al., 2014; Dhande et al., 2015; Baden et al., 2016). It has been suggested that these different RGC types may each form a separate, functionally and anatomically segregated retinogeniculate labeled line, wherein RGCs of the same type converge together onto the same thalamocortical (TC) neurons that don't receive inputs from other RGC types. These single-source TC neurons then convey information about the feature of the visual scene detected by this RGC to the visual cortex, where multiple types of information eventually converge. Whether this scheme accurately describes the mouse retinogeniculate circuit, or whether different types of RGCs intermingle and converge on common TC neurons is a matter of active study and interest (Supplementary Figure 5.5; Cruz-Martín et al., 2014; Chen et al., 2016; Morgan et al., 2016; Rompani et al., 2017; Stafford & Huberman, 2017). This question is important, because the functional organization of retinal inputs can reveal how and where the visual system performs computations relevant for visual processing. The mouse visual system has become a useful tool for the study of visual processing, behavior, and development. Therefore, an accurate description of its functional connectivity will likely impact the broader understanding of vision and reveal a diversity of strategies that different species use to accomplish vision.

Two recent anatomical studies of connectivity have begun to challenge the idea of parallel retinogeniculate pathways in mice, though evidence of functional convergence of diverse RGC subtypes onto common TC neurons is still lacking (Morgan et al., 2016; Rompani

et al., 2017). Furthermore, the few strong and multiple weak RGC inputs that converge onto a TC neurons, as described in Chapter 4, prompt the question of whether diverse RGC types exhibit different patterns of connectivity in the dLGN.

In this chapter, I describe experiments that test whether more than one type of RGC can provide functional synaptic inputs to a common TC neuron. These experiments rely on an optogenetic *in vitro* approach to selectively activate the axons of DSRGCs in the dLGN. My results demonstrate that single mouse TC neurons often receive inputs from both On-Off Direction-Selective RGCS (OODSRGCs) and other unidentified RGCs, and thus suggest that neurons in the dLGN may integrate information from multiple parallel visual streams.

RESULTS

Experimental Strategy

The overlying hypothesis for this study posits that retinogeniculate functional organization can be demonstrated to conform to the framework of parallel visual pathways. To test this hypothesis, I initially chose to rely on the transgenic expression of ChR2 to selectively and reliably drive neurotransmitter release from one type of RGC. I aimed to compare the amplitude of blue light-driven EPSCs (“oEPSC”, corresponding to total input from one RGC type), to the expected or measured amplitude of overall synaptic input to a TC neuron. Geniculate lamination is less distinct in mice than in other species, but different RGC types do preferentially terminate their arbors in different regions of the dLGN (Kim et al., 2010; Cruz-Martín et al., 2014; Dhande et al., 2015). A labeled lines hypothesis predicts that if a TC neuron located in a dLGN region defined by the projections of a RGC type receives all or most of its inputs from this RGC type, then the synaptic response resulting from the activation of axons of this RGC type (through selective expression of ChR2, in this case) should be large enough to account for all or most of the inputs to that TC neuron (Supplementary Figure 5.5). Furthermore,

because RGC classification rests on the intersection of morphology, gene expression, retinal distribution and physiological properties, the RGC population may be subdivided in multiple different ways (Völgyi et al., 2009; Sanes & Masland, 2014; Baden et al., 2016b). OODSRGC direction selectivity clusters along cardinal axes in the retina, and these clusters each comprise a RGC subtype, whereas the OODSRGCs together comprise the overlying type. I therefore chose to test the labeled lines hypothesis in RGC-Cre lines that label overlapping RGC populations: BD-Cre-ER (“BD”) and CART-IRES2-Cre (“CART,” Cocaine- and Amphetamine-Regulated Transcript). BD-Cre-ER labels ON-OFF-Direction Selective RGCS (OODSRGCS) selective for ventral motion (Kay et al., 2011), whereas CART-Cre, in labeling CART-positive RGCs, identifies both BD-RGCs and OODSRGCs preferring other cardinal axes of motion (Kay et al., 2011; Sanes & Masland, 2014; Martersteck et al., 2017). In comparing the patterns of retinogeniculate connectivity between these RGC groupings, I aimed to test whether a subtype (BD) or broader type (CART) of RGC could form its own retinogeniculate labeled line through functional convergence onto distinct, dedicated neurons. This comparison can also indicate whether TC neurons receive convergent inputs from one subtype of OODSRGC or whether they integrate OODSRGCs preferring different directions of motion. Finally, because the retinogeniculate synapse exhibits robust developmental refinement which continues through P60 (Hong et al., 2014), I aimed to capture any effect of refinement on the functional segregation of RGC types within the LGN by comparing P30 and P60 age groups.

BD;ChR2 and CART;ChR2 retinæ drive ChR2 expression in OODSRGCs

Because Cre-driven expression can vary depending on the promoter and other characteristics of the reporter, I first tested whether the Ai32 ChR2(H134R) mouse, possessing a CAG promoter (Madisen et al., 2012), labels retinal populations in BD- and CART-Cre mice that are consistent with previous reports. As both BD and CART RGCs can be identified by the expression of CART (Kay et al., 2011), I performed immunohistochemistry for CART and Brn3A

(a marker of RGCs; Xiang et al., 1995) in *BD;ChR2* and *CART;ChR2* retinae. Preliminary results show that 91% of Brn3a⁺, YFP⁺ RGCs in *BD;ChR2* retinae (Figure 5.1A, F) and 95% of Brn3a⁺, YFP⁺ RGCs in *CART;ChR2* (Figure 5.1B, F) retinae express CART. Thus, both RGC-Cre lines exhibit a high degree of specificity of ChR2-YFP labeling. I also found that YFP⁺ axonal boutons in the dLGN of *CART;ChR2* animals exhibit a high degree of overlap with VGLUT2, a marker specific to retinogeniculate inputs (Figure 5.1C). Together these results provide confidence that blue-light activation in *BD;ChR2* or *CART;ChR2* slices will selectively drive retinogeniculate synaptic currents from BD⁺ or CART⁺ RGCs.

No effect of neonatal tamoxifen administration on retinogeniculate development

Cre-driven expression in BD-Cre-ER mice requires the administration of a large dose of tamoxifen (TX) neonatally (Kay et al., 2011). Because this dose can affect the overall health and development of the pups, I compared the electrical fiber fraction between mice receiving TX (*Chx10;ChR2* and *BD;ChR2* mice combined) and uninjected mice (*Chx10ChR2* data reproduced from Chapter 4). Neonatal TX administration did not alter the electrical fiber fraction at P30 or P60 (P30 no TX: n=23, median 0.07, IQR 0.14, TX: n=30, median 0.13, IQR 0.165; p=0.435 MW; P60 no TX n=29, median 0.18, IQR 0.21, TX n=25, median 0.16, IQR 0.23; p=0.3852 MW). I also took advantage of the HB9-GFP mouse line, which labels BD-RGCs in a non-Cre-dependent manner (Trenholm et al., 2011), to test the effect of TX on the density of RGCs. Neonatal TX injection had no effect on the number of GFP⁺ RGCs (p=0.71) in the retinae of Hb9-GFP mice. The administration of TX should therefore have no effect on the functional organization of retinogeniculate connectivity.

BD and CART RGCs drive a broad range of EPSC amplitudes

To begin to assess the functional organization of BD and CART RGC synapses in the dLGN, I prepared parasagittal slices from the brains of *BD;ChR2* and *CART;ChR2* mice. I

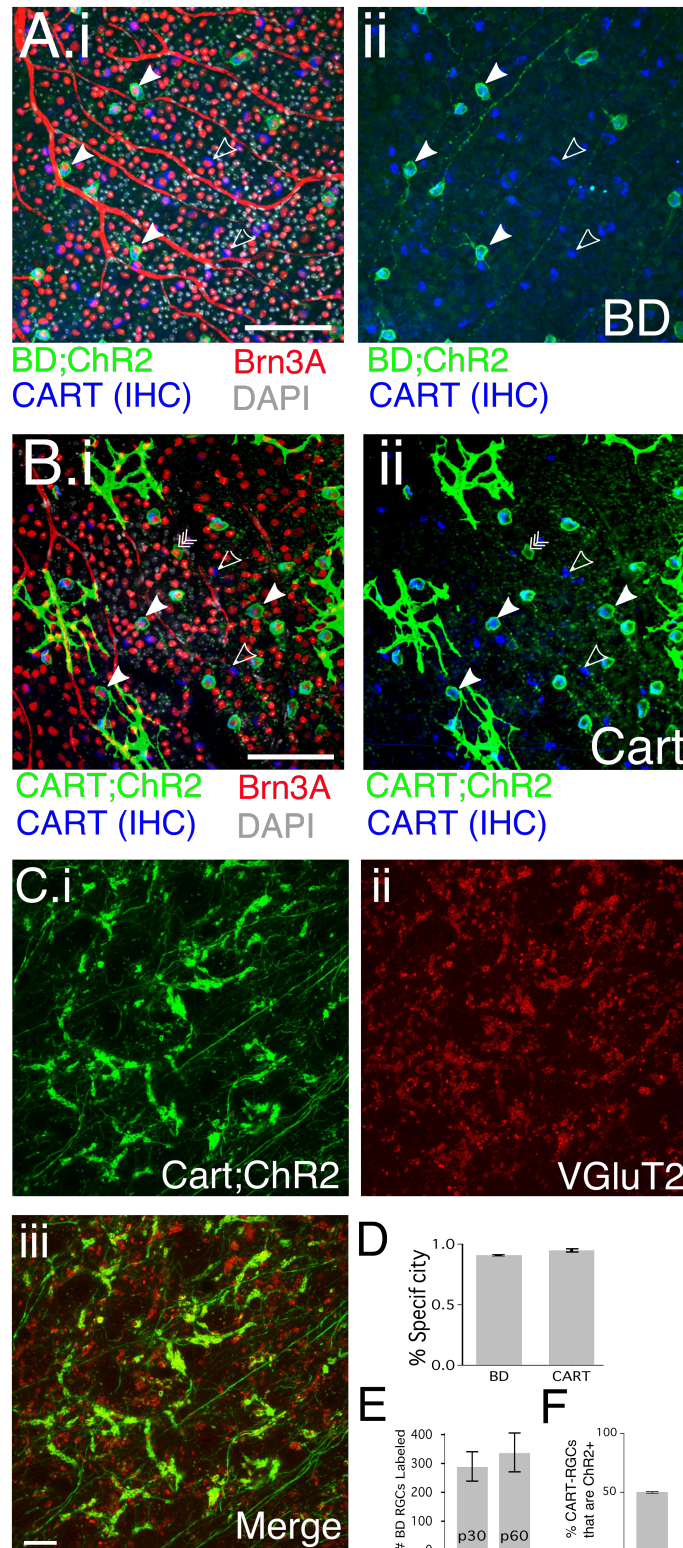


Figure 5.1: Preliminary Characterization of ChR2 expression in retinæ of *BD;ChR2* and *CART;ChR2* mice.

Figure 5.1 (Continued)

(A) Representative confocal stack of the RGC layer of a *BD;ChR2* mouse retina stained for GFP (ChR2; green), Brn3A (RGCs; red), CART (DS-RGCs, blue), and DAPI (nuclei, grey). (i). Composite of all four channels. (ii). Composite of GFP and CART-IHC signals to show overlap between these two signals. Filled arrowheads: quadruple-labeled RGCs; empty arrowheads: GFP⁺ CART⁺ RGCs. The same arrows are reproduced in both i and ii to track the subtler CART IHC signal. (B). Representative confocal stack of RGC layer of a *CART;ChR2* mouse retina stained as in A. Arrows as in A, with the addition of striped arrow that points to a GFP⁺ but CART⁻ RGC. Note, DAPI is very dim in A and B. A and B Scale bars=100 μ m (C). Confocal stack of dLGN in a *CART-Cre;ChR2* mouse stained for GFP(i) and VGLUT2(ii), with merged signals in iii. Scale bar = 20 μ m (D). Summary of preliminary quantification of labeling specificity of GFP expression in *BD* and *CART;ChR2* retinæ, referring to the number of GFP⁺, Brn3a⁺, CART-IHC⁺ RGCs ("GFP⁺ DS-RGCs") divided by the number of GFP⁺, Brn3a⁺ RGCs (all GFP⁺ RGCs). (E). Average total number of GFP⁺ neurons per retina in the RGC layer of *BD;ChR2* retinæ at P30 (n=8 animals) and P60 (n=10 animals). One retina per animal was quantified. (F). Preliminary quantification of the proportion of CART⁺, Brn3A⁺ RGCs that express ChR2 in *CART;ChR2* retinæ, from 3 retinæ P30 and older.

performed patch-clamp experiments in slices from P30 and P60 animals, using full-field blue light stimulation (as described in Chapter 4) to evoke maximal responses for BD or CART RGC axons (I refer to these as BD-oEPSCs and CART-oEPSCs).

Maximal BD-oEPSCs and CART-oEPSCs exhibited a broad range of amplitudes (Figure 5.2Ai, Bi). I roughly classified these populations of oEPSC amplitudes based on the 600-pA cutoff previously used to distinguish strong from weak retinal inputs (Chapter 4, Liu & Chen, 2008). The majority of responses had both an AMPAR and NMDAR component and ranged up to 600 pA in amplitude. 24-37% of the remaining inputs exceeded 600 pA (Figure 5.2Aii, Bii) and were thus likely to be strong drivers of TC neuron activity (Liu & Chen, 2008). An additional 3-24% of BD-oEPSCs and CART-oEPSCs were very small, characterized by the absence of a fast activating and decaying AMPAR component, with median peak NMDAR currents measuring 65 pA (IQR 69pA) and a peak AMPA:NMDA ratio of 0.19 (IQR 0.16). The median AMPA:NMDA Ratio for oEPSCs with a detectable AMPAR component was 1.26 (IQR 1.06). I did not perform the pharmacological experiments necessary to distinguish whether these slow currents may correspond to silent inputs lacking functional AMPA receptors (Chen & Regehr, 2000), spillover currents (Hauser et al., 2014), or weak distally synapsing inputs whose small AMPAR component cannot be recorded in the soma. These may be of interest for future study.

This cursory survey demonstrates that OODSRGC make variable contributions to the total retinal drive onto individual TC neurons.

Examining the spatial organization of OODSRGC synaptic connectivity

This wide range of BD- and CART-oEPSC amplitudes can be consistent with a labeled lines model. For example, since OODSRGCs restrict their axons to the outer shell region of the dLGN (Kay et al., 2011; Dhande & Huberman, 2014; Cruz-Martín et al., 2014), weaker synapses may reflect borderline regions or incomplete axon retraction from inappropriate target regions.

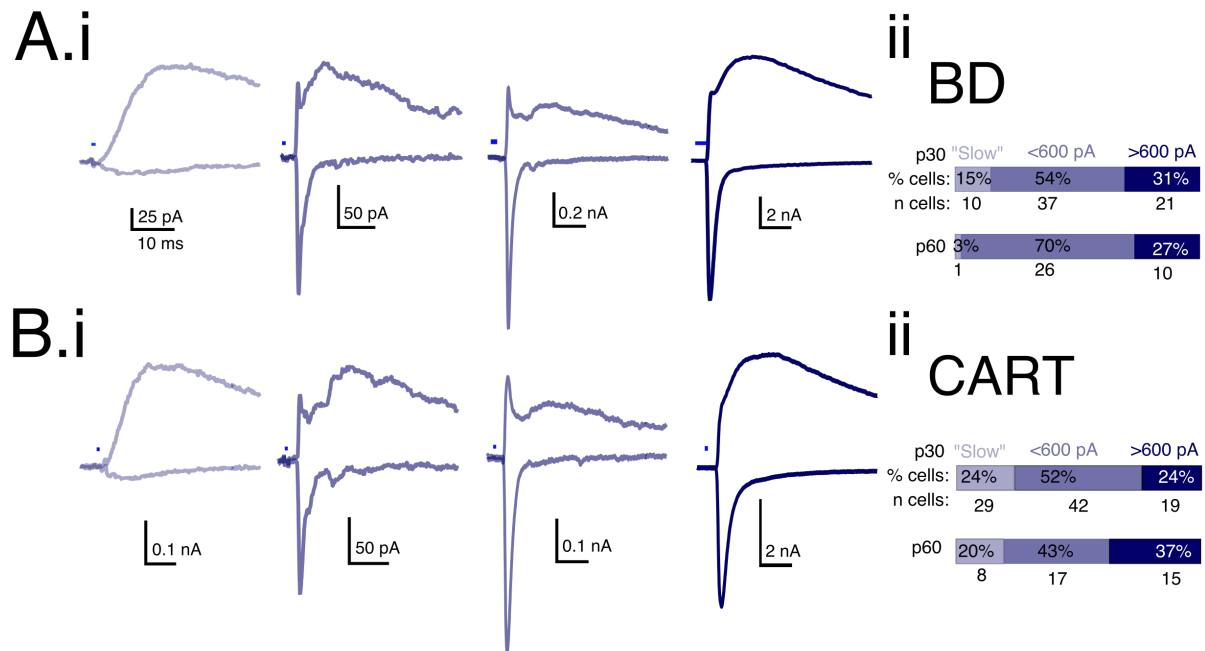


Figure 5.2: BD and CART RGCs drive geniculate responses with a broad range of amplitudes.

(A.i) Example maximal oEPSCs obtained using full-field blue light stimulation in dLGN slices prepared from *BD;ChR2* mice. The traces are shaded according to their categorization in the stacked bar graph on the right (ii), which summarizes the types of maximal oEPSCs encountered in the population, broken down by age. (B). Example maximal oEPSCs and their amplitude category breakdown (right) from *CART;ChR2* slices.

The distribution of BD-RGC axons also covers a portion of the core, but may not necessarily make functional synapses there (Hong & Chen, 2011; Kay et al., 2011; Hong et al., 2014; Dhande & Huberman, 2014*b*; Cruz-Martín et al., 2014). I therefore hypothesized that TC neurons with stronger BD or CART inputs may be restricted to the shell region of the dLGN, whereas weaker inputs may extend in a gradient into the core region.

I tested this hypothesis retroactively based on records of approximate locations of patched TC neurons with reference to a grid map (Figure 5.3A). My recordings were generally circumscribed to the mid-to-caudo-ventrolateral corner of the dLGN, where retinogeniculate axons are best preserved for effective electrical stimulation of the OT (Chen & Regehr, 2000). This region partly spans the shell and core regions (Hong et al., 2014).

Figure 5.3B shows reconstructions of the approximate locations of TC neurons that exhibited oEPSCs, color-coded by AMPAR oEPSC amplitude. Figure 5.3C adds to this map the locations of TC neurons that exhibited no oEPSC. Interestingly, in contradiction to my hypothesis, I did not find any apparent gradient or pattern in the distribution of subtype input amplitudes between the shell versus the core region of this caudoventral portion of the dLGN; TC neurons with no CART or BD input closely neighbor those with a substantial oEPSCs. These data therefore suggest that functional connectivity of OODSRGC does not exhibit a clear laminar or columnar organization within the region occupied by its axons. However, the method used here is unlikely to reveal nuanced connectivity patterns. It would be interesting to examine this question by expanding the TC neuron sampling to the entire dLGN and more precisely tracking the exact location of recorded neurons, as the caudal portion of the dLGN exhibits an especially dense proportion of direction-selective TC neurons (Piscopo et al., 2013).

OODSRGCs account for a small fraction of total retinal drive to most TC neurons

The labeled lines model predicts that, if I could label the entire population of BD or CART RGCs with ChR2, a concentration of TC neurons should exhibit very large oEPSCs—meaning

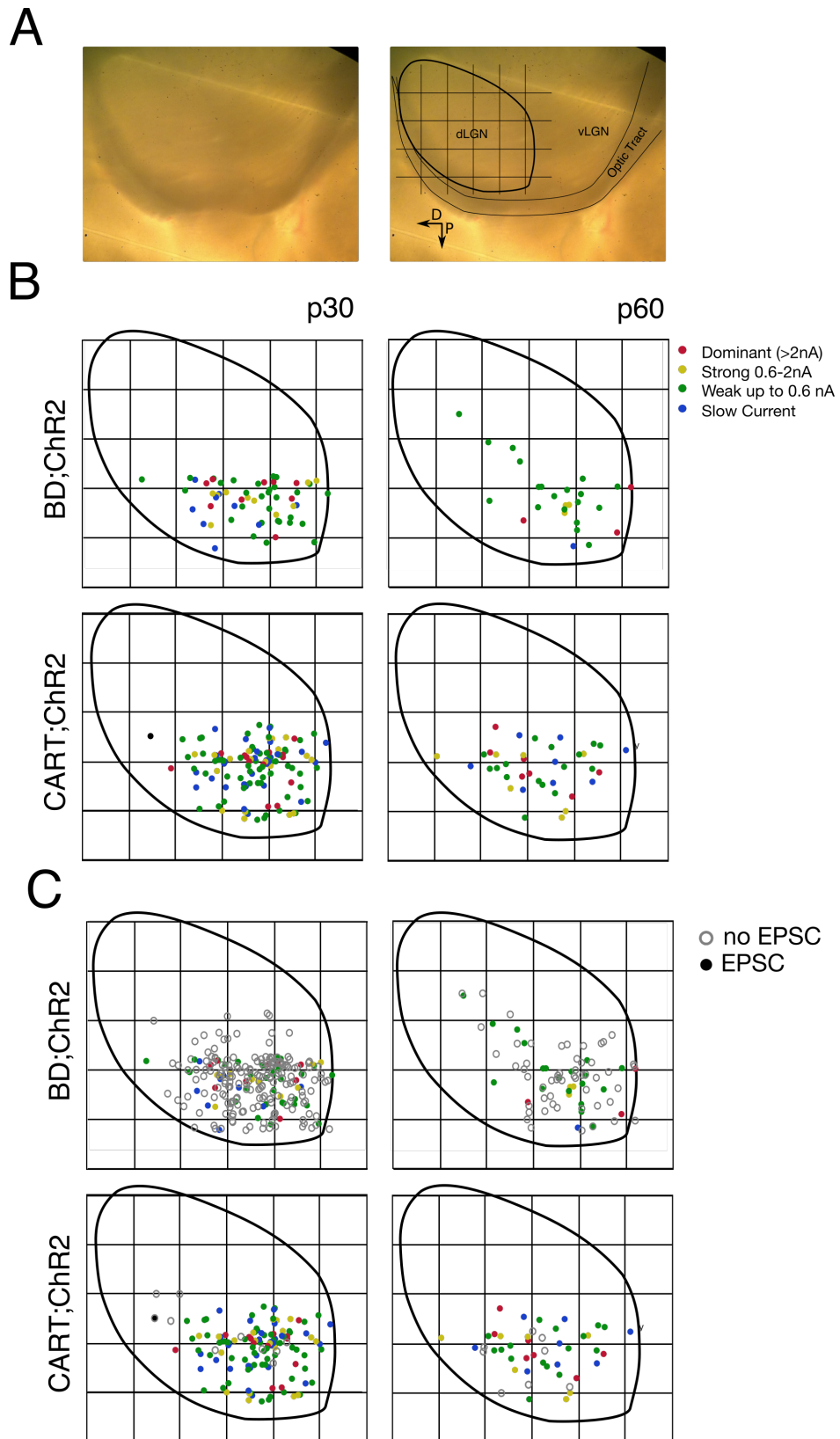


Figure 5.3: Spatial Distribution of BD and CART oEPSCs in dLGN.

Figure 5.3 (Continued)

(A). Left: image of dLGN slice during an *in vitro* experiment. Right: same image with a superimposed grid used to track the approximate location of responding neurons. (B). Spatial distribution of oEPSCs across the dLGN by age and RGC type (left: P30, right: P60; top: *BD;ChR2*, bottom: *CART;ChR2*). Circles are color coded by oEPSC (AMPA) amplitude category as listed in the legend. (C). Superimposed on top of figures in B are locations of TC neurons that did not exhibit an oEPSC in response to maximal blue light stimulation (gray circles).

that they receive all or most of their input from these RGCs. The distribution of input amplitudes I encountered (Figure 5.2) and their lack of apparent spatial clustering (Figure 5.3) both contradict aspects of this model. However, a low efficiency of RGC labeling could explain these findings. Small oEPSCs that are proportional to the number of RGC labeled in the dLGN, might serve as indirect evidence of functional segregation of RGC types. I therefore quantified the proportion of BD and CART-RGCs labeled in each mouse line.

An average of almost 300 RGCs per retina expressed ChR2 in *BD;ChR2* retinæ at P30 and P60 (Figure 5.1G). The expected total population likely consists of at least 1500 BD-RGCs (assuming that BD-RGCs are a quarter/one of four direction-preferring clusters of all CART⁺ OODSRGCS RGCs, which themselves constitute about ~15% of the 40-60,000 RGCs/mouse retina; Jeon et al., 1998; Kay et al., 2011; Schlamp et al., 2013; Farrow et al., 2014). HB9GFP retinæ contain about 900 GFP⁺ BD-RGCs, which does not appear to cover the entire BD-RGC population (data not shown)—thus, most generously, we’ve labeled an average of ~20-30% of all BD-RGCs. The preliminary quantification for three *CART;ChR2* retinæ shows both denser labeling and lower variability. YFP⁺ RGCs in *CART;ChR2* mice label about 50% of all CART⁺/Brn3A⁺ RGCs by a preliminary estimate (Figure 5.1H).

These findings predict that, if convergence of BD or CART RGCs functionally segregates from other RGC types in dLGN, oEPSCs in TC neurons in *BD;ChR2* and *CART;ChR2* mice should make up at least 20% (BD) and 50% (CART) of total retinal input, respectively (assuming that a random proportion is labeled). I can use the maximal eEPSC as an indicator of total input to the cell: as I showed in Chapter 4, electrical stimulation of the OT misses about 40% of total input to the cell. This comparison sets a low bar to satisfy the hypothesis. Figure 5.4 compares the amplitude of oEPSCs and eEPSCs from the same cells. While there was a small subset of cells (<20%, Table 5.1) for which the oEPSC was equal to or greater than the eEPSC, the majority of neurons had a much smaller oEPSC: the median oEPSC was <5% of the eEPSC in *BD;ChR2* slices and <7% for *CART;ChR2* slices (Table 5.2). Expanding this population to

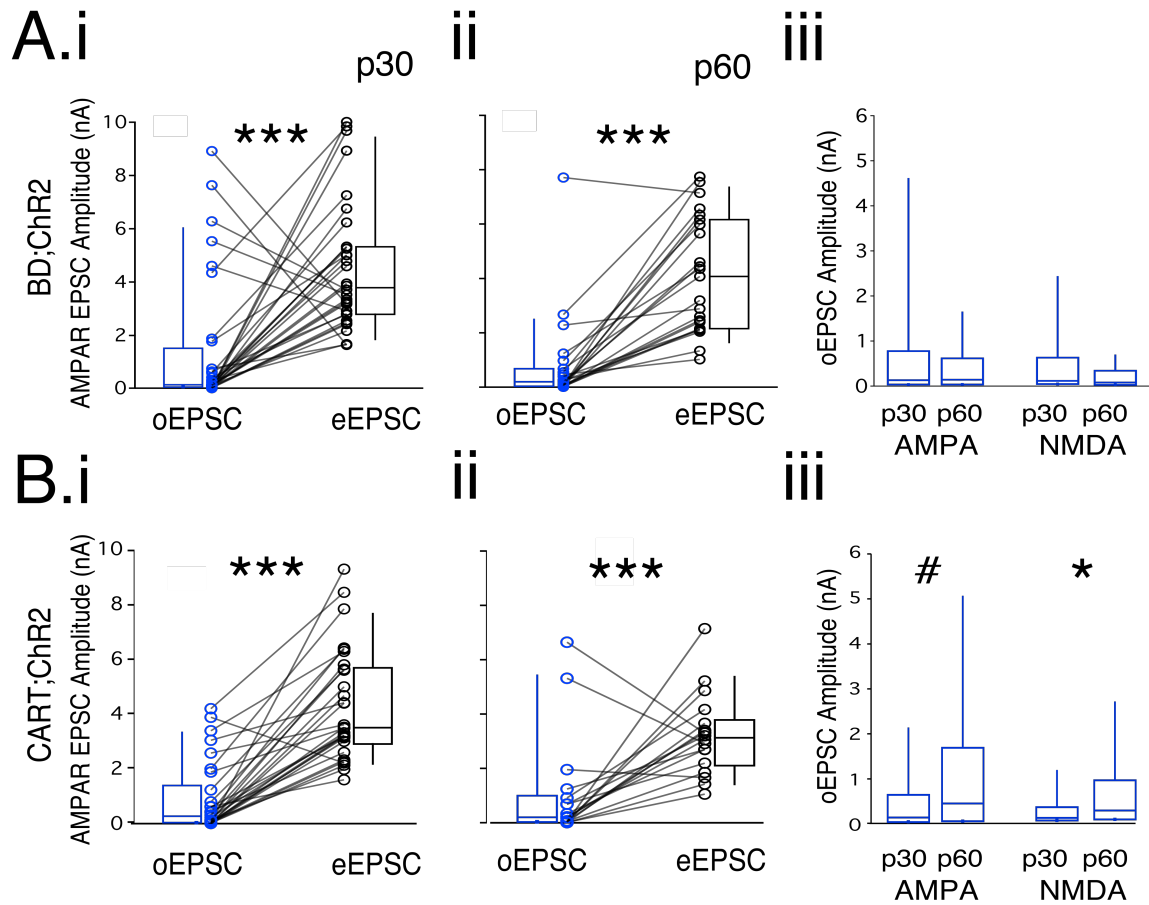


Figure 5.4: *BD;ChR2* and *CART;ChR2* oEPSCs are much smaller than eEPSCs in the same TC neurons.

(A). *BD;ChR2* oEPSCs and eEPSCs (bulk RGC stimulation) at 30 (i) and P60 (ii). i and iii (P30 and P60 data) show pairs of data points and box plots summaries for cells that had both a *BD;ChR2* oEPSC and an eEPSC from the electrical stimulation of the OT. *** $p < 0.0001$ Wilcoxon. iii: comparison of *BD;ChR2* AMPAR and NMDA oEPSCs at P30 and P60; these plots include additional cells for which the eEPSC was not collected. Comparing between age groups, AMPA $p = 0.1787$, NMDA $p = 0.0983$ MW. Further statistics for these figures are presented in Table 5.3. (B). *CART;ChR2* oEPSCs and eEPSCs. Panels arranged as in A. # $p = 0.0892$, * $p = 0.0135$.

Table 5.1: Summary of data presented in Figs 5.4A, B, and Supplementary Figure 7.6 H-I.

RGC type	Age	N TC neurons	Percent of Total with an oEPSC/eEPSC ratio of:		
			<0.5	0.5-0.95	>0.95
BD	p30	32	84.4	0.0	15.6
BD	p60	23	91.3	4.3	4.3
CART	p30	30	83.3	13.3	3.3
CART	p60	18	83.3	0.0	16.7
J	p30	5	80.0	20.0	0.0
J	p60	5	80.0	20.0	0.0

Table 5.2: Summary of the comparison of the amplitude of oEPSC to the eEPSC from the same cell, referring to data presented in Figure 5.4A, B, Supplementary Figure 7.6H-I.

RGC type	Age	N TC neurons	oEPSC/eEPSC * 100		AMPA eEPSC (nA)	
			Median	IQR	Median	IQR
BD	p30	32	4.9	40.3	3.8	2.7
BD	p60	23	4.5	19.1	4.1	4.0
CART	p30	30	6.7	27.4	3.5	2.8
CART	p60	18	6.4	33.9	3.1	1.7
J	p30	5	3.7	42.2	4.0	2.6
J	p60	5	32.4	48.1	1.8	1.3

include those cells for which I did not measure the eEPSC yields median oEPSC amplitudes <200 pA (Table 5.3), in contrast to the several nA of current TC neurons generally receive, as shown in Chapter 4. These results therefore show that synaptic input from BD or CART RGCs is generally much weaker than predicted based on the proportion of the population labeled in the retina.

To further formalize this comparison, I plotted the cumulative probability distributions of the amplitudes of BD-oEPSCs and CART-oEPSCs against corresponding maximal eEPSC and *Chx10;ChR2* P30 maximals (data from Chapter 4, Figure 4.6). *Chx10;ChR2* maximal oEPSCs and eEPSCs from OT stimulation capture different proportions of the same axonal population (Chapter 4). If the small amplitude of BD-oEPSCs and CART-oEPSCs reflects very suboptimal activation of a larger homogenous population—if only a very small percent of all BD⁺ or CART⁺ inputs to every cell have been labeled with ChR2—I would expect a similarly shaped curve to that of Chx10, only shifted further to the left (reflecting lower amplitude). The raw and normalized data are plotted in Figure 5.5, statistics in Table 5.4. Strikingly, while the data do exhibit the expected leftward shift, the *BD;ChR2* and *CART;ChR2* data exhibit a distinct nonlinear shape. There is also no significant difference in the amplitude of BD-oEPSCs and CART-oEPSCs (whether I include “slow currents”, as shown in Table 5.3, or only consider oEPSCs with an AMPAR component) despite the differences in the proportion of RGCs labeled in their retinae. These results suggest that the overall low amplitude of BD- and CART-oEPSCs are unlikely to simply reflect inefficient labeling of otherwise homogenous converging RGCs. Instead, these indicate that TC neurons that receive an OODSRGC input also integrate other inputs from other RGC subtypes.

Evidence of Divergence among OODSRGCS Preferring Different Directions

Because BD-RGCs represent a subset of CART-RGCs, these data can also reveal whether OODSRGCs that preferentially respond to different directions of motion converge onto

Table 5.3: Summary of the oEPSC amplitudes presented in Figure 5.4A, B, Supplementary Figure 7.6J.

RGC type	Age	N TC neurons	oEPSC AMPA (nA)		oEPSC NMDA (nA)	
			Median	IQR	Median	IQR
BD	p30	68	0.131	0.740	0.118	0.565
BD	p60	37	0.142	0.579	0.080	0.313
CART	p30	81	0.068	0.464	0.125	0.299
CART	p60	40	0.174	1.130	0.300	1.438
J	p30	28	0.071	0.328	0.054	0.161
J	p60	31	0.407	0.554	0.228	0.268

the same neurons or prefer separate target populations. Several studies of direction and orientation selectivity in the mouse dLGN have proposed that geniculate orientation selectivity may arise at least in part from the combination of DSRGCs with opposing motion preferences (Marshel et al., 2012; Piscopo et al., 2013; Zhao et al., 2013; Stafford & Huberman, 2017). If diverse OODSRGCs frequently converge onto the same neurons, I would expect to encounter larger CART-oEPSC than BD-oEPSC amplitudes among target TC neurons, representing an OODSRGCs channel of information that perhaps computes orientation selectivity or stimulus motion. On the other hand, if OODSRGCs with different direction preferences don't converge, I would instead expect more TC neurons with a CART-oEPSC than a BD-oEPSC, corresponding to the broader population labeled in the retina. Figure 5.6 reveals a dramatic increase in the number of TC neurons with a CART-oEPSC relative to BD. Combined with the similarity in BD-oEPSC and CART-oEPSC amplitudes, these data suggests that OODSRGCs preferring different directions of motion rarely converge.

I note here that all these experiments were also performed using a third RGC-Cre mouse to test whether the retinogeniculate connectivity of distinct RGC subtypes is organized differently. I used the JamB-Cre-ER mice, which label the morphologically distinctive J-RGCs when crossed with a Thy1 promoter-based reporter line. These RGCs are sensitive to upward motion within a narrow set of parameters and exhibit color opponency (Kim et al., 2008; Joesch & Meister, 2016). Crossing these mice with the CAG-promoter-based Ai32 (ChR2) mice lead to extensive non-RGC-layer neuronal and non-neuronal YFP expression which have made it challenging to directly assess the specificity and density of labeling among RGCs. The data are included in the Appendix (Supplementary Figure 7.6), Figure 5.8, and Tables 5.1-4, and generally follow a similar pattern as the OODSRGC data, with the caveat that additional characterization may or may not identify J-RGC as the predominant RGC type labeled J;ChR2 retinae.

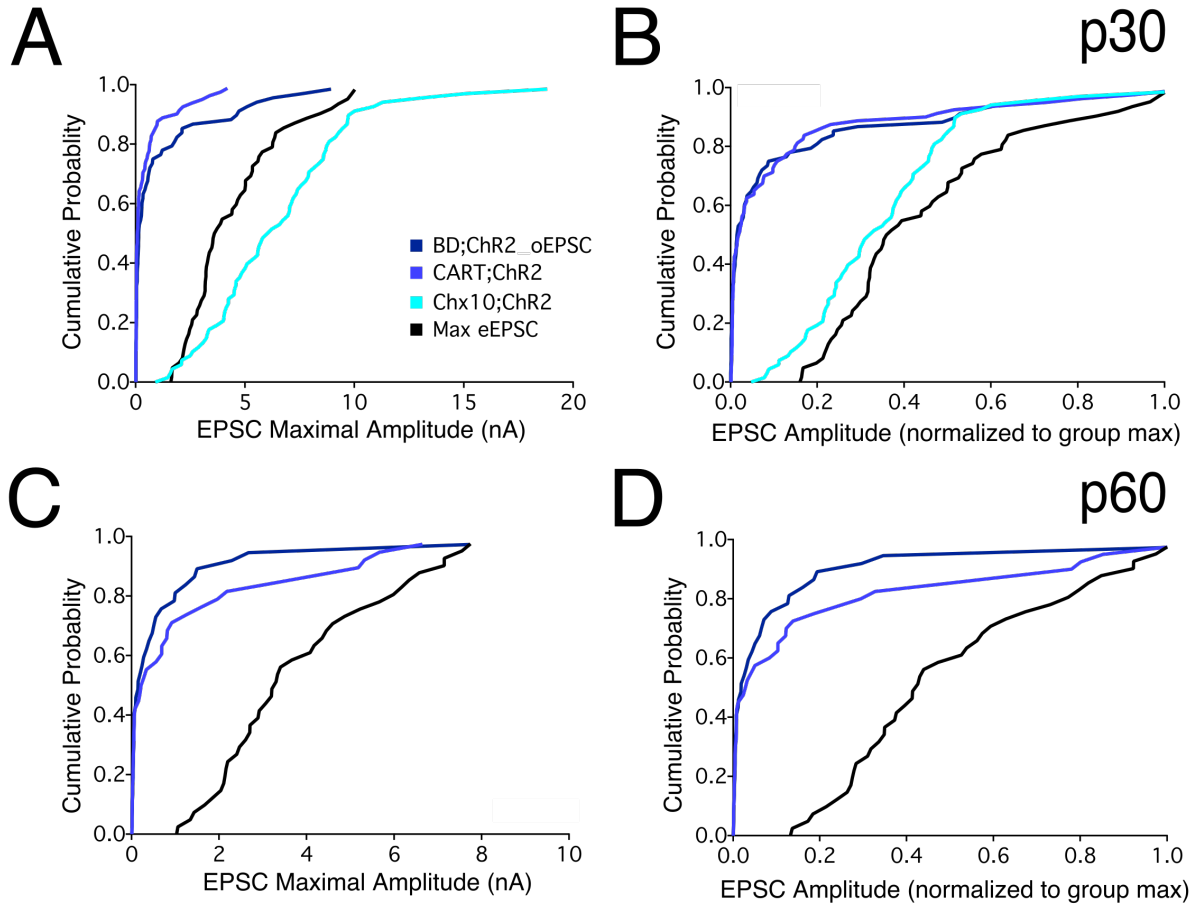


Figure 5.5: *BD;ChR2* oEPSCs and *CART;ChR2* oEPSCs are much smaller than total retinal input onto TC neurons.

(A, B). Cumulative probability distribution plots of absolute (A) and normalized (B; to the maximal EPSC within each group) oEPSC and eEPSC amplitudes at P30. Legend in A applies to the entire figure. *Chx10;ChR2* data is reproduced from Chapter 4. Max eEPSC data accumulates the eEPSC from Figure 5.4. (C, D.) Cumulative probability distribution plots of absolute (A) and normalized (B; to the maximal EPSC within each group) oEPSC and eEPSC amplitudes at P60. Statistics are presented in Table 5.4

Table 5.4. Summary of Statistics for the comparison of oEPSCs and eEPSCs in Figure 5.5.

Raw data				Normalized			
AMPA p30	BD	CART	Chx10	AMPA p30	BD	CART	Chx10
BD				BD			
CART	0.79			CART	1		
Chx10	<0.0001	<0.0001		Chx10	<0.0001	<0.0001	
eEPSC	<0.0001	<0.0001	0.29	eEPSC	<0.0001	<0.0001	1
NMDA p30	BD	CART	Chx10	NMDA p30	BD	CART	Chx10
BD				BD			
CART	1			CART	1		
Chx10	<0.0001	<0.0001		Chx10	<0.0001	<0.0001	
eEPSC	<0.0001	<0.0001	0.34	eEPSC	<0.0001	<0.0001	0.38
AMPA p60	BD	CART		AMPA p60	BD	CART	
BD				BD			
CART	1			CART	1		
eEPSC	<0.0001	<0.0001		eEPSC	<0.0001	<0.0001	
NMDA p60	BD	CART		NMDA p60	BD	CART	
BD				BD			
CART	0.0195			CART	0.118		
eEPSC	<0.0001	<0.0001		eEPSC	<0.0001	<0.0001	

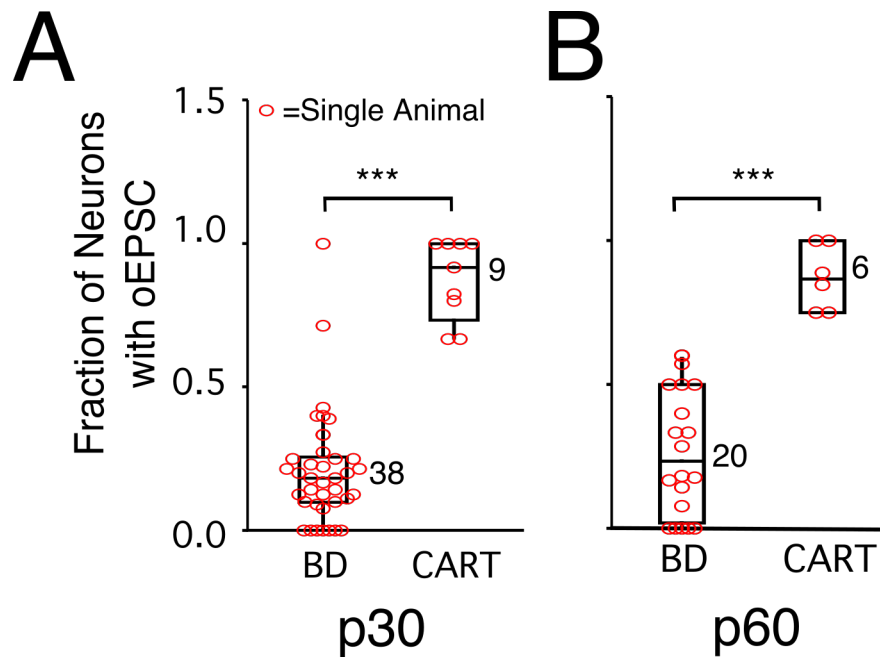


Figure 5.6: More TC neurons receive *CART;ChR2* inputs than *BD;ChR2* inputs.

Box plots and superimposed single data points show the proportion of patched TC neurons in each animal that exhibited an oEPSC. A: P30 data, B: P60 data. Numbers next to box plots list n of animals used for these experiments. BD data includes those animals in which no TC neurons exhibited an eEPSC, but more than 50 RGCs were labeled in the retina. Experiments with fewer than 50 ChR2⁺ BD-RGCs were excluded, as oEPSCs were never encountered in slices from these animals.

Multiple RGC types converge onto the same TC neurons

The experiments I have shown so far do not support a retinogeniculate connectivity scheme consistent with a labeled lines/parallel pathways organization. However, the low efficiency of OODSRGC labeling in examined retinae undermines a strong claim, because any axon that doesn't respond to blue light stimulation may still be an unlabeled BD or CART-RGC axon.

I was also unsatisfied with the inferential nature of this data, and devised an alternate experiment to directly assess whether different RGC types may synapse on common TC neurons. Specifically, I could use the CART-Cre line to express a Cre-dependent opsin in OODSRGCs and a different opsin sensitive to a different wavelength of light in RGCs that don't express Cre. I could then test whether individual TC neurons receive inputs from OODSRGC and non-DSRGCs by selectively activating each opsin. The BD-Cre-ER line is unsuitable for this experiment because Cre expression is inefficient and depends on neonatal tamoxifen administration. I combined dual-channel optogenetic stimulation (Lin et al., 2013; Hooks et al., 2015) with the Cre-off expression system (Saunders et al., 2012) to drive ReachR expression in CART-Cre-RGCs and ChR2 expression in non-CART RGCs. ReachR is a red-shifted opsin that responds to both blue and orange light (Lin et al., 2013), whereas ChR2 only responds to blue light (Lin et al., 2009). Therefore, orange light stimulation in the retinogeniculate prep will activate RGC axons from CART-RGCs, whereas blue light stimulation will activate both CART-RGCs and other RGCs that express ChR2.

To drive expression, AAV2/2 viral constructs carrying DIO-ReachR-mCitrine and DO-ChR2-mCherry were injected into the eyes of p20 CART-Cre mice. I then waited 52-54 days to allow ChR2 expression to turn off in CART-Cre⁺ RGCs. Figure 5.7A shows an example retina from a CART-Cre mouse injected with both viruses; <1% (2/233 counted RGCs) of labeled RGCs expressed both opsins across two retinae, and in one of these retinae stained for CART, 92% (56/61) of ReachR:mCitrine RGCs were immunopositive for CART, while only 4% (3/67) of

ChR2:mCherry neurons were. These two opsins can therefore reliably distinguish CART (CART:ReachR oEPSCs) and non-CART oEPSCs.

Here I present preliminary data from 3 animals. Of 32 TC neurons patch-clamped across 3 slices, 26 exhibited oEPSCs to both orange and blue light, 3 had only a blue light response, and 3 responded to neither wavelength. Example responses to orange and blue light stimulations from the same cell are shown in 5.7B, and the amplitudes of pairs of oEPSCs are plotted in 5.7C. Responses to blue light stimulation were consistently and dramatically larger (by a median factor of 7.1, IQR 24.9) than the CART:ReachR oEPSCs. This result is consistent with the single-opsin experiments, but demonstrate directly the convergence of CART⁺ and CART⁻ RGCs onto the same TC neurons. In a small subset of neurons, I used the inactivation of ReachR⁺ by prolonged orange light exposure (Hooks et al., 2015) to reveal the contribution of ChR2-expressing RGCs to the total blue light oEPSC (Figure 5.7D-F). Finally, while considering that virally expressed opsins can distort presynaptic release probability and the amplitude of oEPSCs (Jackman et al., 2014), I compared the cumulative probability distributions of CART:ReachR oEPSCs and blue light oEPSCs against P60 *CART;ChR2* oEPSCs and eEPSCs data shown in Figs 5.5C, D. The blue light oEPSCs were smaller than the eEPSCs ($p < 0.0001$ for AMPAR, < 0.05 for NMDA EPSCs), but the distribution of their amplitudes was similar ($p > 0.34$) to the distribution of the eEPSCs, whereas the amplitude and distribution shape of the CART:ReachR oEPSCs was similar to *CART;ChR2* (Cre-on amplitude trend smaller, with $p < 0.05$ in NMDA; comparison of normalized *CART;ChR2* vs. CART:ReachR yields $p > 0.35$). Notably, in two instances a large CART:ReachR oEPSC equaled or exceeded the blue light oEPSC. These results are in line with lower efficiency of activation of ReachR by blue than orange light (Lin et al., 2013), and with the observations that a small fraction of TC neurons receive large *CART;ChR2* and *BD;ChR2* contributions.

Though preliminary, this experiment provides direct evidence that a large number of TC neurons in the OODSRGC-recipient region of the dLGN receive converging input from both

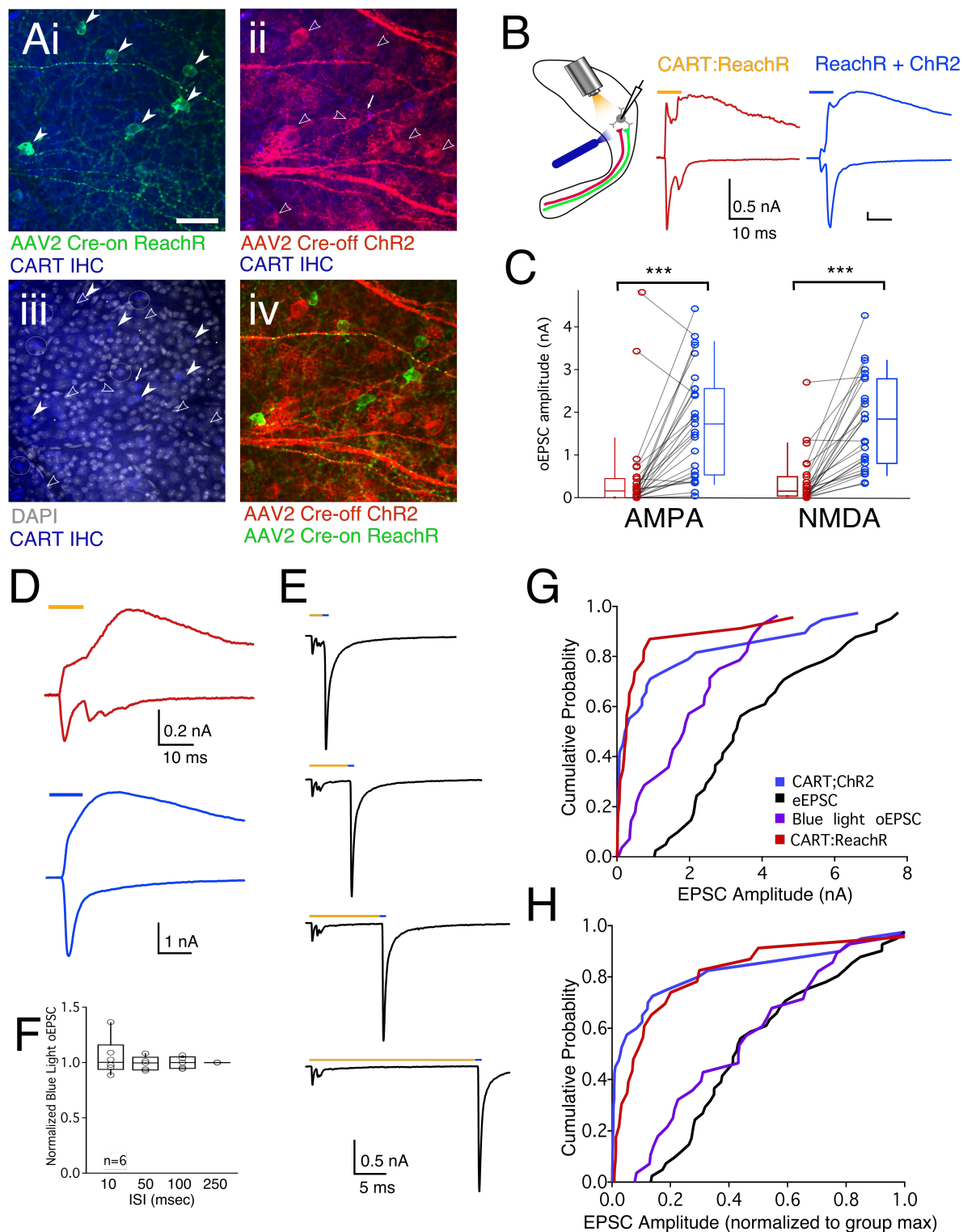


Figure 5.7: Dual channel RGC activation demonstrates convergence of multiple RGC types onto single TC neurons.

Figure 5.7 (Continued)

(A). Different channels of a spinning disk confocal image of a CART-Cre retina fixed at 53 days after injection with AAV2/2 viruses carrying Cre-on-ReachR and Cre-off-ChR2 constructs. ReachR-mCitrine (green) and CART immunohistochemistry (blue) signals are superimposed in i; ChR2-mCherry (red) and CART immunohistochemistry (blue) signals are superimposed in ii to show little overlap; iii shows CART and DAPI colocalization, with arrows from i and ii superimposed to identify mCitrine and mCherry-positive RGCs; (iv). shows lack of colocalization between neurons in RGC layer expressing ReachR-mCitrine (green) and ChR2-mCherry (red). Filled arrowheads: ReachR-mCitrine RGC layer neurons co-labelled with the CART antibody. Empty arrowheads: ChR2-mCherry RGC layer neurons with no CART expression. Circles: CART+ neurons with no opsin expression. Thin arrow points to a rare Cre-off-mCherry RGC that does express CART. Scale bar=50 μ M. (B). (*left*) Experimental setup—orange light (565nm LED) was delivered through the 60x objective and blue light was delivered through a 200 μ m-thick optic fiber with the center of the light spot positioned over the cell body of the patched TC neuron. (*middle, right*) Responses to 10msec-long red or blue light pulses recorded from the same neuron. (C). Comparison of the peak amplitude of AMPAR and NMDAR oEPSC responses to orange light (red box plots/data points) and blue light (blue box plots/data points) from the same TC neurons. $P < 0.0001$ matched Wilcoxon. (D). Another example of red and blue light-evoked oEPSCs recorded from the same cell; these form the baseline currents for the experiment shown in E. (E). Red-light-dependent inactivation of ReachR-expressing axons reveals the ChR2 oEPSC in response to blue light. (F). Summary quantification from 5-6 cells (2 of the cells did not include all time-points) of the blue light oEPSC after 10-250 msec long red light stimulus, normalized to the 250-msec blue light oEPSC. (G, H). Cumulative probability distribution plots of absolute (G) and normalized (H; to the maximal EPSC within each group) blue and red light evoked AMPAR oEPSCs (purple and red traces, respectively), compared to P60 AMPAR *CART;ChR2* oEPSC (blue trace) and eEPSC (black trace) amplitude distributions shown in Figure 5. G: Kruskal Wallis with Dunn post hoc yields $p < 0.001$ - $p < 0.05$ for all comparisons except *CART;ChR2* to CART-ReachR, which is n.s. H: Kruskal Wallis with Dunn posthoc yields $p < 0.001$ for all comparisons except *CART;ChR2* to CART-ReachR, and eEPSC to blue light oEPSC, which are n.s.

CART⁺ and CART⁻ RGCs. It also reveals that a small number of TC neurons do receive substantial convergent input from CART-RGCs alone.

Multiple RGCs of one type contribute to the subtype maximal oEPSC

In Chapter 4 I showed that TC neurons receive approximate 3 strong and 7 weak inputs from the retina. This finding may be reconciled with the parallel pathways framework through the argument that only the strong RGC inputs profoundly shape TC neuron spiking, whereas weak inputs have little functional relevance. I therefore hypothesized that any TC neuron may only receive strong or weak inputs from one type of RGC. Though my studies with specific Cre lines focused mainly on maximal oEPSC currents, in some recordings I was able to maintain the cell long enough to use methods presented in Chapter 4 to test whether the oEPSC was composed of multiple single fiber inputs. At least one ChR2-positive single fiber was isolated in 23 cells. A summary of one such experiment is shown in Figure 5.8A-B, and group data is plotted in Figure 5.8D. The distribution of single fiber input amplitudes from *BD;ChR2*, *CART;ChR2*, and *J;ChR2* combined show that these RGC types make a broad range of single fiber contacts that match the distribution of undifferentiated single fibers isolated optically from *Chx10;ChR2* mice (Figure 5.8C). TC neurons exhibit a broad range of “subtype fiber fractions”—the ratio of the amplitude of a single fiber input expressing ChR2 to the amplitude to the maximal oEPSC representing the sum of all ChR2-expressing inputs (Figure 5.8D). Most cells with a strong or dominant oEPSC exhibit a small subtype fiber fraction, indicating that at least 1 weak input contributes to the maximal oEPSC. Therefore, this experiments preliminarily indicates that both weak and strong inputs from one RGC type can converge onto common TC neurons. Together with the preceding findings, I observe that these multiple inputs of the same subtype may converge together with RGC inputs of different subtypes—but further experiments are needed to characterize such patterns in detail and over development.

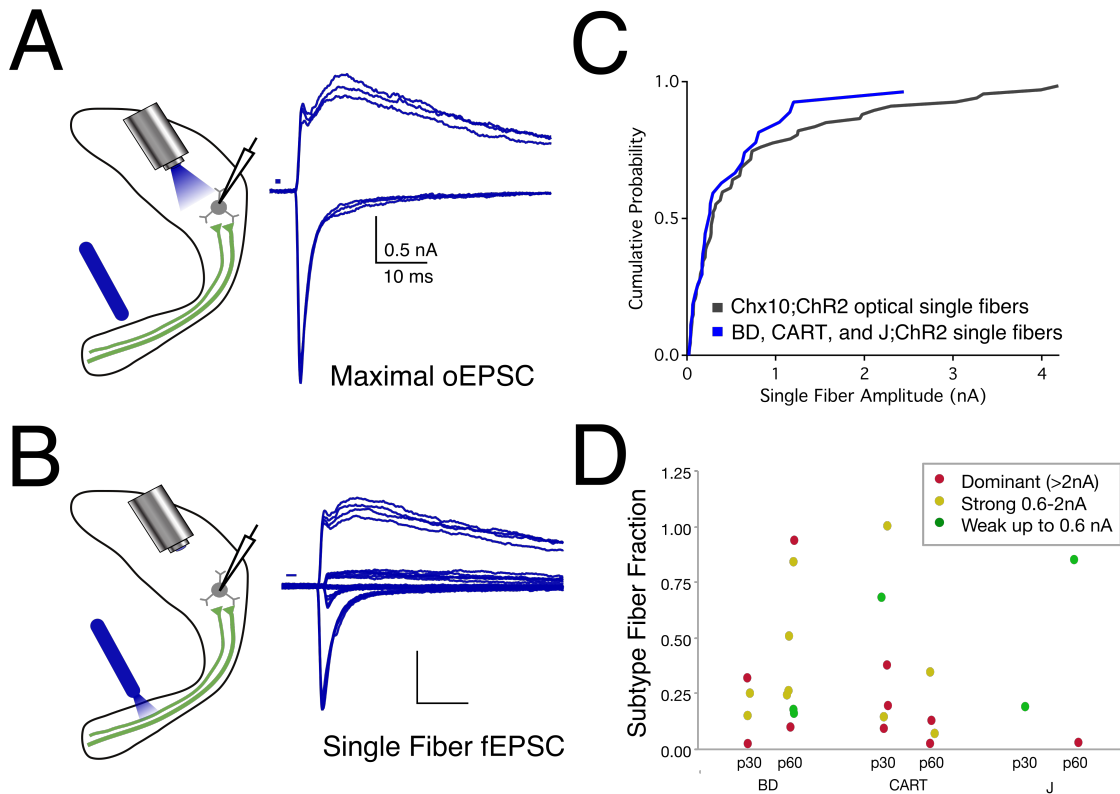


Figure 5.8: Multiple RGCs of the same type contribute to the subtype maximal oEPSC.

(A). Full-field stimulation of a maximal oEPSC in a P30 *CART;ChR2* retinogeniculate slice, with multiple traces shown for clarity. (B). Single fibers from the same cell as in A were isolated using minimal stimulation of the OT with a optic fiber light source. Traces superimpose recordings from a large range of blue light intensities. Traces have been manually realigned for clarity. (C). Cumulative Probability plot comparing the distribution of amplitudes of Chx10ChR2 fibers reproduced from Chapter 4 to the combined single fibers isolated from BD;ChR2, *CART;ChR2*, and *J;ChR2* slices. These distributions are statistically comparable. (D). A plot of the available data for the optical (RGC subtype) fiber fraction (single fiber fEPSC/maximal oEPSC). Points are color-coded by the amplitude category of the maximal oEPSC.

Minor changes to subtype connectivity during late-stage developmental refinement

I have previously shown that the final stage of developmental refinement extends to P60 at the mouse retinogeniculate synapse (Hong et al., 2014/Chapter 3). I therefore hypothesized that the large number of weak contacts at P30 could reflect an unfinished process of developmental refinement. P30 and P60 data have been presented side by side throughout this study. This comparison revealed only minor changes between these two ages—notably a modest increase in CART-oEPSCs and J-oEPSCs (Figs 5.4, Supplementary Figure 7.7). Because preliminary paired-pulse experiments in *Chx10;ChR2* P60 animals showed a greater distortion of the probability of release with ChR2 stimulation (data not shown) than at P30, I cannot rule out the role of experimental artifact in this increase. On the whole, therefore, it appears that the connectivity patterns I observed at P30 are maintained into maturity, after the final stage of refinement.

DISCUSSION

In this study I have used optogenetic labeling of OODSRGCs (and J-RGCs) to show that TC neurons can receive inputs from multiple types of RGCs. While the majority of these subtype contributions are weak (<600pA EPSC), approximately a third may robustly drive postsynaptic activity, and a small population of TC neurons exhibit sufficiently large oEPSCs to account for all or nearly all their retinal inputs. These results suggest that the parallel pathways organizing framework is not the only, nor perhaps the dominant mode of retinogeniculate functional connectivity in mice.

Reevaluating the Parallel Pathways Framework

These experiments do not rule out the idea of segregated retino-geniculo-cortical

pathways. First, the rare neurons with very large OODSRGC-oEPSCs may indeed bespeak such organization coexisting with other connectivity modes. Second, these results may be specific to the types of RGCs, geniculate neurons, or region of the dLGN that I have been able to examine. Further studies are needed to determine whether distinct TC neuron types may exhibit different patterns of retinogeniculate convergence in mice as they have been shown to do in the cat dLGN (reviewed in Weyand, 2016). Notably, I saw no correlation between oEPSC amplitude and cell capacitance (data not shown), but this measure is unlikely to capture subtle morphological diversity among TC neurons. Finally, the idea of parallel pathways may describe a higher-level organizing principle—after all, in its original context the scheme refers to very broad categories, such as X, Y, and W pathways in cat (Casagrande & Xu, 2004).

These results support and, critically, add a functional component to the recent anatomical observation that morphologically distinct RGCs contact common neurons in the mouse dLGN (Rompani et al., 2017). This study used single-cell-initiated retrograde rabies tracing from near the “ipsilateral” patch of the dLGN to show that while some TC neurons are contacted by 1-2 types of RGCs, many are contacted by tens of RGCs encompassing several different morphologically distinct types. However, contacts identified using rabies tracing may not always represent functional synapses (Callaway, 2008). I have not tried to match my results to the distinct modes of convergence identified by Rompani and colleagues due to low RGC labeling efficiency in my experiments (though that is also a likely caveat of rabies tracing) and difference in the region examined. Broadly, however, the trends are similar—the majority of TC neurons are contacted by or functionally integrate multiple types of RGCs, whereas a smaller fraction integrate inputs from primarily one type of RGC. However, while 7 of 25 (28%) TC neurons targeted by rabies tracing received all of their inputs from 1 (or 2 related) RGC types, fewer than 20% of the TC neurons I have sampled receive a dominant input from one RGC type (Table 5.1, 2/26 in the dual channel experiment). A higher sample size may help draw more meaningful distinctions within my data set, as would a more systematic comparison between the

proportion of input provided by one RGC type and the number of inputs the TC neuron receives overall (oEPSC versus electrical fiber fraction).

This study focuses on the convergence of diverse RGCs onto the same neurons. The divergence of single RGC axons has been demonstrated functionally and anatomically in other species (Hamos et al., 1987; Alonso et al., 2006; Alitto & Usrey, 2015; Weyand, 2016) and anatomically in mice (Morgan et al., 2016), but the degree of functional divergence in mice remains uncharacterized. With only ~300 labeled RGCs in BD;ChR2 retinæ, these were many TC neurons with robust BD inputs, some of these representing convergence of multiple BD-RGCs. Indirectly these observations imply that OODSGCs likely exhibit some degree of divergence, though they do not contact every available nearby postsynaptic partner (Hong et al., 2014). This is a highly relevant topic for future work, as retinogeniculate divergence and convergence likely shape mechanisms of thalamocortical visual processing (Alonso et al., 2006; Martinez et al., 2014; Usrey & Alitto, 2015).

Implications for direction and orientation selectivity in the mouse dLGN

A TC neuron that receives dominant inputs from one RGC type likely inherits its receptive field characteristics (Cleland & Levick, 1971; Usrey et al., 1999). However, how input strength shapes the feature selectivity of a TC neuron beyond its spatial characteristics, especially in combination with other inputs possessing other selectivity characteristics, is not a well-explored topic. The low proportion of TC neurons dominated by OODSRGC inputs in my data is consistent with the low number of highly direction-selective neurons encountered in the mouse dLGN *in vivo* (Marshel et al., 2012; Piscopo et al., 2013; Zhao et al., 2013). Orientation-selective neurons are detected more frequently than direction selective neurons, motivating some to hypothesize that geniculate orientation selectivity assembles from combinations of direction-selective neurons (Marshel et al., 2012; Piscopo et al., 2013; Zhao et al., 2013; Dhande et al., 2015; Stafford & Huberman, 2017). However, in contradiction to this hypothesis,

the higher number of responding neurons rather than higher response amplitudes in *CART;ChR2* (a mix of OODSRGCs) than *BD;ChR2* (OODSRGCs preferring a single direction) slices suggest that OODSRGCs preferring different amplitudes rarely converge together. Of course, other, non-OODSRGCs may converge together with OODSRGCs to enhance TC neuron feature selectivity, or selectivity may rely on inhibitory circuits, intrinsic dendritic properties (as recently shown for neurons in the superior colliculus: Gale & Murphy, 2016), or the detection of synchronous activity by neurons with relatively high retinogeniculate convergence—a mechanism previously ascribed to thalamocortical connectivity that is more broadly recognized as a high-convergence synapse (Stanley et al., 2012; Kelly et al., 2014). The availability of the *CART-Cre* mouse line and multiple technologies for the acute manipulation of neuronal activity (such as DREADDs or inhibitory opsins) motivate an obvious *in vivo* single unit recording experiment to test the contribution of OODSRGCs to geniculate direction and orientation selectivity by examining the effect of acute manipulation of *CART-RGC* activity on the encoding of these features.

The rare neurons that appear to receive all/most of their inputs from OODSRGCs are reminiscent of the dedicated pathway tracking OODSRGCs to the superficial primary visual cortex in mice identified through rabies tracing in mice (Cruz-Martín et al., 2014; Stafford & Huberman, 2017). It would therefore be very interesting to test whether these neurons also exhibit a different pattern of axonal projections in the visual cortex than TC neurons that combine inputs from multiple RGC types.

Future Directions

The dual channel stimulation experiments and characterization of labeling in retina presented in this study are preliminary and require elaboration. It is important that future experiments test whether other RGC types exhibit similar retinogeniculate connectivity as the cell types I have examined here. I am already planning to expand the dual channel stimulation

experiments to KCNG4-Cre mice, which label several types of alpha-RGCs (Sanes & Masland, 2014), but further exploration is limited by a very short list of available Cre lines that truly label a select group of RGCs (Martersteck et al., 2017). This powerful dual channel approach (Hooks et al., 2015) may also prove useful to exploring other aspects of retinogeniculate convergence, especially with regards to recent reports of binocular convergence (Howarth et al., 2014; Rompani et al., 2017; my n=1 experiment not included here is consistent with the authors' observations of binocularly innervated TC).

My findings remain difficult to interpret without a more nuanced understanding of the contribution and potential plasticity of strong and weak retinal inputs to the activity and feature selectivity of TC neurons. Future work should explore the influence of cell-intrinsic integration mechanisms (Sherman & Koch, 1986; Abbott & Regehr, 2004; Carandini et al., 2007; Sincich et al., 2007; Harnett et al., 2012; Silver, 2010), inhibitory circuits (Blitz & Regehr, 2005) and modulatory influences (Sherman, 2016) along with behavioral state (Hei et al., 2014), which may together dynamically shape the contribution diverse RGC inputs to the activity of TC neurons and neuronal ensembles. Future work *in vitro* and *in vivo* should address this question, not least with regard to the “slow currents” I note among my results.

This study represents a preliminary but important step to characterize the potential diversity of connectivity modes in retinogeniculate wiring. Understanding the patterns, principles, and development of convergence and divergence of diverse RGCs onto TC neurons will greatly inform the role of the dLGN in vision and enable progress towards new models of neural mechanisms of vision (Kaplan, 2014).

CHAPTER 6

Conclusions

Despite, or perhaps thanks to the rich history of the neurobiology of the visual system, the dLGN, and its role in visual processing remains mysterious and not a little overshadowed by the dazzling diversity of its retinal inputs and the elusive but apparent complexity of its cortical target. Nonetheless, renewed interest in the function and organization of the dLGN is revealing complexities that its most devoted students have hinted at all along.

In this dissertation, I have shown that geniculate neurons in mature mice receive approximately 10 inputs from the retina, which cover a broad range of amplitudes and frequently represent multiple types of RGCs. Together with the spatial breadth of individual RGC arbors that maintain the potential for retinogeniculate plasticity through bouton rearrangement (Hong et al., 2014), these results raise important questions about the role of the dLGN in visual processing and of attribution of specific functions among different stations of the visual system, more broadly.

Although the concept of parallel pathways in the visual system has long provided a convenient and clear framework for understanding the contribution of the retina, LGN, and visual cortex to visual processing, data presented in this dissertation build on a long history of experiments in the mouse and cat visual system that don't find strong evidence for it in the fine structural and functional anatomy of the dLGN (Chapter 1). The data presented in this dissertation together with existing *in vivo* and anatomical studies of retinogeniculate convergence (summarized in Chapter 1) show that the strength of individual RGC inputs ranges widely in the mature dLGN. In the context of a parallel pathways framework, it may be easiest to disregard the weak retinal inputs in the mature dLGN as leftovers from developmental plasticity with no functional relevance, or as the sloppy imprecision of an underdeveloped, underused, low-acuity visual system unchallenged in a small, visually unstimulating caged life of a rodent. However, weak inputs are also present in mature cats, which have much higher-acuity visual systems. There is also no clear separation between different populations, such as strong drivers and weak remnants, and a variety of discussed mechanisms (Chapter 1) may dynamically

enhance or suppress the strength of any individual retinal input. It is therefore worthwhile to consider the functional relevance of a more complex wiring diagram comprising both strong and weak retinal inputs.

Fortunately, studies of convergence and divergence of multiple functional retinogeniculate inputs have inspired several interesting hypotheses about the function of this complex circuitry at this stage of the visual system. First, the convergence of several (3-4) robust inputs can favor coding accuracy of geniculate spiking relative to only 1-2 inputs (Martinez et al., 2014). Second, a complex wiring diagram suggests that geniculate neurons, through the integration of different combinations of neighboring RGCs, may form an interpolated map of the visual scene that “fills in” gaps between receptive fields or creates novel receptive fields (Alonso et al., 2006; Usrey & Alitto, 2015). The convergence of multiple types and amplitudes of RGC inputs could produce TC neurons that code for novel features that drive visual cortical selectivity, or make it possible for single neurons or neuronal ensembles to process multiple types or combinations of retinal informational streams under different modulatory states. The computational capabilities of geniculate dendritic specializations (synaptic clustering on appendages, for example) and compartmentalization, and inhibitory circuits should be studied in the context of convergent retinal inputs to identify the appropriate functional unit of analysis at this stage of the visual system—whether a cluster of synapses, a dendrite, neuron, or ensemble of neurons (London & Häusser, 2005; Llinas & Steriade, 2006; Yuste, 2015). The contribution of weak inputs to postsynaptic activity may vary in vivo, as visual stimulation modulates the ability of both strong and weak RGC inputs to drive geniculate spiking (Usrey et al., 1999; Rowe & Fischer, 2001). Indeed, modulation of cortical feedback, alertness, short-term visual experience, and manipulation of RGC activity can modify receptive field properties and feature selectivity preferences of geniculate neurons, potentially as a result of unmasking or adjusting the weights of individual RGC inputs (Moore et al., 2011; Hei et al., 2014; Stoelzel et al., 2015; Aguila et al., 2017). Perhaps the contribution from multiple RGCs

with varied amplitudes could also produce neurons that exhibit partial selectivity to orientation or direction of motion of a stimulus, or neurons that exhibit different degrees of binocularity (Cheong et al., 2013; Howarth et al., 2014; Zeater et al., 2015; Suresh et al., 2016; Rompani et al., 2017). Interestingly, ipsilateral inputs may modulate dLGN neuronal activity based on eye position (Lal & Friedlander, 1990).

Third, the divergence of single RGCs that likely accompanies convergence (by the simple math of ~20-40,000 LGN-projecting RGCs (Jeon et al., 1998; Dhande et al., 2015) mapping onto <20,000 LGN neurons in mice (Ashwell, 1987), with ~10 RGC inputs per TC neuron (Chapter 4)) of axons onto multiple TC neurons enhances synchronous activity among TC neurons. This synchrony can increase signal-to-noise, encode novel information in synchronous firing patterns (including orientation/direction selectivity) or novel combinations of multiplexed RGCs, and enhance the detection of coincident geniculate or retinal activity in the cortex (Alonso et al., 1996; Dan et al., 1998; Usrey et al., 1998; Yeh et al., 2003; Koepsell et al., 2009; Rathbun et al., 2010; Wang et al., 2010; Stanley et al., 2012; Usrey & Alitto, 2015).

Of course, this dissertation relies on the study of the mouse dLGN. A systematic comparison of retinogeniculate synaptic connectivity between different species is lacking, and the difference in experimental approaches suitable to different species makes it difficult to reliably reconcile results across species. Therefore the synaptic integration of either numerous or diverse inputs described here for the mouse dLGN may not be a prominent feature of other species, or the functionality that this integration imparts to the mouse dLGN may be expressed at other stages of higher-acuity visual systems through different mechanisms. In support of this possible difference, the mouse V1 exhibits a higher proportion of neurons selective for complex motion that in other species, where this features characterize higher-order cortical areas (Palagina et al., 2017).

I began this project with the aim of understanding the logic of developmental retinogeniculate refinement. In the context of parallel visual pathways, the similarity in the time

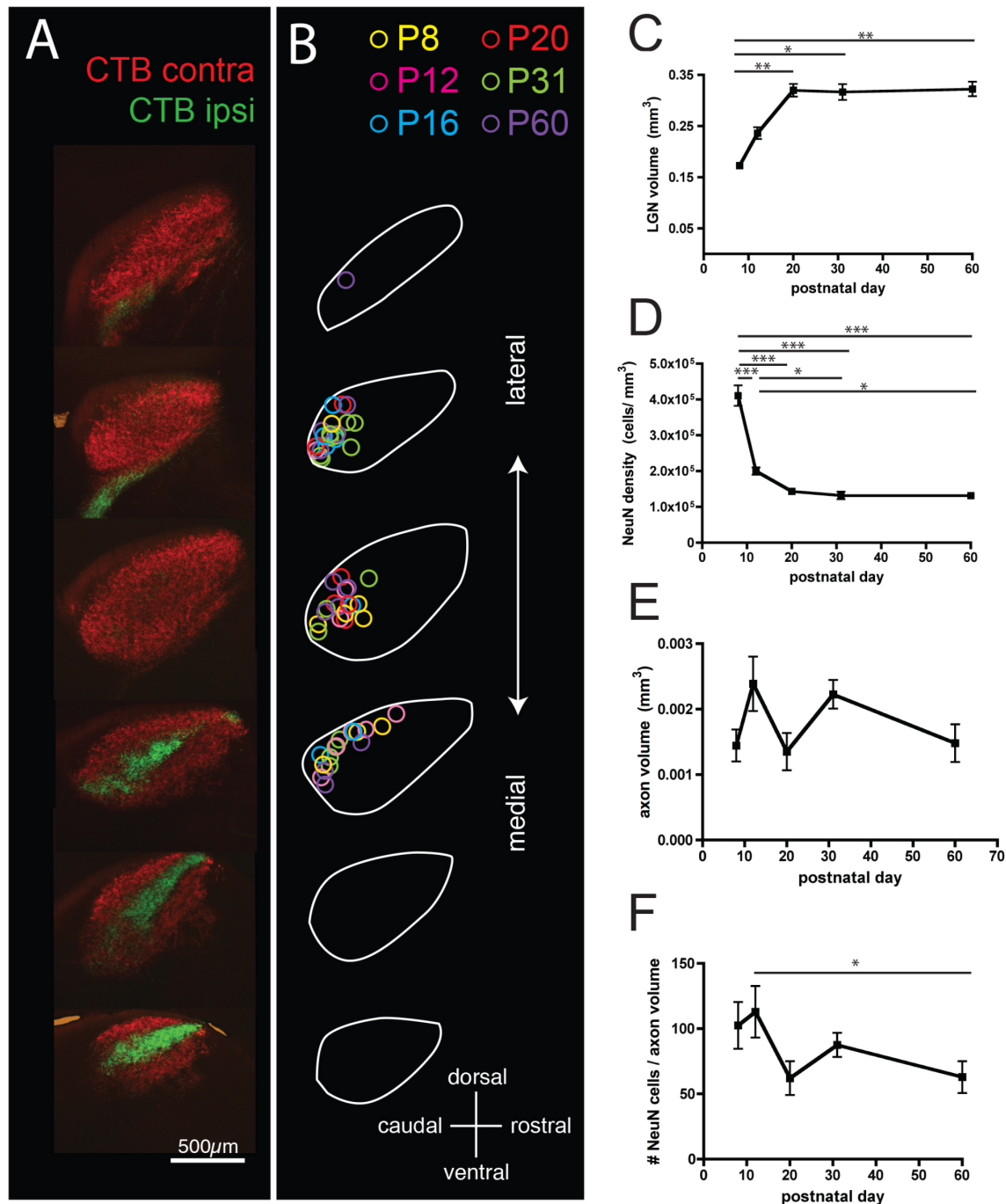
frame for retinogeniculate functional and morphological synaptic refinement (Chen & Regehr, 2000; Jaubert-Miazza et al., 2005; Hooks & Chen, 2006; Hong et al., 2014) and receptive field maturation (Tavazoie & Reid 2000, Akerman *et al.*, 2002, Davis *et al.*, 2015) has long implied that these processes reflect the segregation of initially intermingled retinal channels of information (Archer et al, 1982). In the context of the hypotheses I just outlined, then, together with the recent identification of the role of cortical feedback in this process (Thompson et al., 2016), my findings suggest that developmental refinement might instead represent the fine-tuning of the visual system to enable novel feature selectivity at the level of both the dLGN and the visual cortex. Rather than a process of segregation, the late phase of retinogeniculate refinement that follows eye specific segregation of axons from different eyes may enable meaningful multiplexing of diverse inputs to build novel channels of information that are appropriate for the experience and context of the individual animal. Taken together, therefore, the organization and short-term plasticity properties of the retinogeniculate circuit have set up a system that may actively tune and elaborate information conveyed from the retina to the cortex, suggesting that the dLGN participates in complex processing of visual information rather than simply relaying it the cortex (Sherman, 2016).

Finally, in considering the possible mechanistic underpinnings of geniculate function, it may be important to think beyond cell types and feature selectivity pathways in general. I have used genetic methods to access RGC types previously characterized by the intersection of their preferred stimulus features (characterized with a limited set of visual stimuli and under circumscribed conditions), morphology, and biochemistry. However, individual RGCs are not perfect detectors, and also respond weakly to non-preferred stimuli (J-RGCs themselves are an example; Kim et al., 2008; Joesch & Meister, 2016). Parsing the nervous system into cell types is a practical paradigm for dissecting its complexity, but may ultimately deemphasize information like patterns of responsiveness to non-preferred stimuli or the contribution of weak inputs, which may in the cell type context resemble “biological noise.” This “noise,” however, may serve a

computational purpose particularly in a population coding context (Béhuret et al., 2015, Kohn et al, 2016). Indeed, OODSRGCs have been the subject of two studies that demonstrated the potential contributions of noise correlations to coding information about the stimulus (Franke et al., 2016; Zylberberg et al., 2016), suggesting that the complexity of geniculate and cortical networks may reflect the salience of population rather than single-cell-based coding strategies in the visual system. To enable the field to properly explore whether such subtleties do have computational value downstream in the nervous system, it is important that dominant narratives within neuroscience that serve as the basis of communication between researchers working at different levels of analysis acknowledge and embrace the complexities that confound or challenge clear organizing principles. With respect to the visual system and the role of the dLGN within it, this may mean studying geniculate neurons not only as single, self-contained relays or segregated nodes in a sequential processing chain, but rather as a set of flexible ensembles or a population of potentially multifunctional elements in a densely interconnected network (Maunsell, 1992; Kaplan, 2014; Yuste 2015; Morgan et al., 2016).

APPENDIX

Supplementary Figures

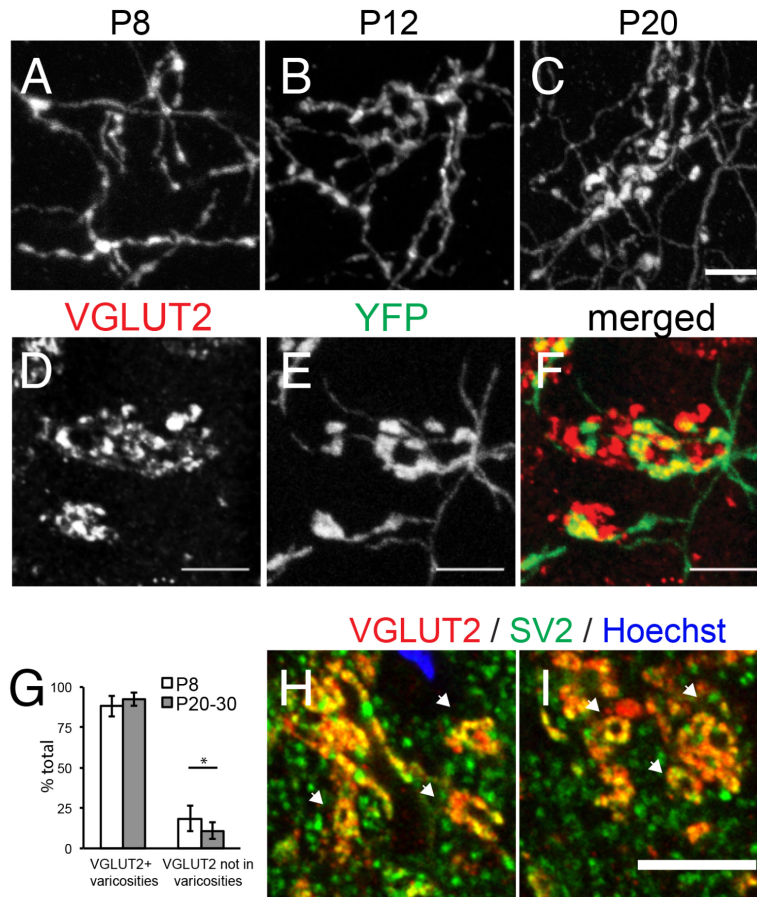


Supplementary Figure 7.1, related to Figure 3.1: Mapping of RGC Axon Arbors in the LGN.

(A) Eye-specific laminae in the LGN are shown in serial sections made in the sagittal plane. Axon terminals from the ipsilateral (green) and contralateral (red) eye are labeled by CTB conjugated to Alexa 488 or 647. Epifluorescence images of 100μm serial sections are shown. Sections are shown in order from lateral (top) to medial LGN (bottom). (B) Schematic of the positions of each axon used for this study superimposed onto the contours from LGN images in

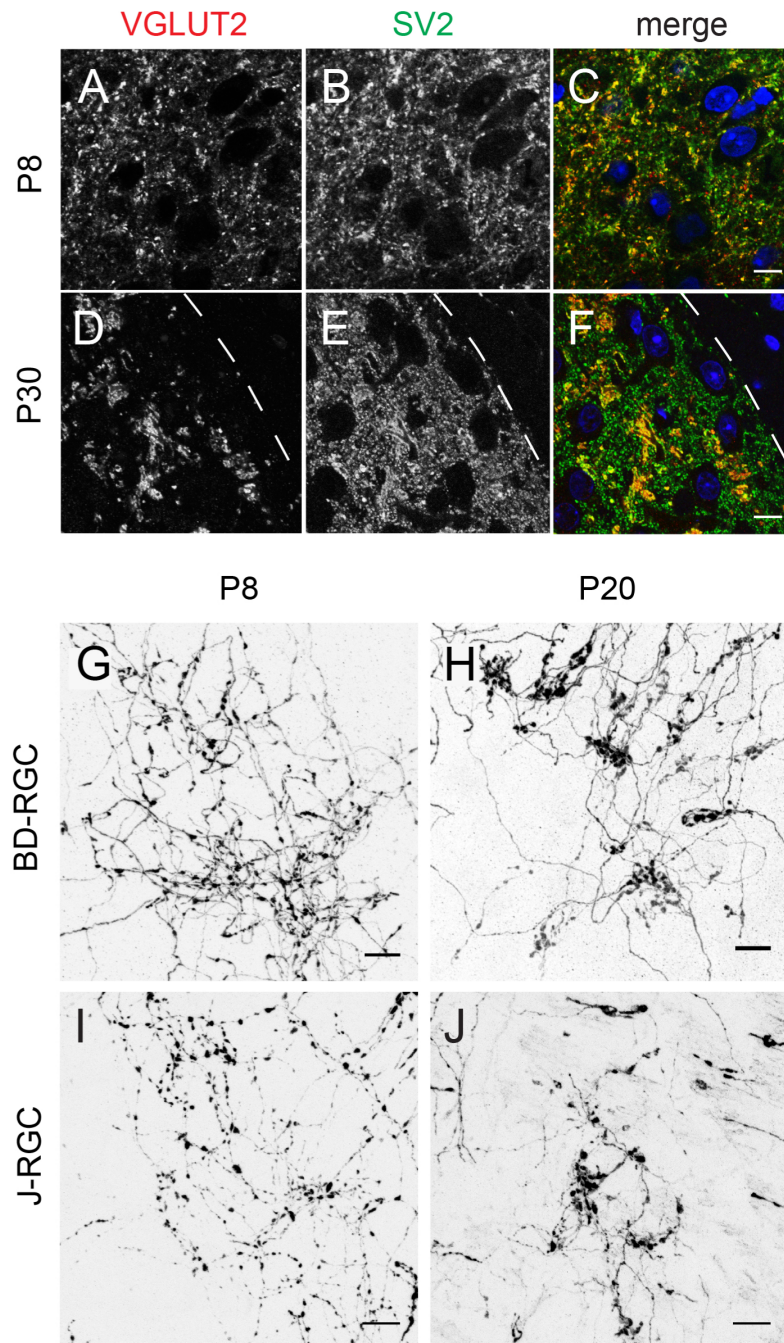
Supplementary Figure 7.1 (Continued)

A (colored circles). The majority of axons were located in the lateral-caudal portion of the LGN and within the contralateral projection area for all ages. Color of circle represents age of the reconstructed axon as shown. For P8, P12, P16, P20, P31, P60: $n = 8, 8, 8, 7, 12,$ and 11 respectively. (C) Quantification of the growth in mouse LGN volume over development are consistent with previous studies in growth of LGN size in rat (Satorre et al., 1986). (D) average density of neurons (identified by NeuN staining) in the LGN and (E) axon volume, measured by the convex hull encompassing the axon backbone, of individually reconstructed axon. (F) Estimated number of neurons encompassed by a single BD-RGC axon calculated from D and E. While the LGN increases in size, the total number of cells in the vicinity of the expanding axon remained relatively constant. * $p < 0.05$; ** $p < 0.01$; *** $p < 0.001$. Scale bar: $500\mu\text{m}$. Error bars: SEM.



Supplementary Figure 7.2, related to Figure 3.2: Varicosities are reliable markers for presynaptic boutons.

High-resolution confocal images at P8 (A), P12 (B), and P20 (C) show gradual increase in varicosity size over development. Colocalization of presynaptic marker of RGC terminals, VGLUT2 (D) and YFP labeled axon (E), and merged (F, VGLUT2 in red, YFP in green) at P31. Note that a single YFP-labeled BD-RGC axon terminates on a larger cluster of VGLUT2 puncta. Red VGLUT2 positive puncta are terminations from other, un-labeled RGCs. (G) Colocalization of varicosities and presynaptic marker control: quantification of the number of varicosities that colocalize with VGLUT2 (left) and VGLUT2 positive puncta found along axons outside of varicosities (right) for P8 (white bars) and P20-31 (gray bars). (H, I) P31 LGN labeled with antibodies against VGLUT2 (red) and SV2 (green). White arrows point to donut-shaped clusters formed by VGLUT2 positive boutons. Scale bars: A-F: 5μm; H, I: 10μm. Error bars: standard deviation.

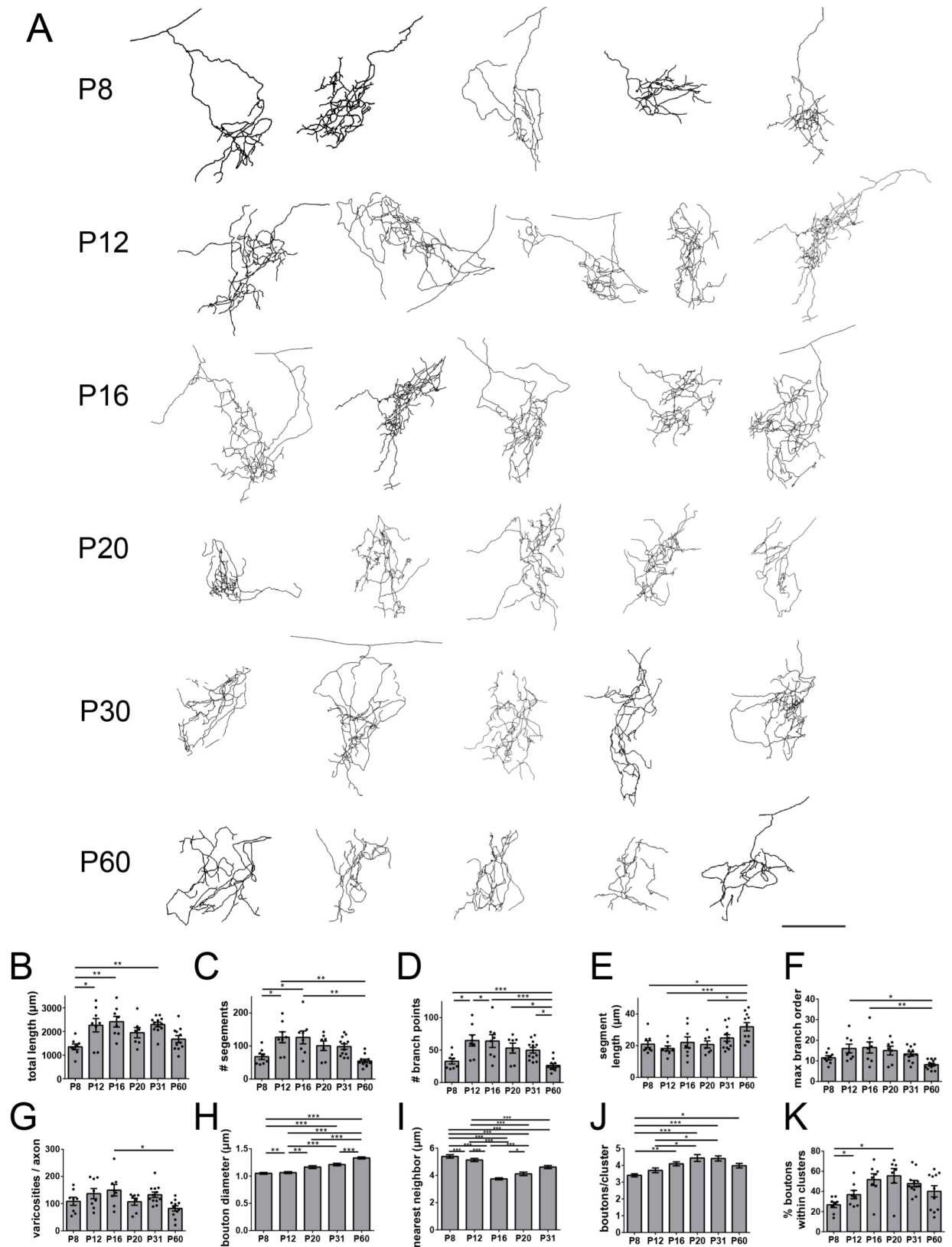


Supplementary Figure 7.3, related to Figure 3.2: Developmental bouton clustering is also evident in densely labeled samples.

(A-F) High resolution confocal images of LGN sections co-immunolabeled for RGC-specific presynaptic marker, VGLUT2 (A,D), pan-presynaptic marker SV2 (B,E), and merged images (C,F; SV2 in green, VGLUT2 in red). Hoechst-stained nuclei are shown in blue in C and F. Note that VGLUT2, a presynaptic marker for RGC terminals, clusters over development (compare A vs. D; C vs. F). Hoechst staining makes it evident that VGLUT2 staining becomes more

Supplementary Figure 7.3 (Continued)

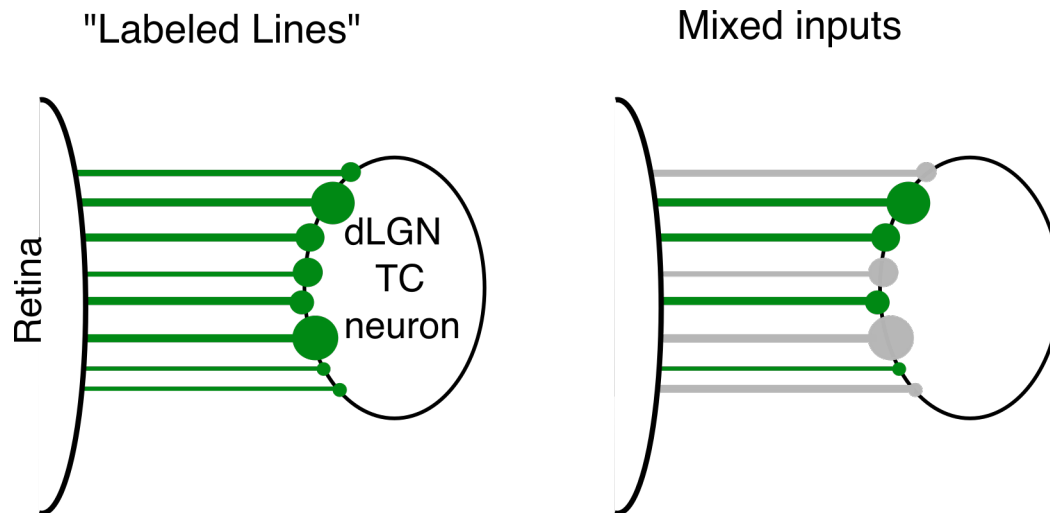
restricted with age rather than a growing soma crowding together synaptic contacts. As BD-RGCs represent only a minority of all VGLUT2-labeled RGC terminals, clustering is likely a mechanism used by other RGC types as well. (G-J) Maximum intensity projection of confocal image stacks of densely labeled (50-100 neurons) BD-RGC (G,H) and J-RGC (I,J) axons in the LGN. For both RGC-subtypes, bouton clustering becomes more evident at >P20 when compared to P8. G-J: gray scale inverted for visual clarity. Scale bars: 10um.



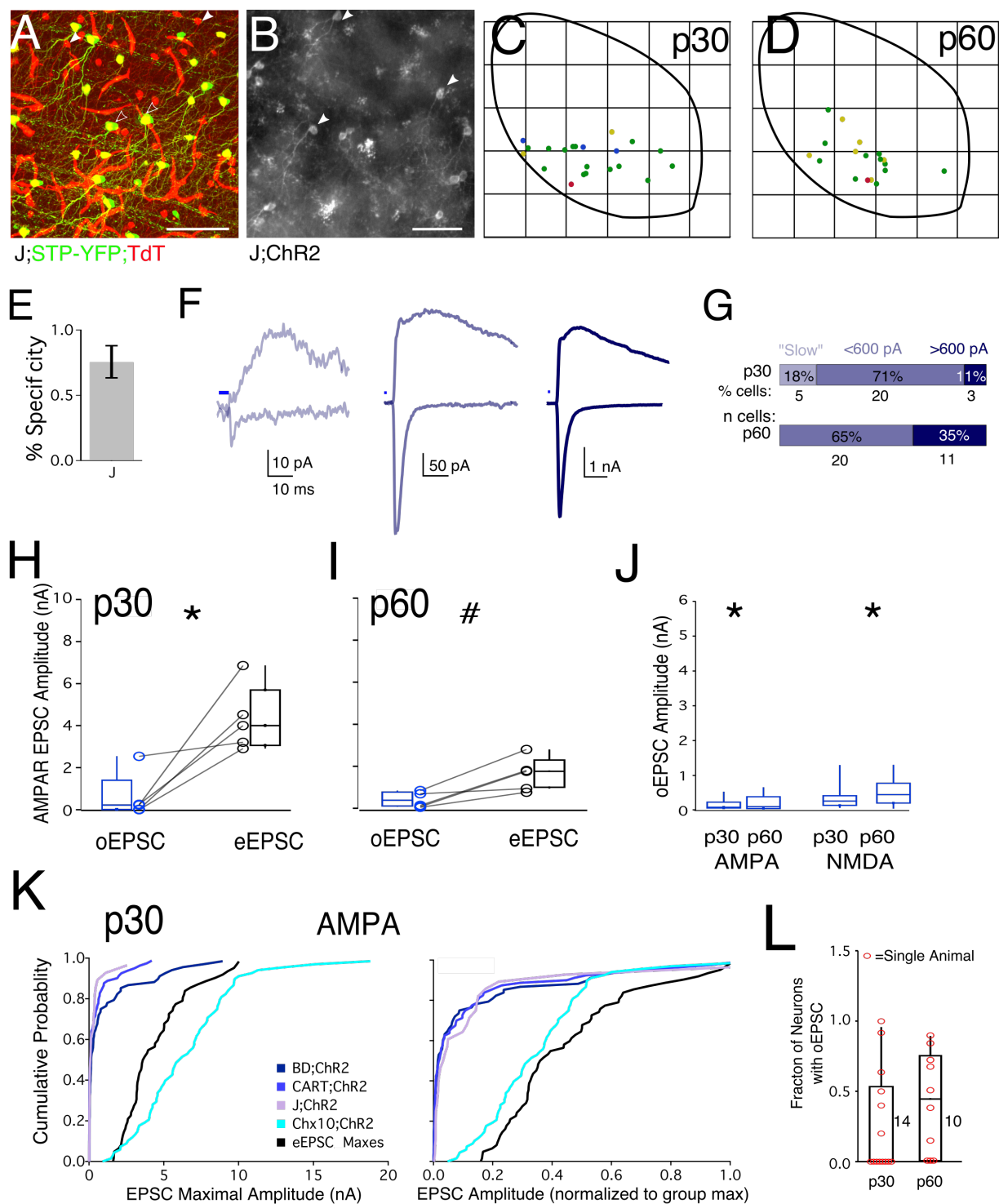
Supplementary Figure 7.4, related to Figure 4.4: Reconstruction of many RGC arbors.

Supplementary Figure 7.4 (Continued)

(A) More examples of reconstructed axon arbors at P8, 12, 16, 20, 30, and 60. Statistical analysis of axon backbone and bouton parameters of all ages analyzed together: average (B) total axon length (C) number of segments, (D) branch points, (E) segment length, (F) maximum branch order, (G) number of boutons per axon, (H) bouton diameter, (I) nearest neighbor distance, (J) boutons per cluster, and (K) fraction of boutons within clusters. Scale bars: 100 μm . Error bars: SEM.



Supplementary Figure 7.5: Schematic comparison of retinogeniculate wiring models. Left: a model of retinogeniculate wiring predicted by a labeled line hypothesis. A single dLGN thalamocortical neuron receives all of its inputs from one type of RGC (color represents type). Right: alternative hypothesis to labeled lines: multiple types of RGCs (two or more) converge onto single TC neurons.



Supplementary Figure 7.6: $J;ChR2$ oEPSCs follow a similar pattern to $BD;ChR2$ and $CART;ChR2$ oEPSCs.

A. Example confocal stack image of $J;STP-YFP;Ai14-TdT$ mouse retina showing YFP signal in green and Ai14-TdT signal in red in the RGC layer; Scale bar=100 μm . Activation of the Cre

Supplementary Figure 7.6 (Continued)

in *J;ChR2* mice results in GFP expression not only in RGCs but also a dense population of inner-retina neurons that project their dendrites close to the cell bodies of the RGCs, as well as vasculature and non-neuronal cells in many tissues of the brain. These signals make it difficult to directly assess the specificity of expression in *J;ChR2* retinæ. I hypothesized that the difference in expression pattern between *J;STP-YFP* mice described in the literature (Kim et al, 2008) and *J;ChR2* mice results from a difference between the Thy1 and CAG promoters. Unfortunately there is no independent marker available to identify J-RGCs. Instead, I used the Ai14 TDT reporter, which like the Ai32 reporter, is based on a CAG promoter (Madisen et al., 2012), as a proxy for the Ai32 reporter, and generated *J;STP-YFP;TDT* (Jamb-Cre-ER x Thy1-STP-YFP x Ai14) triple transgenic mice to use the more restricted *J;STP* to identify J-RGCs from other labeled cells in the retina. The unique unidirectional organization of the J-RGC dendrites makes it possible to identify single RGCs as J-RGCs if the direction of the primary dendrite can be identified and compared to identify *J;STP-YFP* RGCs. TDT⁺ cells in the RGC layer of the that exhibited a single primary dendrite that pointed in the same direction as *J;STP-YFP* RGCs were classified as J-RGCs. Cells with ambiguous morphology were classified as non-J-RGCs. The sum of YFP⁺:TDT⁺ (empty arrowheads) cells and TDT⁺ cells clearly identifiable as J-RGCs by their morphology (filled arrowheads) was divided by the total number of TDT⁺ cells in the RGC layer of *J;STP-YFP;TdT* mice (Figure 7E). 1-3 20X fields of view from 3 mice were used in the preliminary quantification. In the future, I will improve upon this quantification method by also counterstaining for Brn3A to avoid including non-RGC in the quantification. The specificity as quantified in E, therefore, may underestimate the proportion of labeled RGCs that are actually J-RGCs in *J;Ai14-TDT* and therefore perhaps in *J;ChR2* retinæ. I did not attempt to directly quantify the # of RGCs labeled in J-RGC retinæ, though I can revisit available tissue and perform analysis based on Brn3A counterstaining.(B). A rare example of *J;ChR2* retina that had sufficiently sparse background labeling to reveal the morphology of the RGCs (filled arrowheads). Scale bar=100 μ m (C, D). Spatial Distribution of *J;ChR2* oEPSCs in dLGN at P30 (C) and P60 (D). (E). Preliminary quantification of RGC labeling specificity as described in A, based on 3 double-labeled retinæ (P30). (F). Representative examples of *J;ChR2* oEPSCs (G). Distribution of *J;ChR2* oEPSCs at P30 and P60. (H-J). ChR2 oEPSCs and eEPSCs (bulk RGC stimulation) at P30 (H) and P60 (I). H and I show pairs of data points and box plot summaries for cells that had both a J:ChR2 oEPSC and an eEPSC (electrical stimulation of the OT). * $p < 0.05$ # $p = .0612$ Matched Wilcoxon. TC neurons sampled for these experiments were generally distributed more dorsally (experimenter's choice based on location of *J;STP* axons) than the region where retinogeniculate axons are intact for electrical stimulation, few cells exhibited an EPSC, and those that did had small eEPSC, corresponding to axon severing (Chapter 4). (J). comparison of *J;ChR2* AMPAR and NMDA oEPSCs at P30 and P60; these plots include additional cells for which the eEPSC was not collected. Comparing between age groups, AMPA $p = 0.1787$, NMDA $p = 0.0983$ MW. Further statistics for these figures are presented in Table 5.3. (K). Cumulative probability distribution plots of *J;ChR2* oEPSCs superimposed onto AMPAR plots presented in Figure 5.5 A&B. KW with Dunn yields comparison of all groups in both plots yield statistically significant difference ($p < 0.0001$) between each RGC subtype oEPSC data and the eEPSC and *Chx10;ChR2* oEPSC data sets. (L). Box plots and superimposed single data points show the proportion of patched TC neurons in each *J;ChR2* animal that exhibited an oEPSC. Numbers next to box plots list n of animals used for these experiments. Data includes those animals in which no TC neurons exhibited an eEPSC, but which had GFP labeling in the retina. The median line for the P30 plot is at 0.

References

- Abbott LF & Regehr WG (2004). Synaptic computation. *Nature* 431, 796–803.
- Ackman, J.B., Burbridge, T.J., and Crair, M.C. (2012). Retinal waves coordinate patterned activity throughout the developing visual system. *Nature* 490, 219–225.
- Aguila J, Cudeiro FJ & Rivadulla C (2017). Suppression of V1 Feedback Produces a Shift in the Topographic Representation of Receptive Fields of LGN Cells by Unmasking Latent Retinal Drives. *Cerebral Cortex* 27, 3331-3345.
- Akerman, C.J., Smyth, D., and Thompson, I.D. (2002). Visual experience before eye-opening and the development of the retinogeniculate pathway. *Neuron* 36, 869–879.
- Albrecht D, Davidowa H & Gabriel H (1990). Conditioning-Related Changes of Unit Activity in the Dorsal Lateral Geniculate Nucleus of Urethane-Anaesthetized Rats. *Brain Research Bulletin* 25, 55–63.
- Alitto HJ, Moore BD, Rathbun DL & Usrey WM (2011). A comparison of visual responses in the lateral geniculate nucleus of alert and anaesthetized macaque monkeys. *The Journal of physiology* 589, 87–99.
- Alonso JM, Usrey WM & Reid RC (1996). Precisely correlated firing in cells of the lateral geniculate nucleus. *Nature* 383, 815–819.
- Alonso JM, Yeh CI, Weng C & Stoelzel CR (2006). Retinogeniculate connections: a balancing act between connection specificity and receptive field diversity. *Progress in Brain Research* 154, 3–13.
- Antonini, A., and Stryker, M.P. (1993). Rapid remodeling of axonal arbors in the in the visual cortex. *260*, 1819–1821.
- Antonini, A., Fagiolini, M., and Stryker, M.P. (1999). Anatomical correlates of functional plasticity in mouse visual cortex. *J Neurosci* 19, 4388–4406.
- Arber S, Han B, Mendelsohn M, Smith M, Jessell TM & Sockanathan S (1999). Requirement for the homeobox gene Hb9 in the consolidation of motor neuron identity. *Neuron* 23, 659–674.
- Archer S, Dubin MW & Stark L (1982). Abnormal development of kitten retino-geniculate connectivity in the absence of action potentials. *Science* 217, 743–745.
- Ashwell K (1987). Direct and indirect effects on the lateral geniculate nucleus neurons of prenatal exposure to methylazoxymethanol. *Dev Brain Res* 35, 199–214.

Augustinaite S & Heggelund P (2007). Changes in firing pattern of lateral geniculate neurons caused by membrane potential dependent modulation of retinal input through NMDA receptors. *The Journal of physiology* 582, 297–315.

Becker N, Wierenga CJ, Fonseca R, Bonhoeffer T & Nägerl UV (2008). LTD Induction Causes Morphological Changes of Presynaptic Boutons and Reduces Their Contacts with Spines. *Neuron* 60, 590–597.

Béhuret S, Deleuze C & Bal T (2015). Corticothalamic Synaptic Noise as a Mechanism for Selective Attention in Thalamic Neurons. *Frontiers in Neural Circuits* 9, 1–21.

Benowitz LI, He Z & Goldberg JL (2017). Reaching the brain: Advances in optic nerve regeneration. *Experimental Neurology* 287, 365–373.

Bickford ME, Slusarczyk A, Dilger EK, Krahe TE, Kucuk C & Guido W (2010). Synaptic development of the mouse dorsal lateral geniculate nucleus. *The Journal of comparative neurology* 518, 622–635.

Binzegger, T., Douglas, R.J., and Martin, K.A.C. (2007). Stereotypical bouton clustering of individual neurons in cat primary visual cortex. *J Neurosci* 27, 12242–12254.

Bishop P, Burke W & Davis R (1959). Activation of single lateral geniculate cells by stimulation of either optic nerve. *Science* 130, 506–507.

Bishop P, Burke W & Davis R (1962). The interpretation of the extracellular response of the lateral geniculate cells. *Journal of Physiology* 1, 451–472.

Blackman MP, Djukic B, Nelson SB & Turrigiano GG (2012). A critical and cell-autonomous role for MeCP2 in synaptic scaling up. *The Journal of Neuroscience* 32, 13529–13536.

Blakemore C & Vital-Durand F (1985). Organization and post-natal development of the monkey's lateral geniculate nucleus. *Journal of Physiology* 380, 453–491.

Blitz DM, Foster KA & Regehr WG (2004). Short-term synaptic plasticity: a comparison of two synapses. *Nature Reviews Neuroscience* 5, 630–640.

Blitz DM & Regehr WG (2003). Retinogeniculate synaptic properties controlling spike number and timing in relay neurons. *Journal of Neurophysiology* 90, 2438–2450.

Borst, J.G., and Sakmann, B. (1996). Calcium influx and transmitter release in a fast CNS synapse. *Nature* 383, 431–434.

Budisantoso T, Matsui K, Kamasawa N, Fukazawa Y & Shigemoto R (2012). Mechanisms

underlying signal filtering at a multisynapse contact. *The Journal of Neuroscience* 32, 2357–2376.

Buffelli M, Burgess RW, Feng G, Lobe CG, Lichtman JW & Sanes JR (2003). Genetic evidence that relative synaptic efficacy biases the outcome of synaptic competition. *Nature* 424, 430–434.

Butts DA, Kanold PO & Shatz CJ (2007). A burst-based ‘Hebbian’ learning rule at retinogeniculate synapses links retinal waves to activity-dependent refinement. *PLoS biology* 5, e61.

Butts DA & Rokhsar DS (2001). The Information Content of Spontaneous Retinal Waves. 21, 961–973.

Cai, D., DeAngelis, G.C., and Freeman, R.D. (1997). Spatiotemporal Receptive Field Organization in the Lateral Geniculate Nucleus of Cats and Kittens. *Journal of Neurophysiology* 78, 1045–1061.

Callaway EM (2008). Transneuronal circuit tracing with neurotropic viruses. *Current Opinion in Neurobiology* 18, 617–623.

Campbell G & Shatz CJ (1992). Synapses Formed by identified retinogeniculate axons during the segregation of eye input. *Journal of Neuroscience* 12, 1847–1858.

Cang J & Feldheim DA (2013). Developmental Mechanisms of Topographic Map Formation and Alignment. *Annual Review of Neuroscience* 36, 51–77.

Carandini M, Horton JC & Sincich LC (2007). Thalamic filtering of retinal spike trains by postsynaptic summation. *Journal of Vision* 7, 20.1-11.

Carden WB, Datskovskaia A, Guido W, Godwin DW & Bickford ME (2000). Development of the cholinergic, nitroergic, and GABAergic innervation of the cat dorsal lateral geniculate nucleus. *The Journal of comparative neurology* 418, 65–80.

Casagrande VA & Xu X (2004). Parallel visual pathways: a comparative perspective. *The Visual Neurosciences* 494–506.

Cetin A & Callaway EM (2014). Optical control of retrogradely infected neurons using drug-regulated ‘TLoop’ lentiviral vectors. *Journal of neurophysiology* 111, 2150–2159.

Chen C, Bickford ME & Hirsch JA (2016). Untangling the Web between Eye and Brain. *Cell* 165, 20–21.

Chen C, Blitz DM & Regehr WG (2002). Contributions of receptor desensitization and saturation

to plasticity at the retinogeniculate synapse. *Neuron* 33, 779–788.

Chen C & Regehr WG (2000). Developmental remodeling of the retinogeniculate synapse. *Neuron* 28, 955–966.

Chen C & Regehr WG (2003). Presynaptic modulation of the retinogeniculate synapse. *The Journal of Neuroscience* 23, 3130–3135.

Cheng, T-W, Liu, X-., Faulkner, R, Stephan, AH, Barres, BA, Huberman, AD, and Cheng, H-J (2010). Emergence of Lamina-Specific Retinal Ganglion Cell Connectivity by Axon Arbor Retraction and Synapse Elimination. *J. Neurosci.* 30, 16376–16382.

Cheong SKK, Tailby C, Solomon SG & Martin PR (2013). Cortical-like receptive fields in the lateral geniculate nucleus of marmoset monkeys. *J Neurosci* 33, 6864–6876.

Chung W-S, Clarke LE, Wang GX, Stafford BK, Sher A, Chakraborty C, Joung J, Foo LC, Thompson A, Chen C, Smith SJ & Barres BA (2013). Astrocytes mediate synapse elimination through MEGF10 and MERTK pathways. *Nature* 504, 394–400.

Cleland BG, Dubin MW & Levick WR (1971). Sustained and transient neurones in the cat's retina and lateral geniculate nucleus. *J Physiology* 217, 473–496.

Cleland BG & Lee BB (1985). A comparison of visual responses of cat lateral geniculate nucleus neurones with those of ganglion cells afferent to them. *J Physiol* 369, 249–268.

Cleland BG & Levick WR (1971). Simultaneous recording of input and output of lateral geniculate neurones. *Nature* 231, 191–192.

Clem RL & Barth A (2006). Pathway-specific trafficking of native AMPARs by in vivo experience. *Neuron* 49, 663–670.

Clements JD, Lester R a, Tong G, Jahr CE & Westbrook GL (1992). The time course of glutamate in the synaptic cleft. *Science (New York, NY)* 258, 1498–1501.

Coleman, J.E., Nahmani, M., Gavnornik, J.P., Haslinger, R., Heynen, A.J., Erisir, A., and Bear, M.F. (2010). Rapid structural remodeling of thalamocortical synapses parallels experience-dependent functional plasticity in mouse primary visual cortex. *J. Neurosci.* 30, 9670–9682.

Coenen AML, Gerrits HJM & Vendrik AJH (1972). Analysis of the response characteristics of optic tract and geniculate units and their mutual relationship. *Experimental Brain Research* 15, 452–471.

Conley M & Fitzpatrick D (1989). Morphology of Retinogeniculate Axons in the Macaque. *Visual*

neuroscience 2, 287–296.

Cruz-Martín, A., El-Danaf, R.N., Osakada, F., Sriram, B., Dhande, O.S., Nguyen, P.L., Callaway, E.M., Ghosh, A., and Huberman, A.D. (2014). A dedicated circuit links direction-selective retinal ganglion cells to the primary visual cortex. *Nature* 507, 358–361.

Cull-Candy SG, Kelly L & Farrant M (2006). Regulation of Ca²⁺-permeable AMPA receptors: synaptic plasticity and beyond. *Current opinion in neurobiology* 16, 288–297.

Dan Y, Alonso JM, Usrey WM & Reid RC (1998). Coding of visual information by precisely correlated spikes in the lateral geniculate nucleus. *Nature neuroscience* 1, 501–507.

Danbolt NC (2001). Glutamate uptake. *Progress in Neurobiology* 65, 1–105.

Daniels JD, Norman JL & Pettigrew JD (1977). Biases for oriented moving bars in lateral geniculate nucleus neurons of normal and stripe-reared cats. *Experimental Brain Research* 29, 155–72.

Daniels JD, Pettigrew JD & Norman JL (1978). Development of Single-Neuron Responses in Kitten's Lateral Geniculate Nucleus. *Journal of neurophysiology* 41, 1373–1393.

Denman D & Contreras D (2016). On Parallel Streams through the Mouse Dorsal Lateral Geniculate Nucleus. *Frontiers in neural circuits* 10, 20.

Denman D, Siegle JH, Koch C, Reid RC & Blanche TJ (2016). Spatial organization of chromatic pathways in the mouse dorsal lateral geniculate nucleus. *Journal of Neuroscience* 37, 1102–1116.

Davis, Z.W., Chapman, B., and Cheng, H.-J. (2015). Increasing Spontaneous Retinal Activity before Eye Opening Accelerates the Development of Geniculate Receptive Fields. *Journal of Neuroscience* 35, 14612–14623.

Dhande OS, Hua EW, Guh E, Yeh J, Bhatt S, Zhang Y, Ruthazer ES, Feller MB & Crair MC (2011). Development of single retinofugal axon arbors in normal and $\beta 2$ knock-out mice. *The Journal of Neuroscience* 31, 3384–3399.

Dhande OS, Stafford BK, Lim JA & Huberman AD (2015). Contributions of Retinal Ganglion Cells to Subcortical Visual Processing and Behaviors. *Annual Review of Vision Science* 1, 291–328.

Diamond JS & Jahr CE (1997). Transporters buffer synaptically released glutamate on a submillisecond time scale. *The Journal of Neuroscience* 17, 4672–4687.

Dilger EK, Krahe TE, Morhardt, Seabrook TA, Shin H-S & Guido W (2015). Absence of plateau potentials in dLGN cells leads to a breakdown in retinogeniculate refinement. *The Journal of Neuroscience* 35, 3652–3662.

Duan X, Qiao M, Bei F, Kim IJ, He Z & Sanes JR (2015). Subtype-Specific regeneration of retinal ganglion cells following axotomy: Effects of osteopontin and mtor signaling. *Neuron* 85, 1244–1256.

El-Danaf RN, Krahe TE, Dilger EK, Bickford ME, Fox M & Guido W (2015). Developmental remodeling of relay cells in the dorsal lateral geniculate nucleus in the absence of retinal input. *Neural Development* 10, 19.

Erzurumlu, R.S., Jhaveri, S., and Schneider, G.E. (1988). Distribution of morphologically different retinal axon terminals in the hamster dorsal lateral geniculate nucleus. *Brain Res* 461, 175–181.

Famiglietti E V & Peters A (1972). The synaptic glomerulus and the intrinsic neuron in the dorsal lateral geniculate nucleus of the cat. *J Comp Neurol* 144, 285–334.

Felch DL & Van Hooser SD (2012). Molecular compartmentalization of lateral geniculate nucleus in the gray squirrel (*Sciurus carolinensis*). *Frontiers in neuroanatomy* 6, 12.

Feller, M.B. (1999). Spontaneous Correlated Activity in Developing Neural Circuits. *Neuron* 22, 653–656.

Feller MB (2009). Retinal waves are likely to instruct the formation of eye-specific retinogeniculate projections. *Neural development* 4, 24.

Fisher TG, Alitto HJ & Usrey WM (2017). Retinal and Non-Retinal Contributions to Extraclassical Surround Suppression in the Lateral Geniculate Nucleus. *Journal of Neuroscience* 37, 226–235.

Franke F, Fiscella M, Sevelev M, Roska B, Hierlemann A & Azeredo da Silveira R (2016). Structures of Neural Correlation and How They Favor Coding. *Neuron* 89, 409–422.

Freche D, Pannasch U, Rouach N & Holcman D (2011). Synapse geometry and receptor dynamics modulate synaptic strength. *PLoS ONE*; DOI: 10.1371/journal.pone.0025122.

Fujiyama F, Hioki H, Tomioka R, Taki K, Tamamaki N, Nomura S, Okamoto K & Kaneko T (2003). Changes of immunocytochemical localization of vesicular glutamate transporters in the rat visual system after the retinofugal denervation. *Journal of Comparative Neurology* 465, 234–249.

Fukuda Y, Hsiao CF, Watanabe M & Ito H (1984). Morphological correlates of physiologically identified Y-, X-, and W-cells in cat retina. *Journal of Neurophysiology* 52, 999–1013.

Gale SD & Murphy GJ (2016). Active Dendritic Properties and Local Inhibitory Input Enable Selectivity for Object Motion in Mouse Superior Colliculus Neurons. *Journal of Neuroscience* 36, 9111–9123.

Garraghty PE, Salinger WL & Macavoy MG (1985). The development of cell size in the dorsal lateral geniculate nucleus of monocularly paralyzed cats. *Brain Res* 353, 99–106.

Garraghty PE, Shatz CJ, Sretavan DW & Sur M (1988). Axon arbors of X and Y retinal ganglion cells are differentially affected by prenatal disruption of binocular inputs. *Proceedings of the National Academy of Sciences* 85, 7361–7365.

Garraghty PE & Sur M (1993). Competitive interactions influencing the development of retinal axonal arbors in cat lateral geniculate nucleus. *Physiol Rev* 73, 529–545.

Gary-Bobo, E., Przybylski, J., and Saillour, P. (1995). Experience-dependent maturation of the spatial and temporal characteristics of the cell receptive fields in the kitten visual cortex. *Neuroscience Letters* 189, 147–150.

Glees P & Le Gros Clark WE (1941). The termination of optic fibres in the lateral geniculate body of the monkey. *The Journal of Anatomy* 75, 295–307.

Golding B., Pouchelon, G., Bellone, C., Murthy, S., Nardo, A.A. Di, Govindan, S., Ogawa, M., Shimogori, T., Lu, C., Di Nardo, A.A., et al. (2014). Retinal Input Directs the Recruitment of Inhibitory Interneurons into Thalamic Visual Circuits. *Neuron* 81, 1057–1069.

Grant E, Hoerder-Suabedissen A & Molnar Z (2016). The Regulation of Corticofugal Fiber Targeting by Retinal Inputs. *Cerebral Cortex* 26, 1336–1348.

Graydon CW, Cho S, Diamond JS, Kachar B, von Gersdorff H & Grimes WN (2014). Specialized postsynaptic morphology enhances neurotransmitter dilution and high-frequency signaling at an auditory synapse. *The Journal of Neuroscience* 34, 8358–8372.

Guido W (2008). Refinement of the retinogeniculate pathway. *The Journal of physiology* 586, 4357–4362.

Guillery R & Sherman SM (2002). Thalamic relay functions and their role in corticocortical communication: generalizations from the visual system. *Neuron* 33, 163–175.

Hammer S, Monavarfeshani A, Lemon T, Su J & Fox MA (2015). Multiple Retinal Axons Converge onto Relay Cells in the Adult Mouse Thalamus. *Cell Reports* 12, 1575–1583.

Hamos JE, Van Horn SC, Raczkowski D & Sherman SM (1987). Synaptic circuits involving an individual retinogeniculate axon in the cat. *The Journal of comparative neurology* 259, 165–192.

Hanganu, I.L., Ben-Ari, Y., and Khazipov, R.R. (2006). Retinal waves trigger spindle bursts in the neonatal rat visual cortex. *The Journal of Neuroscience* 26, 6728–6736.

Harnett MT, Makara JK, Spruston N, Kath WL & Magee JC (2012). Synaptic amplification by dendritic spines enhances input cooperativity. *Nature* 3–9.

Hashimoto, K., Ichikawa, R., Kitamura, K., Watanabe, M., and Kano, M. (2009). Translocation of a “winner” climbing fiber to the Purkinje cell dendrite and subsequent elimination of “losers” from the soma in developing cerebellum. *Neuron* 63, 106–118.

Hauser JL, Edson EB, Hooks BM & Chen C (2013). Metabotropic glutamate receptors and glutamate transporters shape transmission at the developing retinogeniculate synapse. *J Neurophysiol* 109, 113–123.

Hauser JL, Liu X, Litvina EY & Chen C (2014). Prolonged synaptic currents increase relay neuron firing at the developing retinogeniculate synapse. *Journal of Neurophysiology* 112, 1714–1728.

Hei X, Stoelzel CR, Zhuang J, Bereshpolova Y, Huff JM, Alonso JM & Swadlow HA (2014). Directional selective neurons in the awake LGN: response properties and modulation by brain state. *Journal of Neurophysiology* 112, 362–373.

Hong YK & Chen C (2011). Wiring and rewiring of the retinogeniculate synapse. *Current opinion in neurobiology* 21, 228–237.

Hong YK, Park S, Litvina EY, Morales J, Sanes JR & Chen C (2014). Refinement of the Retinogeniculate Synapse by Bouton Clustering. *Neuron* 84, 332–339.

Hooks BM & Chen C (2006). Distinct roles for spontaneous and visual activity in remodeling of the retinogeniculate synapse. *Neuron* 52, 281–291.

Hooks BM & Chen C (2007). Critical periods in the visual system: changing views for a model of experience-dependent plasticity. *Neuron* 56, 312–326.

Hooks BM & Chen C (2008). Vision triggers an experience-dependent sensitive period at the retinogeniculate synapse. *The Journal of Neuroscience* 28, 4807–4817.

Hooks BM, Lin JY, Guo C & Svoboda K (2015). Dual-channel circuit mapping reveals sensorimotor convergence in the primary motor cortex. *The Journal of Neuroscience* 35, 4418–4426.

van Horn SC, Erişir A & Sherman SM (2000). Relative distribution of synapses in the A-laminae of the lateral geniculate nucleus of the cat. *Journal of Comparative Neurology* 416, 509–520.

Howarth M, Walmsley L & Brown TM (2014). Report Binocular Integration in the Mouse Lateral Geniculate Nuclei. *Current Biology* 24, 1241–1247.

Hua, J.Y., Smear, M.C., Baier, H., and Smith, S.J. (2005). Regulation of axon growth in vivo by activity-based competition. *Nature* 434, 1022–1026.

Hubel DH & Wiesel TN (1961). Integrative Action in the Cat's Lateral Geniculate Body. *The Journal of Physiology* 155, 385–398.

Hubel DH & Wiesel TN (1970). The period of susceptibility to the physiological effects of unilateral eye closure in kittens. *The Journal of physiology* 206, 419–436.

Huberman, A. (2007). Mechanisms of eye-specific visual circuit development. *Curr Opin Neurobiol* 17, 73–80.

Huberman AD, Feller MB & Chapman B (2008). Mechanisms Underlying Development of Visual Maps and Receptive Fields. *Annual Review of Neuroscience* 31, 479–509.

Huberman AD, Manu M, Koch SM, Susman MW, Lutz AB, Ullian EM, Baccus S a & Barres B a (2008). Architecture and activity-mediated refinement of axonal projections from a mosaic of genetically identified retinal ganglion cells. *Neuron* 59, 425–438.

Huganir RL & Nicoll RA (2013). AMPARs and Synaptic Plasticity: The Last 25 Years. *Neuron* 80, 704–717.

Isaac JTR, Nicoll RA & Malenka RC (1995). Evidence for silent synapses: Implications for the expression of LTP. *Neuron* 15, 427–434.

Jackman SL, Beneduce BM, Drew IR & Regehr WG (2014). Achieving High-Frequency Optical Control of Synaptic Transmission. *Journal of Neuroscience* 34, 7704–7714.

Jacobs EC, Campagnoni C, Kampf K, Reyes SD, Kalra V, Handley V, Xie Y-Y, Hong-Hu Y, Spreur V, Fisher RS & Campagnoni AT (2007). Visualization of corticofugal projections during early cortical development in a tau-GFP-transgenic mouse. *The European journal of neuroscience* 25, 17–30.

Jaubert-Miazza L, Green E, Lo F-S, Bui K, Mills J & Guido W (2005). Structural and functional composition of the developing retinogeniculate pathway in the mouse. *Visual neuroscience* 22, 661–676.

Jeon C, Strettoi E & Masland RH (1998). The Major Cell Populations of the Mouse Retina. 18, 8936–8946.

Joesch M & Meister M (2016). A neuronal circuit for colour vision based on rod–cone opponency. *Nature* 532, 236–239.

Jones EG & Powell TPS (1969). Electron Microscopy of synaptic glomeruli in the thalamic relay nuclei in cat. *Proceedings of the Royal Society* 172, 153–171.

Kano M & Hashimoto K (2009). Synapse elimination in the central nervous system. *Current Opinion in Neurobiology* 19, 154–161.

Kaplan E (2014). The M, P and K pathways of the Primate Visual System revisited. In *The New Visual Neuroscience*, pp. 215–226. MIT Press.

Kaplan E, Purpura K & Shapley RM (1987). Contrast Affects the transmission of visual information through the mammalian lateral geniculate nucleus. *J Physiol* 267–288.

Kaplan E & Shapley R (1984). The origin of the S (slow) potential in the mammalian Lateral Geniculate Nucleus. *Experimental Brain Research* 55, 111–116.

Kastner S, Schneider KA & Wunderlich K (2006). Beyond a relay nucleus: neuroimaging views on the human LGN. *Progress in brain research* 155, 125–143.

Katz, L.C., and Shatz, C.J. (1996). Synaptic activity and the construction of cortical circuits. *Science* 274, 1133–1138.

Kay, JN, de la Huerta, I, Kim, I-J, Zhang, Y, Yamagata, M, Chu, MW, Meister, M, and Sanes, JR (2011). Retinal Ganglion Cells with Distinct Directional Preferences Differ in Molecular Identity, Structure, and Central Projections. *J. Neurosci.* 31, 7753–7762.

Keller-Peck, CR, Walsh, MK, Gan, W, Feng, G, Sanes, JR, Lichtman, JW, and Louis, S (2001). in Neonatal Motor Units: Studies Using GFP Transgenic Mice. *Neuron* 31, 381–394.

Kelly ST, Kremkow J, Jin J, Wang Y, Wang Q, Alonso JM & Stanley GB (2014). The Role of Thalamic Population Synchrony in the Emergence of Cortical Feature Selectivity. *PLoS Computational Biology* 10, e1003418

Kielland A, Bochorishvili G, Corson J, Zhang L, Rosin DL, Heggelund P & Zhu JJ (2009). Activity patterns govern synapse-specific AMPA receptor trafficking between deliverable and synaptic pools. *Neuron* 62, 84–101.

Kielland A & Heggelund P (2002). AMPA and NMDA currents show different short-term

depression in the dorsal lateral geniculate nucleus of the rat. *The Journal of Physiology* 542, 99–106.

Kim I-J, Zhang Y, Meister M & Sanes JR (2010). Laminar restriction of retinal ganglion cell dendrites and axons: subtype-specific developmental patterns revealed with transgenic markers. *The Journal of Neuroscience* 30, 1452–1462.

Kim I-J, Zhang Y, Yamagata M, Meister M & Sanes JR (2008). Molecular identification of a retinal cell type that responds to upward motion. *Nature* 452, 478–482.

Kingston A., Ornstein P., Wright R., Johnson B., Mayne N., Burnett J., Belagaje R, Wu S & Schoepp D. (1998). LY341495 is a nanomolar potent and selective antagonist of group II metabotropic glutamate receptors. *Neuropharmacology* 37, 1–12.

Kleindienst, T., Winnubst, J., Roth-Alpermann, C., Bonhoeffer, T., and Lohmann, C. (2011). Activity-dependent clustering of functional synaptic inputs on developing hippocampal dendrites. *Neuron* 72, 1012–1024.

Knudsen, EI, Zheng, W, and DeBello, WM. (2000). Traces of learning in the auditory localization pathway. *Proc. Natl. Acad. Sci. U. S. A.* 97, 11815–11820.

Koch C (1985). Understanding the intrinsic circuitry of the cat's lateral geniculate nucleus: electrical properties of the spine-triad arrangement. *Proceedings of the Royal Society of London Series B* 225, 365–390.

Koepsell K, Wang X, Vaingankar V, Wei Y, Wang Q, Rathbun DL, Usrey WM, Hirsch JA & Sommer FT (2009). Retinal oscillations carry visual information to cortex. *Frontiers in Systems Neuroscience* 3, 4.

Kohn A, Coen-Cagli R, Kanitscheider I & Pouget A (2016). Correlations and Neuronal Population Information. *Annual Review of Neuroscience* 39, 237–256.

Krahe TE, El-Danaf RN, Dilger EK, Henderson SC & Guido W (2011). Morphologically Distinct Classes of Relay Cells Exhibit Regional Preferences in the Dorsal Lateral Geniculate Nucleus of the Mouse. *Journal of Neuroscience* 31, 17437–17448.

Krahe TE & Guido W (2011). Homeostatic plasticity in the visual thalamus by monocular deprivation. *The Journal of Neuroscience* 31, 6842–6849.

von Krosigk M, Bal T & McCormick DA (1993). Cellular mechanisms of a synchronized oscillation in the thalamus. *Science (New York, NY)* 261, 361–364.

Kumar SS, Bacci A, Kharazia V & Huguenard JR (2002). A developmental switch of AMPA

receptor subunits in neocortical pyramidal neurons. *The Journal of Neuroscience* 22, 3005–3015.

Kwon YH, Esguerra M & Sur M (1991). NMDA and non-NMDA receptors mediate visual responses of neurons in the cat's lateral geniculate nucleus. *J Neurophysiol* 66, 414–28.

Lachica EA & Casagrande VA (1988). Development of Primate Retinogeniculate Axons. *Visual neuroscience* 1, 103–123.

Lal R & Friedlander J (1990). Effect of Passive Eye Position Changes on Retinogeniculate Transmission in the Cat. *Journal of Neurophysiology* 63, 502–522.

Lam Y-W & Sherman SM (2013). Activation of both Group I and Group II metabotropic glutamatergic receptors suppress retinogeniculate transmission. *Neuroscience* 242, 78–84.

Land, PW, Kyonka, E, and Shamalla-Hannah, L (2004). Vesicular glutamate transporters in the lateral geniculate nucleus: expression of VGLUT2 by retinal terminals. *Brain Res* 996, 251–254.

Lee BB, Creutzfeldt OD & Elepfandt A (1979). The responses of magno- and parvocellular cells of the monkey's lateral geniculate body to moving stimuli. *Experimental Brain Research* 35, 547–557.

Lee BB, Virsu V & Creutzfeldt OD (1983). Linear signal transmission from prepotentials to cells in the macaque lateral geniculate nucleus. *Experimental Brain Research* 52, 50–56.

Lee H, Brott BK, Kirkby LA, Adelson JD, Cheng S, Feller MB, Datwani A & Shatz CJ (2014). Synapse elimination and learning rules co-regulated by MHC class I H2-Db. *Nature* 509, 195–200.

Levick WR, Cleland BG & Dubin MW (1972). Lateral geniculate neurons of cat: retinal inputs and physiology. *Investigative ophthalmology* 11, 302–311.

Levick WR, Oyster CW & Takahashi E (1969). Rabbit Lateral Geniculate Nucleus: Sharpener of Directional Information. *Science* 165, 712–714.

Levick WR & Thibos LNLN (1980). Orientation bias of cat retinal ganglion cell. *Nature* 286, 389–390.

Levick WR & Williams WO (1964). Maintained activity of lateral geniculate neurones in darkness. *The Journal of Physiology* 170, 582–597.

Levine MW & Cleland BG (2001). An analysis of the effect of retinal ganglion cell impulses upon the firing probability of neurons in the dorsal lateral geniculate nucleus of the cat. *Brain research*

902, 244–254.

Li, J., Erisir, A., and Cline, H. (2011). In vivo time-lapse imaging and serial section electron microscopy reveal developmental synaptic rearrangements. *Neuron* 69, 273–286.

Liao D, Hessler NA & Malinow R (1995). Activation of postsynaptically silent synapses during pairing-induced LTP in CA1 region of hippocampal slice. *Nature* 375, 400–404.

Lin DJ-P, Kang E & Chen C (2014). Changes in input strength and number are driven by distinct mechanisms at the retinogeniculate synapse. *Journal of Neurophysiology* 112, 942–950.

Lin JY, Knutsen PM, Muller A, Kleinfeld D & Tsien RY (2013). ReaChR: a red-shifted variant of channelrhodopsin enables deep transcranial optogenetic excitation. *Nature neuroscience* 16, 1499–1508.

Ling, C., Schneider, G.E., and Jhaveri, S. (1998). Target-specific morphology of retinal axon arbors in the adult hamster. *Vis Neurosci* 15, 559–579.

Linkenhoker, B.A., von der Ohe, C.G., and Knudsen, E.I. (2005). Anatomical traces of juvenile learning in the auditory system of adult barn owls. *Nat. Neurosci.* 8, 93–98.

Liu SJ & Zukin RS (2007). Ca^{2+} -permeable AMPA receptors in synaptic plasticity and neuronal death. *Trends in Neurosciences* 30, 126–134.

Liu X & Chen C (2008). Different roles for AMPA and NMDA receptors in transmission at the immature retinogeniculate synapse. *Journal of Neurophysiology* 99, 629–643.

Livingstone M & Hubel D (1988). Segregation of form, color, movement, and depth: anatomy, physiology, and perception. *Science* 240, 740–749.

Llinas RR & Steriade M (2006). Bursting of Thalamic Neurons and States of Vigilance. *Journal of Neurophysiology* 95, 3297–3308.

Lo F, Ziburkus J & Guido W (2013). Synaptic Mechanisms Regulating the Activation of a Ca^{2+} -Mediated Plateau Potential in Developing Relay Cells of the LGN. *Journal of Neurophysiology* 110, 1175–1185.

London M & Häusser M (2005). Dendritic computation. *Annual review of neuroscience* 28, 503–532.

Louros SR, Hooks BM, Litvina L, Carvalho AL & Chen C (2014). A role for stargazin in experience-dependent plasticity. *Cell Reports* 7, 1614–1625.

Lund RD & Cunningham TJ (1972). Aspects of synaptic and laminar organization of the mammalian lateral geniculate body. *Investigative ophthalmology* 11, 291–302.

Luo L & O’Leary DDM (2005). Axon retraction and degeneration in development and disease. *Annual review of neuroscience* 28, 127–156.

Macleod N, Turner C & Edgar J (1997). Properties of developing lateral geniculate neurones in the mouse. *International Journal of Developmental Neuroscience* 15, 205–224.

Marshel JH, Kaye AP, Nauhaus I & Callaway EM (2012). Report Anterior-Posterior Direction Opponency in the Superficial Mouse Lateral Geniculate Nucleus. *Neuron* 76, 713–720.

Madisen L et al. (2012). A toolbox of Cre-dependent optogenetic transgenic mice for light-induced activation and silencing. *Nature neuroscience* 15, 793–802.

Martersteck EM, Hirokawa KE, Zeng H, Sanes JR, Harris JA, Evarts M, Bernard A, Duan X, Li Y, Ng L, Oh SW, Ouellette B, Royall JJ, Stoecklin M & Wang Q (2017). Diverse Central Projection Patterns of Retinal Ganglion Cells. *Cell Reports* 18, 2058–2072.

Martinez LM, Molano-Mazón M, Wang X, Sommer FT & Hirsch JA (2014). Statistical wiring of thalamic receptive fields optimizes spatial sampling of the retinal image. *Neuron* 81, 943–956.

Mason CA (1982). Development of Terminal Arbors of Retino- Geniculate Axons in the Kitten-I . Light Microscopical Observations. *Neuroscience* 7, 561–582.

Mastrorade DN (1987). Two classes of single-input X-cells in cat lateral geniculate nucleus. II. Retinal inputs and the generation of receptive-field properties. *Journal of Neurophysiology* 57, 381–413.

Mastrorade DN (1992). Nonlagged relay cells and interneurons in the cat lateral geniculate nucleus: receptive-field properties and retinal inputs. *Visual neuroscience* 8, 407–441.

Matthews G & Fuchs P (2010). The diverse roles of ribbon synapses in sensory neurotransmission. *Nature reviews Neuroscience* 11, 812–822.

Maunsell JHR (1992). Functional visual streams. *Current Opinion in Neurobiology* 2, 506–510.

McBride, TJ, Rodriguez-Contreras, A, Trinh, A, Bailey, R, and DeBello, WM (2008). Learning drives differential clustering of axodendritic contacts in the barn owl auditory system. *J. Neurosci.* 28, 6960–6973.

McLaughlin, T, Torborg, C, Feller, M, and O'Leary, D. (2003). Retinotopic map refinement requires spontaneous retinal waves during a brief critical period of development. *Neuron* 40, 1147–1160.

Meyer, MP, and Smith, SJ. (2006). Evidence from in vivo imaging that synaptogenesis guides the growth and branching of axonal arbors by two distinct mechanisms. *J Neurosci* 26, 3604–3614.

Michael CR (1988). Retinal afferent arborization patterns, dendritic field orientations, and the segregation of function in the lateral geniculate nucleus of the monkey. *Proceedings of the National Academy of Sciences* 85, 4914–4918.

Montero VM (1991). A quantitative study of synaptic contacts on interneurons and relay cells of the cat lateral geniculate nucleus. *Experimental Brain Research* 86, 2570270.

Montero VM & Wenthold RJ (1989). Quantitative immunogold analysis reveals high glutamate levels in retinal and cortical synaptic terminals in the lateral geniculate nucleus of the macaque. *Neuroscience* 31, 639–647.

Mooney R, Madison D V. & Shatz CJ (1993). Enhancement of transmission at the developing retinogeniculate synapse. *Neuron* 10, 815–825.

Mooney, R., Penn, A.A., Gallego, R., and Shatz, C.J. (1996). Thalamic relay of spontaneous retinal activity prior to vision. *Neuron* 17, 863–874.

Moore BD, Kiley CW, Sun C & Usrey WM (2011). Responses in the Adult Lateral Geniculate Nucleus. *Neuron* 71, 812–819.

Morgan JL, Berger DR, Wetzel AW & Lichtman JW (2016). The Fuzzy Logic of Network Connectivity in Mouse Visual Thalamus. *Cell* 165, 192–206.

Murphy GJ & du Lac S (2001). Postnatal Development of Spike Generation in Rat Medial Vestibular Nucleus Neurons. *Journal of neurophysiology* 85, 1899–1906.

Narushima M, Uchigashima M, Yagasaki Y, Harada T, Nagumo Y, Uesaka N, Hashimoto K, Aiba A, Watanabe M, Miyata M & Kano M (2016). The Metabotropic Glutamate Receptor Subtype 1 Mediates Experience-Dependent Maintenance of Mature Synaptic Connectivity in the Visual Thalamus. *Neuron* 91, 1097–1109

Nassi JJ & Callaway EM (2009). Parallel processing strategies of the primate visual system. *NatRevNeurosci* 10, 360–372.

Nirenberg S & Meister M (1997). The light response of retinal ganglion cells is truncated by a displaced amacrine circuit. *Neuron* 18, 637–650.

Noutel J, Hong YK, Leu B, Kang E & Chen C (2011). Experience-dependent retinogeniculate synapse remodeling is abnormal in MeCP2-deficient mice. *Neuron* 70, 35–42.

Owens MT, Feldheim DA, Stryker MP, Triplett JW, Owens MT, Feldheim DA, Stryker MP & Triplett JW (2015). Stochastic Interaction between Neural Activity and Molecular Cues in the Formation of Topographic Article Stochastic Interaction between Neural Activity and Molecular Cues. *Neuron* 87, 1261–1273.

Palagina G, Meyer JF & Smirnakis XSM (2017). Complex Visual Motion Representation in Mouse Area V1. **37**, 164–183.

de Paola, V, Holtmaat, A, Knott, G, Song, S, Wilbrecht, L, Caroni, P, and Svoboda, K. (2006). Cell type-specific structural plasticity of axonal branches and boutons in the adult neocortex. *Neuron* 49, 861–875.

Pirchio M, Turner JP, Williams SR, Asproдини E & Crunelli V (1997). Postnatal Development of Membrane Properties and delta Oscillations in Thalamocortical Neurons of the Cat Dorsal Lateral Geniculate Nucleus. *Journal of Neuroscience* 17, 5428–5444.

Piscopo DM, El-Danaf RN, Huberman AD & Niell C (2013). Diverse Visual Features Encoded in Mouse Lateral Geniculate Nucleus. *Journal of Neuroscience* 33, 4642–4656.

Portera-Cailliau, C., Weimer, R.M., De Paola, V., Caroni, P., and Svoboda, K. (2005). Diverse modes of axon elaboration in the developing neocortex. *PLoS Biol.* 3, e272.

Purves, D, and Lichtman, JW (1980) Elimination of synapses in the developing nervous system. *Science* (80-.). 210, 153–157.

Rafols JA & Valverde F (1973). The structure of the dorsal lateral geniculate nucleus in the mouse. A golgi and electron microscopic study. *The Journal of Comparative Neurology* 150, 303–331.

Ramoa AS & McCormick DA (1994a). Enhanced activation of NMDA receptor responses at the immature retinogeniculate synapse. *J Neurosci* 14, 2098–2105.

Ramoa AS & McCormick DA (1994b). Developmental changes in electrophysiological properties of LGNd neurons during reorganization of retinogeniculate connections. *The Journal of Neuroscience* 14, 2089–2097.

Ramoa AS & Prusky G (1997). Retinal activity regulates developmental switches in functional

properties and ifenprodil sensitivity of NMDA receptors in the lateral geniculate nucleus. *Developmental brain research* 101, 165–175.

Ramos A, Schwartz EL. & Roy E. (1976). Stable and Plastic Unit Discharge Patterns during Behavioral Generalization. *Science* 192, 393–396.

Rathbun DL, Alitto HJ, Warland DK & Usrey WM (2016). Stimulus Contrast and Retinogeniculate Signal Processing. *Frontiers in Neural Circuits* 10, 1–10.

Rathbun DL, Alitto HJH & Weyand TG (2007). Interspike interval analysis of retinal ganglion cell receptive fields. *Journal of Neurophysiology* 98, 911–919.

Rathbun DL, Warland DK & Usrey WM (2010). Spike timing and information transmission at retinogeniculate synapses. *The Journal of Neuroscience* 30, 13558–13566.

Rimmele TS & Rosenberg PA (2016). Neurochemistry International GLT-1 : The elusive presynaptic glutamate transporter. *Neurochemistry International* 98, 19–28.

Robson JA (1981). Abnormal axonal growth in the dorsal lateral geniculate nucleus of the cat. *The Journal of Comparative Neurology* 195, 453–476.

Robson JA (1993). Qualitative and quantitative analyses of the patterns of retinal input to neurons in the dorsal lateral geniculate nucleus of the cat. *The Journal of Comparative Neurology* 334, 324–336.

Robson JA & Mason CA (1979). The synaptic organization of terminals traced from individual labeled retino-geniculate axons in the cat. *Neuroscience* 4, 99–111.

Rompani SB, Mullner FE, Wanner A, Roth CN, Yonehara K, Zhang C & Roska B (2017). Different Modes of Visual Integration in the Lateral Geniculate Nucleus Revealed by Single-Cell-Initiated Transsynaptic Tracing. *Neuron* 93,767–776.

Rowan S & Cepko CL (2004). Genetic analysis of the homeodomain transcription factor Chx10 in the retina using a novel multifunctional BAC transgenic mouse reporter. *Developmental Biology* 271, 388–402.

Rowe MH & Fischer Q (2001). Dynamic properties of retino-geniculate synapses in the cat. *Visual neuroscience* 18, 219–231.

Rozov A, Zilberter Y, Wollmuth LP & Burnashev N (1998). Facilitation of currents through rat Ca²⁺-permeable AMPA receptor channels by activity-dependent relief from polyamine block. *Journal of Physiology* 511, 361–377.

- Ruthazer, E.S., Li, J., and Cline, H.T. (2006). Stabilization of axon branch dynamics by synaptic maturation. *J Neurosci* 26, 3594–3603.
- Sabbah S, Berg D, Papendorp C, Briggman KL & Berson DM (2017). A Cre Mouse Line for Probing Irradiance- and Direction-Encoding Retinal Networks. *Eneuro* 4, ENEURO.0065-17.2017.
- Sanderson KJ, Bishop P & Darian-Smith I (1971). The properties of the binocular receptive fields of lateral geniculate neurons. *Experimental Brain Research* 13, 178–207.
- Sanes JR & Masland RH (2014). The Types of Retinal Ganglion Cells: Current Status and Implications for Neuronal Classification. *Annual Review of Neuroscience* 38, 150421150146009.
- Saunders A, Johnson CA, Sabatini BL & Miyamichi K (2012). Novel recombinant adeno-associated viruses for Cre activated and inactivated transgene expression in neurons. 6, 1–10.
- Schafer DP & Stevens B (2010). Synapse elimination during development and disease: immune molecules take centre stage. *BiochemSocTrans* 38, 476–481.
- Schmitt L & Halassa M (2016). Interrogating the mouse thalamus to correct human neurodevelopmental disorders. doi, 1–9.
- Scholl B, Tan AYY, Corey J & Priebe NJ (2013). Emergence of orientation selectivity in the Mammalian visual pathway. *The Journal of Neuroscience* 33, 10616–10624.
- Seabrook T a, Eleftheriou CG, Krahe TE, Fox M a & Guido W (2013). Retinal input regulates the timing of corticogeniculate innervation. *The Journal of Neuroscience* 33, 10085–10097.
- Seeburg DP, Liu X & Chen C (2004). Frequency-dependent modulation of retinogeniculate transmission by serotonin. *The Journal of Neuroscience* 24, 10950–10962.
- Sengpiel F & Kind PC (2002). The role of activity in development of the visual system. *Current Biology* 12, 818–826.
- Shatz CJ (2009). MHC Class I: An Unexpected Role in Neuronal Plasticity. *Neuron* 64, 40–45.
- Shatz CJ & Kirkwood PA (1984). Prenatal development of functional connections in the cat's retinogeniculate pathway. *The Journal of Neuroscience* 4, 1378–1397.
- Sherman SM (2004). Interneurons and triadic circuitry of the thalamus. *Trends in Neurosciences* 27, 670–675.

- Sherman SM (2005). Thalamic relays and cortical functioning. *Progress in brain research* 149, 107–126.
- Sherman SM (2007). The thalamus is more than just a relay. *Current Opinion in Neurobiology* 17, 417–422.
- Sherman SM (2016). Thalamus plays a central role in ongoing cortical functioning. *Nature Neuroscience* 16, 533–541.
- Sherman SM & Guillery R (1996). Functional organization of thalamocortical relays. *Journal of Neurophysiology* 76, 1367–1395.
- Sherman SM & Guillery R (2002). The role of the thalamus in the flow of information to the cortex. *Philosophical transactions of the Royal Society of London Series B, Biological sciences* 357, 1695–1708.
- Sherman SM & Guillery RW (2001). *Exploring the Thalamus*. Elsevier.
- Shlens J, Rieke F & Chichilnisky EJ (2008). Synchronized firing in the retina. *Current Opinion in Neurobiology* 18, 396–402.
- Sherman SM & Koch C (1986). The control of retinogeniculate transmission in the mammalian lateral geniculate nucleus. *Exp Brain Res* 63, 1–20.
- Shou T & Leventhal AG (1989). Organized Arrangement of Orientation-Sensitive Cat ' s Dorsal Lateral Geniculate Nucleus Relay Cells in the. *Journal of Neuroscience* 9, 4287–4302.
- Sillito AM, Murphy PC, Salt TE & Moody CI (1990). Dependence of retinogeniculate transmission in cat on NMDA receptors. *J Neurophysiol* 63, 347–55.
- Silver, MA, and Stryker, MP. (1999). Synaptic density in geniculocortical afferents remains constant after monocular deprivation in the cat. *J. Neurosci.* 19, 10829–10842.
- Silver RA (2010). Neuronal arithmetic. *Nature Reviews Neuroscience* 11, 474–489.
- Sincich LC, Adams DL, Economides JR & Horton JC (2007). Transmission of spike trains at the retinogeniculate synapse. *The Journal of Neuroscience* 27, 2683–2692.
- Sincich LC, Horton JC & Sharpee T (2009). Preserving information in neural transmission. *Journal of Neuroscience* 29, 6207–6216.
- Smith EL, Chino Y, Ridder WH, Kitagawa K & Langston A (1990). Orientation bias of neurons in

the lateral geniculate nucleus of macaque monkeys. *Visual Neuroscience* 5, 525–545.

Snider, CJ, Dehay, C, Berland, M, Kennedy, H, and Chalupa, LM (1999). Prenatal development of retinogeniculate axons in the macaque monkey during segregation of binocular inputs. *J Neurosci* 19, 220–228.

Soodak RE, Shapley RM & Kaplan E (1987). Linear mechanism of orientation tuning in the retina and lateral geniculate nucleus of the cat. *Journal of Neurophysiology* 58, 267–275.

Soto D, Coombs ID, Kelly L, Farrant M & Cull-Candy SG (2007). Stargazin attenuates intracellular polyamine block of calcium-permeable AMPA receptors. *Nature neuroscience* 10, 1260–1267.

Sretavan DW & Shatz CJ (1984). Prenatal development of individual retinogeniculate axons during the period of segregation. *Nature* 308, 845–848.

Sretavan DW & Shatz CJ (1986). Prenatal development of retinal ganglion cell axons: segregation into eye-specific layers within the cat's lateral geniculate nucleus. *The Journal of Neuroscience* 6, 234–251.

Sriram B, Meier PM & Reinagel P (2016). Temporal and spatial tuning of dorsal lateral geniculate nucleus neurons in unanesthetized rats. *Journal of Neurophysiology* 115, 2658–2671.

Stanley GB, Jin J, Wang Y, Desbordes G, Wang Q, Black MJ & Alonso JM (2012). Visual orientation and directional selectivity through thalamic synchrony. *The Journal of Neuroscience* 32, 9073–9088.

Stafford BK & Huberman AD (2017). Signal Integration in Thalamus: Labeled Lines Go Cross-Eyed and Blurry. *Neuron* 93, 717–720.

Stephan AH, Barres BA & Stevens B (2012). The Complement System: An Unexpected Role in Synaptic Pruning During Development and Disease. *Annu Rev Neurosci* 35, 369–389.

Stettler, DD, Yamahachi, H, Li, ., Denk, W, and Gilbert, CD. (2006). Axons and synaptic boutons are highly dynamic in adult visual cortex. *Neuron* 49, 877–887.

Steriade M, Jones EG & McCormick DA (1997). *Thalamus*. Elsevier, Oxford.

Stoelzel CR, Huff JM, Bereshpolova Y, Zhuang J, Hei X, Alonso JM & Swadlow HA (2015). Hour-long adaptation in the awake early visual system. *Journal of Neurophysiology* 114, 1172–1182.

Stevens, B., Allen, N.J., Vazquez, L.E., Howell, G.R., Christopherson, K.S., Nouri, N., Micheva, K.D., Mehalow, A.K., Huberman, A.D., Stafford, B., et al. (2007). The classical complement cascade mediates CNS synapse elimination. *Cell* 131, 1164–1178.

Storchi R, Milosavljevic N, Eleftheriou CG, Martial FP, Orlowska-Feuer P, Bedford RA, Brown TM, Montemurro MA, Petersen RS & Lucas RJ (2015). Melanopsin-driven increases in maintained activity enhance thalamic visual response reliability across a simulated dawn. *Proceedings of the National Academy of Sciences* 112, E5734–E5743.

Straub C & Tomita S (2012). The regulation of glutamate receptor trafficking and function by TARPs and other transmembrane auxiliary subunits. *Current opinion in neurobiology* 22, 488–495.

Sugihara, I. (2005). Microzonal projection and climbing fiber remodeling in single olivocerebellar axons of newborn rats at postnatal days 4-7. *J. Comp. Neurol.* 487, 93–106.

Sur M, Esguerra M, Garraghty PE, Kritzer MF & Sherman SM (1987). Morphology of physiologically identified retinogeniculate X- and Y-axons in the cat. *Journal of Neurophysiology* 58, 1–32.

Sur, M, and Sherman, SM. (1982). Retinogeniculate terminations in cats: morphological differences between X and Y cell axons. *Science* 218, 389.

Sur M, Weller RE & Sherman SM (1984). Development of X and Y-cell retinogeniculate terminations in kittens. *Nature* 310, 246–249.

Suresh V, Ciftcio lu UM, Wang X, Lala BM, Ding KR, Smith WA, Sommer FT & Hirsch JA (2016). Synaptic Contributions to Receptive Field Structure and Response Properties in the Rodent Lateral Geniculate Nucleus of the Thalamus. *Journal of Neuroscience* 36, 10949–10963.

Takeuchi, YAsano, H, Katayama, Y, Muragaki, Y, Imoto, K, and Miyata, M. (2014). Large-Scale Somatotopic Refinement via Functional Synapse Elimination in the Sensory Thalamus of Developing Mice. *J. Neurosci.* 34, 1258–1270.

Tapia, JC, Wylie, JD, Kasthuri, N, Hayworth, KJ, Schalek, R, Berger, DR, Guatimosim, C, Seung, HS, and Lichtman, JW. (2012). Pervasive synaptic branch removal in the mammalian neuromuscular system at birth. *Neuron* 74, 816–829.

Tarusawa E, Matsui K, Budisantoso T, Molnár E, Watanabe M, Matsui M, Fukazawa Y & Shigemoto R (2009). Input-specific intrasynaptic arrangements of ionotropic glutamate receptors and their impact on postsynaptic responses. *The Journal of Neuroscience* 29, 12896–12908.

Taschenberger H et al. (2002). Optimizing Synaptic Architecture and Efficiency for High-

Frequency Transmission. *Neuron* 36, 1127–1143.

Taschenberger H & von Gersdorff H (2000). Fine-tuning an auditory synapse for speed and fidelity: developmental changes in presynaptic waveform, EPSC kinetics, and synaptic plasticity. *The Journal of Neuroscience* 20, 9162–9173.

Tavazoie SF & Reid RC (2000). Diverse receptive fields in the lateral geniculate nucleus during thalamocortical development. *Nature neuroscience* 3, 608–616.

Thomas CG, Tian H & Diamond JS (2011). The relative roles of diffusion and uptake in clearing synaptically released glutamate change during early postnatal development. *The Journal of neuroscience : the official journal of the Society for Neuroscience* 31, 4743–4754.

Thompson AD, Gribizis A, Chen C & Crair MC (2017). Activity-dependent development of visual receptive fields. *Current Opinion in Neurobiology* 42, 136–143.

Thompson AD, Picard N, Min L, Fagiolini M & Chen C (2016). Cortical Feedback Regulates Feedforward Retinogeniculate Refinement. *Neuron* 91, 1021–1033.

Thompson KG, Zhou Y & Leventhal AG (1994). Direction-sensitive X and Y cells within the A laminae of the cat's LGNd. *Visual neuroscience* 11, 927–938.

Tomita S, Stein V, Stocker TJ, Nicoll RA & Brecht DS (2005). Bidirectional synaptic plasticity regulated by phosphorylation of stargazin-like TARPs. *Neuron* 45, 269–277.

Toni N, Buchs P a, Nikonenko I, Bron CR & Muller D (1999). LTP promotes formation of multiple spine synapses between a single axon terminal and a dendrite. *Nature* 402, 421–425.

Tootle, S., and Friedlander, M.J. (1989). Postnatal Development of the Spatial Contrast Sensitivity Y-Cells in the Kitten Retinogeniculate Pathway of X- and. *The Journal of Neuro* 9, 1324–1340.

Traynelis SF, Wollmuth LP, McBain CJ, Menniti FS, Vance KM, Ogden KK, Hansen KB, Yuan H, Myers SJ & Dingledine R (2010). Glutamate Receptor Ion Channels: Structure, Regulation, and Function. *Pharmacological Reviews* 62, 405–496.

Trenholm S, Johnson K, Li X, Smith RG & Awatramani GB (2011). Parallel mechanisms encode direction in the retina. *Neuron* 71, 683–694.

Turner JP, Leresche N, Guyon A, Soltesz I & Crunelli V (1994). Sensory input and burst firing output of rat and cat thalamocortical cells: the role of NMDA and non-NMDA receptors. *The Journal of Physiology* 480, 281–295.

Turner JP & Salt TE (1998). Characterization of sensory and corticothalamic excitatory inputs to rat thalamocortical neurones in vitro. *The Journal of Physiology* 510, 829–843.

Tzingounis A V & Wadiche JI (2007). Glutamate transporters: confining runaway excitation by shaping synaptic transmission. *Nat Rev Neurosci* 8, 935–947.

Usrey WM & Alitto HJ (2015). Visual Functions of the Thalamus. *Annual Review of Vision Science* 1, 351–371.

Usrey WM, Reppas JB & Reid RC (1998). Paired-spike interactions and synaptic efficacy of retinal inputs to the thalamus. *Nature* 395, 384–387.

Usrey WM, Reppas JB & Reid RC (1999). Specificity and strength of retinogeniculate connections. *Journal of Neurophysiology* 82, 3527–3540.

Vidyasagar TR & Urbas J V. (1982). Orientation sensitivity of cat LGN neurones with and without inputs from visual cortical areas 17 and 18. *Experimental Brain Research* 46, 157–169.

Wang C, Cleland BG & Burke W (1985). Synaptic delay in the lateral geniculate nucleus of the cat. *Brain research* 343, 236–245.

Wang X, Hirsch JA & Sommer FT (2010). Recoding of sensory information across the retinothalamic synapse. *The Journal of Neuroscience* 30, 13567–13577.

Wang X, Wei Y, Vaingankar V, Wang Q, Koepsell K, Sommer FT & Hirsch JA (2007). Feedforward excitation and inhibition evoke dual modes of firing in the cat's visual thalamus during naturalistic viewing. *Neuron* 55, 465–478.

Weyand TG (2007). Retinogeniculate Transmission in Wakefulness. *Journal of Neurophysiology* 98, 769–785.

Weyand TG (2016). The multifunctional lateral geniculate nucleus. *Reviews in the Neurosciences* 27, 135–157.

Wierenga, CJ, Becker, N, and Bonhoeffer, T. (2008). GABAergic synapses are formed without the involvement of dendritic protrusions. *Nat. Neurosci.* 11, 1044–1052.

Wiesel, T.N., and Hubel, D.H. (1963). Effects of Visual Deprivation on Morphology and Physiology of Cells in the Cat's Lateral Geniculate Body. *Journal of Neurophysiology* 26, 978–993.

Wilson JR, Friedlander JM & Sherman SM (1984). Fine structural of identified X- and Y-cells

morphology in the cat's lateral geniculate nucleus. *Proceedings of the Royal Society of London Series B* 221, 411–436.

Wilson PD, Rowe MH & Stone J (1976). Properties of relay cells in cat's lateral geniculate nucleus: a comparison of W-cells with X- and Y-cells. *Journal of Neurophysiology* 39, 1193–1209.

Winfield DA, Hiorns RW & Powell TPS (1980). A quantitative electron-microscopical study of the postnatal development of the lateral geniculate nucleus in normal kittens and in kittens with eyelid suture. *Proceedings of the Royal Society* 210, 211–234.

Winnubst, J., and Lohmann, C. (2012). Synaptic clustering during development and learning: the why, when, and how. *Front. Mol. Neurosci.* 5, 70.

Wong RO (1999). Retinal waves and visual system development. *Annu Rev Neurosci* 22, 29–47.

Wong RO, Meister M & Shatz CJ (1993). Transient period of correlated bursting activity during development of the mammalian retina. *Neuron* 11, 923–938.

Yang YC, Hu CC, Huang CS & Chou PY (2014). Thalamic synaptic transmission of sensory information modulated by synergistic interaction of adenosine and serotonin. *Journal of Neurochemistry* 128, 852–863.

Yeh C-I, Stoelzel CR, Weng C & Alonso JM (2009). Functional consequences of neuronal divergence within the retinogeniculate pathway. *Journal of Neurophysiology* 101, 2166–2185.

Yeow MBL & Peterson EH (1991). Active zone organization and vesicle content scale with bouton size at a vertebrate central synapse. *Journal of Comparative Neurology* 307, 475–486.

Yuste R (2015). From the neuron doctrine to neural networks. *Nature Reviews Neuroscience* 16, 487–497.

Zaltsman JB, Heimel JA & Van Hooser SD (2015). Weak orientation and direction selectivity in lateral geniculate nucleus representing central vision in the gray squirrel *Sciurus carolinensis*. *Journal of Neurophysiology* 113, 2987–2997.

Zeater N, Cheong SKK, Solomon SGG, Dreher B & Martin PR (2015). Binocular Visual Responses in the Primate Lateral Geniculate Nucleus. *Current Biology* 25, 1–6.

Zhang W & Linden DJ (2009). Neuromodulation at Single Presynaptic Boutons of Cerebellar Parallel Fibers Is Determined by Bouton Size and Basal Action Potential-Evoked Ca Transient Amplitude. 29, 15586–15594.

Zhao X, Chen H, Liu X & Cang J (2013). Orientation-selective responses in the mouse lateral geniculate nucleus. *The Journal of Neuroscience* 33, 12751–12763.

Zheng, W., and Knudsen, E.I. (2001). Gabaergic inhibition antagonizes adaptive adjustment of the owl's auditory space map during the initial phase of plasticity. *J. Neurosci.* 21, 4356–4365.

Ziburkus J, Dilger EK, Lo F-S & Guido W (2009). LTD and LTP at the developing retinogeniculate synapse. *Journal of Neurophysiology* 102, 3082–3090.

Ziburkus J & Guido W (2006). Loss of binocular responses and reduced retinal convergence during the period of retinogeniculate axon segregation. *Journal of Neurophysiology* 96, 2775–2784.

Ziburkus J, Lo F-S & Guido W (2003). Nature of inhibitory postsynaptic activity in developing relay cells of the lateral geniculate nucleus. *Journal of neurophysiology* 90, 1063–1070.

Zylberberg J, Cafaro J, Turner MH, Shea-brown E & Rieke F (2016). Direction-Selective Circuits Shape Noise to Ensure a Precise Population Code. *Neuron* 89, 369–383.